YB:TUNGSTATE WAVEGUIDE LASERS

Fiona Mair Bain

A Thesis Submitted for the Degree of PhD
at the
University of St. Andrews

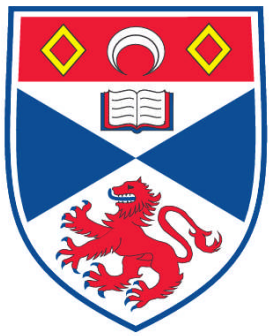

2010

Yb:tungstate Waveguide Lasers

Thesis presented for the degree of

Doctor of Philosophy

to the University of St Andrews

by

Fiona Mair Bain

May 2010

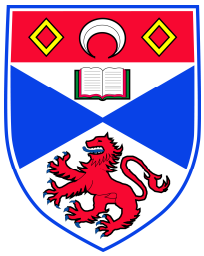

The J. F. Allen Physics Research Laboratories
School of Physics and Astronomy
University of St Andrews
North Haugh
St Andrews
Scotland
KY16 9SS

Declarations

I, Fiona Mair Bain, hereby certify that this thesis, which is approximately thirty-five thousand words in length, has been written by me, that it is the record of work carried out by me and that it has not been submitted in any previous application for a higher degree.

I was admitted as a research student in October 2006 and as a candidate for the degree of Doctor of Philosophy in October 2006; the higher study for which this is a record was carried out in the University of St Andrews between 2006 and 2010.

Date: **Signature of candidate:**

I hereby certify that the candidate has fulfilled the conditions of the Resolution and Regulations appropriate for the degree of Doctor of Philosophy in the University of St Andrews and that the candidate is qualified to submit this thesis in application for that degree.

Date: **Signature of supervisor:**

Copyright Declaration

In submitting this thesis to the University of St Andrews I understand that I am giving permission for it to be made available for use in accordance with the regulations of the University Library for the time being in force, subject to any copyright vested in the work not being affected thereby. I also understand that the title and the abstract will be published, and that a copy of the work may be made and supplied to any bona fide library or research worker, that my thesis will be electronically accessible for personal or research use unless exempt by award of an embargo as requested below, and that the library has the right to migrate my thesis into new electronic forms as required to ensure continued access to the thesis. I have obtained any third-party copyright permissions that may be required in order to allow such access and migration, or have requested the appropriate embargo below.

The following is an agreed request by candidate and supervisor regarding the electronic publication of this thesis:

Access to Printed copy and electronic publication of thesis through the University of St Andrews.

Date: **Signature of candidate:**

Signature of supervisor:

Abstract

Lasers find a wide range of applications in many areas including photo-biology, photo-chemistry, materials processing, imaging and telecommunications. However, the practical use of such sources is often limited by the bulky nature of existing systems. By fabricating channel waveguides in solid-state laser-gain materials more compact laser systems can be designed and fabricated, providing user-friendly sources. Other advantages inherent in the use of waveguide gain media include the maintenance of high intensities over extended interaction lengths, reducing laser thresholds.

This thesis presents the development of Yb:tungstate lasers operating around 1μm in waveguide geometries. An Yb:$KY(WO_4)_2$ planar waveguide laser grown by liquid phase epitaxy is demonstrated with output powers up to 190 mW and 76 % slope efficiency. This is similar to the performance from bulk lasers but in a very compact design. Excellent thresholds of only 40 mW absorbed pump power are realised. The propagation loss is found to be less than 0.1 $dBcm^{-1}$ and *Q*-switched operation is also demonstrated.

Channel waveguides are fabricated in Yb:$KGd(WO_4)_2$ and Yb:$KY(WO_4)_2$ using ultrafast laser inscription. Several of these waveguides lase in compact monolithic cavities. A maximum output power of 18.6 mW is observed, with a propagation loss of ~2 $dBcm^{-1}$. By using a variety of writing conditions the optimum writing pulse energy is identified. Micro-spectroscopy experiments are performed to enable a fuller understanding of the induced crystal modification. Observations include frequency shifts of Raman lines which are attributed to densification of WO_2W bonds in the crystal.

Yb:tungstate lasers can generate ultrashort pulses and some preliminary work is done to investigate the use of quantum dot devices as saturable absorbers. These are shown to have reduced saturation fluence compared to quantum well devices, making them particularly suitable for future integration with Yb:tungstate waveguides for the creation of ultrafast, compact and high repetition rate lasers.

Acknowledgements

During this PhD I have been privileged to receive great support from many colleagues, family and friends, and so there are various people I'd like to thank.

Special thanks must go Tom Brown who's been an excellent supervisor, supporting me at every stage; giving me opportunities to present my work; encouraging me through the writing process; and being the only person (so far) to have read through my entire thesis! His feedback in this has been extremely helpful. Particular thanks must also go to Alexander Lagatsky. His help and advice in the lab have been invaluable, and the work presented here would not have been accomplished without him.

I would also like to thank all other group members past and present: Ben, Chris, Christine, Craig, Douglas, Eddie, Flavio, Gajendra, Klaus, Mario, Ronan and Wilson, for their advice on various pieces of equipment, listening to and giving feedback on my talks, and for useful discussions on various topics. Thanks go to all my collaborators in Minsk, Heriot Watt and Madrid, and especially Robert, Dani and Wagner with whom I've had personal contact. Thanks are due to all the guys from the workshop for various mounts that they've made for me, thanks to Scott for dealing with all the deliveries, thanks to the secretaries for all their administration work, and thanks to Mike and Cameron for keeping me safe in the building!

Thanks to my many friends in the department, besides those mentioned previously, who have been a support throughout my studies here: Jill, Janelle, Lani, Maria, Claire, Areti, Anna Chiara and Sarah. Also thanks to Svetlana, from the Physics department in Dundee, who has been an excellent conference roommate, has helped me prepare and practice for most of my talks, and has provided useful quantum dot discussions. Thanks also to my MSc friends, particularly Kamol, Klearchos, Shailen and Wei, who have been an incredibly useful resource by reminding me of basic photonics! Thanks to my hall and housemates over the years who have been fantastic to live with: Jill (again), Keeley, Laurie, Bani and all others from Gannochy House.

Especial thanks to Jörg for being not only an excellent colleague and friend in the department, but the best fiancé who has read almost as much of my thesis as Tom has! Du bist *der* Beste!

Finally I'd like to thank my family, who have supported me from the beginning in everything I've ever done. Duncan, Jenny and Alistair are a great set of siblings, and Alistair deserves special mention for working through a derivation of the waveguide equation. Mum and Dad have always been a great influence and encouragement, and without them none of this would have been possible. I'd like to thank them both for listening to me practice various conference talks again and again. Thanks also to Mum for reading and commenting on my abstract, conclusion and other sections of my thesis, and to Dad for reading and correcting my first year report, and I know he would have gladly read through the whole thesis for me if he could have.

In loving memory of Dad

Dr Robert Bruce Vorlich Bain

Time Passes

Just sitting here in contemplation
Aging slowly, measured and unseen,
While mind and time both race ahead
Far from those places I have been

Our fleeting life goes by so fast
Like an arrow's murderous flight
Straight and true, unerringly
Toward the target in its sight

Or like a comet in the night
Streaking through the starry sky,
Furiously, at breakneck speed
Before its fading light must die

Neither turning nor yet slowing
It seeks always to find its mark
Ever on, by fire consumed,
Towards a future stark and dark

And like that comet, so are we
However much we speed our span
However fast to those near by
It's as a flash, since time began

We cannot slow it, cannot turn it
All we can is seize the day
Cherish, hold, squeeze every moment
Before it too must fly away

For however fast we run
Or however high we climb
We can never long outpace
Those slowly flowing sands of time

R. B. V. Bain, June 2008

Contents

Glossary of Symbols

$\|\|$	Parallel
α	Gain/loss co-efficient
α_{dB}	Gain/loss co efficient in dB
β	Angle between $\boldsymbol{a}$ and $\boldsymbol{c}$ crystallographic axes
δ	Round trip cavity loss
δ_{coupl}	Coupling loss
δ_{dB}	Loss in dB
δ_{ins}	Insertion loss
δ_{launch}	Launch efficiency
δ_{ns}	Non-saturable losses
δ_{prop}	Propagation loss
η	Slope efficiency
η_0	Intrinsic slope efficiency
η_p	Pump quantum efficiency
θ	Angle, where subscripts *i*, *r* and *t* represent incidence, reflection and transmission
θ_c	Critical angle
λ	Wavelength, subscripts of *p* and *l* represent pump and lasing wavelengths respectively
π	Pi, 3.1416
σ	Cross section, where subscripts *a* and *e* represent absorption and emission
σ_x^2	Second moment of a beam along *x*
$\Delta\tau$	Pulse duration
τ_{rec}	Recovery time
τ_{rt}	Round trip cavity time
τ_{upp}	Upper state life-time
υ_p	Phase velocity of light
φ	Goos-Hänchen phase shift
φ_{am}	Angle between $\boldsymbol{a}$ and $\mathbf{N_m}$
φ_{cg}	Angle between $\boldsymbol{c}$ and $\mathbf{N_g}$

$\chi^{(i)}$	*i*th order susceptibility
$\Delta\omega$	Full spectral range of cavity
$\boldsymbol{a}$, $\boldsymbol{b}$, $\boldsymbol{c}$	Crystallographic axes
a	Waveguide asymmetry parameter
$\boldsymbol{a_{ij}}$	Thermal expansion co-efficient
A	Single pass absorption
b	Normalised guide index
c	Speed of light, 2.998×10^{-8} ms^{-1}
d_{guide}	Waveguide thickness
e	Euler's number, 2.718
E	Energy, where subscript *p* denotes pulse energy
$\boldsymbol{E}$	Electric field
ΔE	Energy difference
f	Fractional population of level
$f_{1(0)}$	Fractional population of upper lasing level
f_{rep}	Repetition rate
F	Represents L = 3
F	Fluence, where subscripts *sat*, *p*, *pGauss* and *0* represent saturation, pulse, Gaussian pulse and peak saturation respectively
g	Degeneracy
h	Planck's constant, 6.626×10^{-34} Js
I	Intensity
J	Total angular momentum
k	Wavenumber, equal to $2\pi/\lambda$
k_B	Boltzmann's constant
L	Orbital angular momentum
L	Length
m	Mode number
m_e	Effective mass of electron
M^2	Measure of beam quality
n_x, n_y, n_z	Principal quantum numbers along *x*, *y* and *z*
n	Refractive index

n_{eff}	Effective refractive index of a waveguide
n_2	Nonlinear refractive index
$\mathbf{N_m}$, $\mathbf{N_g}$, $\mathbf{N_p}$	Principal optical axes
N	Population of given state
$N_{0(3)}$	Population of lower lasing level
p	Constant which depends on pulse shape
P_{abs}	Absorbed pump power
$P_{abs,th}$	Threshold absorbed pump power
P_i	Incident power
P_{out}	Output power
P_{t_bulk}	Power transmitted through bulk material
P_{t_guide}	Power transmitted through waveguide
Q	Quality of a cavity
r	Radius of waveguide core
r_l	Normalised laser mode
r_p	Normalised pump mode
R	Reflectivity, subscripts *s* and *pi* denote sigma and pi polarisations
ΔR	Modulation depth
R_F	Fresnel reflection
R_{lin}	Reflectivity under low light intensity
R_{ns}	Saturated reflectivity
R_p	Pumping rate
$R_{p,th}$	Threshold pumping rate
s, p, d, f	Angular momentum quantum numbers 0, 1, 2 and 3
S	Spin angular momentum
S	Saturation parameter
T	Temperature
T_F	Transmission of end facets
T_{obj}	Transmission of objective
T_{OC}	Transmission of output coupler
t	Time
v	Molecular vibration, subscripts are described in text
Vol	Volume

V	Normalised frequency Parameter
w	Beam waist (radius at e^{-2}), where subscripts l and p denote lasing and pump modes and 0 denotes beam waist at focus
x, y, z	Spatial co-ordinates
$\mathbf{X_1'}$, $\mathbf{X_2'}$, $\mathbf{X_3'}$	Thermal expansion co-efficients in the principal system
z_R	Rayleigh range

Glossary of Acronyms

2D	Two dimensional
3D	Three dimensional
at.	Atomic
A	Monovalent alkali-metal cation
ABCD	Matrix elements for optical ray matrix
Al	Aluminium
AL	Achromatic lens
AFM	Atomic Force Microscopy
ASE	Amplified spontaneous emission
CCD	Charge coupled device
CW	Continuous wave
DBR	Distributed Bragg reflector
DM	Dichroic mirror
GaAs	Gallium Arsenide
Gd	Gadolinium
HT	High transmission
HR	High reflector
HWP	Half-waveplate
IR	Infrared
K	Potassium
KLM	Kerr-lens mode locking
LiF	Lithium fluoride
Ln	Lanthanide
LPE	Liquid phase epitaxy/epitaxially
Lu	Lutetium
M	Mirror
MBE	Molecular beam epitaxy
N.A.	Numerical aperture
Nd	Neodymium
O	Oxygen
Obj	Objective

OC	Output coupler
OSA	Optical spectrum analyser
PbS	Lead sulfide
PBS	Polarising beam-splitter
PLD	Pulsed laser deposition
R	Trivalent metal or rare-earth cation
RF	Radio frequency
SBR	Saturable Bragg reflector
SESAM	Semiconductor saturable absorber mirror
SF10	Fused silica prism
SIMS	Secondary ion mass spectroscopy
Sm	Samarium
TE	Transverse electric field
TEM	Transmission electron microscopy
TEM_{00}	Fundamental mode Gaussian beam
Ti	Titanium
TM	Transverse magnetic field
TSSG	Top-seeded solution growth
QD	Quantum dot
QW	Quantum well
QWP	Quarter waveplate
ULI	Ultrafast laser inscription/inscribed
W	Tungsten
$(WO_4)_2$	Double tungstate
Y	Yttrium
YAG	Yttrium aluminium garnet
Yb	Ytterbium
YVO_4	Yttrium vanadate

Publications

Journal Publications

1. "Ultrafast laser inscribed Yb:$KGd(WO_4)_2$ and Yb:$KY(WO_4)_2$ channel waveguide lasers," F. M. Bain, A. A. Lagatsky, R. R. Thomson, N. D. Psaila, N. V. Kuleshov, A. K. Kar, W. Sibbett, C. T. A. Brown, Opt. Exp. **17,** 22417-22422 (2009)

2. "Continuous-wave and Q-switched operation of a compact, diode-pumped Yb^{3+}:$KY(WO_4)_2$ planar waveguide laser", F. M. Bain, A. A. Lagatsky, S. V. Kurilchick, V. E. Kisel, S. A. Guretsky, A. M. Luginets, N. A. Kalanda, I. M. Kolesova, N. V. Kuleshov, W. Sibbett and C. T. A. Brown, Opt. Exp. **17**, 1666-1670 (2009)

3. "Low-loss quantum-dot-based saturable absorber for efficient femtosecond pulse generation" A. A. Lagatsky, F. M. Bain, C. T. A. Brown, W. Sibbett, D. A. Livshits, G. Erbert and E. U. Rafailov, Appl. Phys. Lett. **91**, 231111-231113, (2007)

4. "Micro-spectroscopy of ultrafast laser inscribed channel waveguides in Yb:tungstate crystals," F. M. Bain, W. F. Silva, A. A. Lagatsky, R. R. Thomson, N. D. Psaila, A. K. Kar, W. Sibbett, D. Jaque, C. T. A. Brown, submitted for publication in Appl. Phys. Lett., June 2010

5. "Lasing action at around 1.9 μm from an ultrafast laser inscribed Tm-doped glass waveguide," F. Fusari, R. R. Thomson, G. Jose, F. M. Bain, A. A Lagatsky, N. D. Psaila, A. K. Kar, A. Jha, W. Sibbett, C. T. A. Brown, to be submitted for publication, 2010

Conference Proceedings

1. “Optical Waveguides in Glasses doped with Lead Sulfide Quantum Dots”, A. M. Malyarevich, K. V. Yumashev, A. A. Lagatsky, F. M. Bain, C. T. A. Brown, W. Sibbett, R. R. Thomson, A. K. Kar, A. A. Anushchenko, A. A. Zhilin, A. A. Lipovskii, Physics, Chemistry and Application of Nanostructures, 140-143 (2009)

2. “Diode-pumped femtosecond Yb:KYW laser incorporating a quantum-dot saturable absorber”, A. A. Lagatsky, F. Bain, C. T. A. Brown, W. Sibbett, D. A. Livshits, G. Erbert, E. U. Rafailov, 2007 Conference of Laser and Electro-Optics/Quantum Electronics and Laser Science Conference (CLEO/QELS 2007), **1-5**, 472-473 (2007)

3. “High-power Kerr-lens mode-locked ytterbium lasers” F. M. Bain, A. A. Lagatsky, C. T. A. Brown and W. Sibbett, Solid State Lasers XV11: Technology and Devices, Proc. of SPIE, **6871**, L68712, 2008

Presented Talks

1. “Micro-Luminescence and Micro-Raman Mapping of Ultrafast Laser Inscribed Yb:$KGd(WO_4)_2$ and Yb:$KY(WO_4)_2$ Channel Waveguides,” F. M. Bain, A. A. Lagatsky, W. F. Silva, D. Jaque, R. R. Thomson, N. D. Psaila, A. K. Kar, W. Sibbett, C. T. A. Brown, presented by F. M. Bain, presentation number CMQ7 at CLEO, San Jose, California, May 2010

2. “Diode-pumped ytterbium-doped double tungstate waveguide lasers,” F. M. Bain, A. A. Lagatsky, W. Sibbett, C. T. A. Brown, presented by F. M. Bain at SU2P symposium, Glasgow, March 2010

3. “Diode-pumped double-tungstate waveguide lasers”, F. M. Bain, A. A. Lagatsky, W. Sibbett and C. T. A. Brown, invited talk presented by F. M.

Bain at the University of Twente, Enschede, The Netherlands, October 2009

4. “Diode-pumped double-tungstate waveguide lasers”, F. M. Bain, A. A. Lagatsky, C. T. A. Brown and W. Sibbett, invited talk presented by C. T. A. Brown at the 18th International Laser Physics Workshop (LPHYS ’09) at ICFO, Barcelona, Spain, July 2009

5. “Yb:KGd(WO_4)$_2$ channel waveguide laser fabricated by ultrafast laser writing”, F. M. Bain, A. A. Lagatsky, W. Sibbett, C. T. A. Brown, R. R. Thomson, N. D. Psaila, A. K. Kar and N. V. Kuleshov, presented by F. M. Bain, presentation number CJ7.3 at CLEO Europe, Munich, Germany, June 2009

6. “Diode-pumped Yb:KYW waveguide lasers” F. M. Bain, A. A. Lagatsky, S. V. Kurilchik, V. E. Kisel, S. A. Guretsky, A. M. Luginets, I. M. Kolesova, C. T. A. Brown, W. Sibbett and N. V. Kuleshov, presented by F. M. Bain at 3rd EPS-QEOD Europhoton Conference, Paris, France, September 2008

7. “1 micron and 1.3 micron femtosecond lasers mode-locked using quantum-dot-based saturable absorbers”, F. M. Bain, A. A. Lagatsky, C. T. A. Brown, W. Sibbett, D. A. Livshits, A. E. Zhukov, V. M. Ustinoc, E. U. Rafailov, presented by F. M. Bain at CLEO Europe, Munich, Germany, June 2007

So what you like, let you decide
And don't let fashions fetter
It matters not if it is new
It matters if it's better

And disregard the taunts and barbs
Of 'It's been done before'
For so have life and sex and love
Yet still we do them more

From *Convention,* R. B. V. Bain, March 2008

Chapter 1
Introduction and Background

1.1 Half a Century of the Laser

Fifty years have passed since the first demonstration of the laser by Maiman in 1960 [1], and during this time the world has been transformed by the advances that this light source, which was once described as a "solution waiting for a problem" [2], has brought. As a coherent light source it has wide-ranging relevance to various applications; for example in the fields of holography [3] and interferometry [4], where lasers have been used in CD players [5, 6], lithography [7], optical sensing [8] and LIDAR [9]. A further property of interference is that, given a large enough bandwidth, ultrashort pulses can be generated and pulses as short as 6.5 fs (6.5×10^{-15} s) have now been produced directly from a laser [10]. The creation of broadband, ultrashort pulses has revolutionised many disciplines, from photo-biology, photo-chemistry [11-15] and medicine [16-18] to materials processing [19, 20] and telecommunications [21]. However, few of these applications have made use of the ruby laser, which was the laser initially built by Maiman. All of these various exciting techniques have relied on the steady but intensive efforts of researchers over the past five decades to vary the properties of available lasers; both in terms of fundamental physical aspects, such as available wavelength [22-28], efficiency [29, 30], output power [31-33], threshold [34, 35], pulse duration [10, 36-39], pulse energy [40] and repetition rate [41]; and also with regard to design, as more compact laser sources are inherently lighter, more practical and user-friendly [42, 43].

The aim of the research described in this thesis has been the development of compact and efficient lasers at wavelengths around 1 μm. Ytterbium-doped crystalline materials have been chosen as gain media due to their excellent material and spectroscopic properties, which have previously been shown to lase in a bulk geometry with excellent efficiencies and to be capable of producing ultrashort pulses [44]. Their high absorption and emission cross sections also make them suitable for the creation of compact sources, as only short crystal lengths are necessary. A further

goal of this work was the fabrication and lasing of waveguides based on these materials which enable ultracompact monolithic cavities with relatively low thresholds to be constructed.

The topics investigated in this thesis are all now introduced, beginning with a discussion of the ytterbium ion and its suitability as a dopant for producing ultrashort pulses with a wavelength around 1 μm. Of equal importance to the chosen dopant is the host crystal, and details of the hosts explored during these experiments are also presented. This topic leads on to a description of the quasi-three-level laser, which is followed by a brief review of continuous wave (CW), *Q*-switched and mode-locked regimes. Finally the theory of optical waveguides and their applications to laser design are discussed briefly together with some fabrication techniques, and a synopsis of the remaining thesis is presented.

1.2 The Ytterbium Ion

Ytterbium is a rare-earth lanthanide element, generally found as the trivalent cation Yb^{3+}. It was discovered in 1878 [45] and first used as an ion for a laser transition in 1965 [25]. However, its potential as a laser ion was largely ignored until a suitable diode pump became available in 1990 [46]. Ytterbium's electron configuration is described by [Xe] $6s^2$ $4f^{14}$, with two valence electrons in the 6s orbital and one in the 4f orbital, while its cation has an ionic radius of 87 pm and the electron configuration [Xe] $4f^{13}$. This means it lacks one electron to complete its valence shell. The 4f sub-shell is shielded by the complete 5s and 5p sub-shells.

The 13 electrons in the outer sub-shell, 4f, of Yb^{3+} consist of six pairs of electrons in six of the orbitals, plus one final unpaired electron in the seventh orbital. Thus the total spin angular momentum, S, is a half. Multiplicity is given by 2S+1 [47] and consequently the multiplicity of Yb^{3+} is 2, giving rise to a doublet term. The total orbital angular momentum, L, is 3. The total angular momentum, J, combines the electrons' orbital and spin angular momenta by considering their relative orientations. The values of J are given by the series J = L + S, L + S - 1, …|L - S| [48], and thus for Yb^{3+} there are only two possible values of J: 7/2 or 5/2. Accordingly, the two energy

levels of the ytterbium ion are given by the terms $^2F_{7/2}$ and $^2F_{5/2}$, where terms are written in the standard form $^{2S+1}L_J$, and L = 3 is represented by the symbol F. According to Hund's third selection rule, if the outer shell is over half-full then the lowest energy level has the highest total angular momentum [49]. Therefore $^2F_{7/2}$ is the ground state of Yb^{3+} whilst $^2F_{5/2}$ is the excited state, and these are separated by approximately 10000 cm^{-1} [50] (the precise value will depend upon the ion's host). A material containing Yb ions will thus absorb and emit around 1 micron.

The ytterbium ion is therefore described by a simple two-level system, and the absence of other energy levels is advantageous for lasing as losses due to excited state absorption, upconversion and concentration quenching are removed even at higher doping levels [51, 52]. Other advantages of ytterbium when used as the active laser ion include: strong absorption and emission cross sections particularly in the double tungstate hosts; strong absorption around 980 nm making it highly suitable for diode pumping with readily available InGaAs laser diodes; a small Stokes shift which leads to high slope efficiencies; and inhomogeneous broadening in many hosts which provides a broad emission bandwidth suitable for femtosecond pulse generation.

These points outline the attractiveness of Yb^{3+} as an active laser ion, and particularly the suitability of this ion for creating compact and efficient lasers. There are numerous examples of lasing from various Yb-doped materials in the literature, with many reporting excellent efficiencies and ultrashort pulses [53-67]. Additional benefits can include using ytterbium as a sensitizer for many other rare-earth ions [57, 68, 69].

1.3 Double Tungstates as Laser Hosts

Equally important to the choice of ion when developing a good laser material is the choice of a suitable host. In this thesis crystalline hosts have been chosen. Although more expensive to fabricate than glasses, the advantages of crystals in terms of strength, homogeneity, thermal conductivity and large cross sections – leading to lower thresholds – can more than outweigh the greater cost. Furthermore, with the correct choice of host, it is possible to obtain broad and smooth emission bandwidths that are almost glass-like in appearance.

Double tungstates were chosen as hosts in this experimental work. These are a group of crystals with the formula $A^{I}R^{III}(WO_4)_2$, where A is a monovalent alkali-metal cation, and R is a trivalent metal or rare-earth cation. They are biaxial crystals, with strong $\chi^{(2)}$ and $\chi^{(3)}$ nonlinearies, making them suitable for second harmonic generation and stimulated Raman scattering applications [70]. They also provide broad emission bandwidths making them suitable hosts for the generation of ultrashort pulses. $KGd(WO_4)_2$ (KGdW), $KY(WO_4)_2$ (KYW) and $KLu(WO_4)_2$ (KLuW) are the double tungstates which have attracted most attention as crystalline laser host materials [56, 57, 65, 67, 71] .

Two of these double tungstates are used as host materials in this thesis – KGdW and KYW – and these have all been grown by our collaborators in Minsk, Belarus[1] using a modified Czochralski method [72]. This technique (also known as the top-seeded solution growth (TSSG)) consists of melting the constituents of the crystal into a crucible at a high temperature, above the saturation temperature. The melt can be left for several hours or days to ensure homogeneity and good optical quality of the crystal. The melt is then gradually cooled to the saturation temperature. A seed crystal is then introduced and crystal growth begins, with an orientation matching that of the seed. As growth continues the crystal is slowly rotated and pulled from the melt. Meanwhile the melt is gradually cooled to ensure the solution remains supersaturated. For growth of Yb:KGdW and Yb:KYW the $K_2W_2O_7$ solvent is generally chosen [73] or K_2WO_4 [70] can alternatively be used.

1.3.1 Double Tungstate Crystal Structure

Both KGdW and KYW are monoclinic crystals which can be described either by the C2/c space group, or the I2/c space group. In crystallography C2/c notation is generally preferred, however the parameters associated with I2/c space group are those used throughout this thesis. This is due to these parameters comparing well with the morphology of the crystals. Most of the data presented, such as absorption and emission spectra and pump and lasing polarisations correspond to the crystallographic

[1] S. V. Kurilchick, V. E. Kisel, N. V. Kuleshov, Research Institute for Optical Materials and Technologies, Belarus National Technical University, 65 Nezavistimosti Ave., 220013 Minsk, Belarus

axes as defined for the I2/c space group. However, it is possible to convert between the two using the transformations:

$$\boldsymbol{a^* = a + c}$$
$$\boldsymbol{b^* = -b}$$
$$\boldsymbol{c^* = -c}$$

where * represents the C2/c notation. A diagram illustrating this is shown in fig. 1.1. The unit cell parameters are quoted many times in the literature, and typical values are shown in table 1.1 where good agreement can be seen between the various sources.

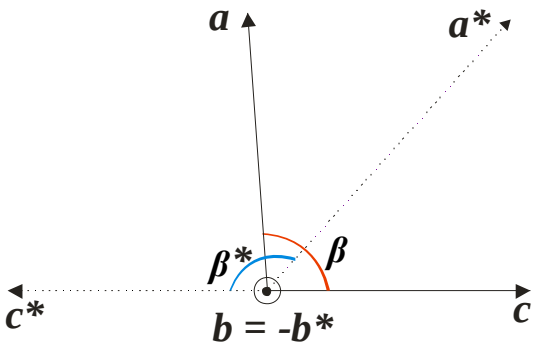

Fig. 1.1. Relative orientations of crystallographic ***a***, ***b*** and ***c*** axes in different space group notations.

	Unit cell parameters				**Reference**
KGdW	***a* (nm)**	***b* (nm)**	***c* (nm)**	***β* (°)**	
	0.8095	1.043	0.7588	94	[57]
	0.8098	1.0417	0.7583	94.43	[74] as quoted in [75]
	0.8084	1.0374	0.7582	94.41	[75]
	0.8122	1.0426	0.7587	94.06	[76]
	***a** (nm)**	***b** (nm)**	***c** (nm)**	***β** (°)**	
	1.0652	1.0374	0.7582	130.80	[75]
KYW	***a* (nm)**	***b* (nm)**	***c* (nm)**	***β* (°)**	
	0.805	1.035	0.754	94	[57, 77]
	***a** (nm)**	***b** (nm)**	***c** (nm)**	***β** (°)**	
	1.064	1.035	0.754	130.5	[77, 78]

Table 1.1. Unit cell parameters for KGdW and KYW single crystals, as quoted in literature.

The potassium, gadolinium and yttrium atoms occupy 4*e* Wyckoff positions, whilst tungsten and oxygen occupy 8*f* Wyckoff positions. More data regarding the atomic co-ordinates of the specific atoms can be found in [75]. The crystallographic structure of KGdW is shown in fig. 1.2. KYW's structure is identical except that yttrium replaces the gadolinium. When doping with a lanthanide, the trivalent metal is replaced with the active doping ion, and so for ytterbium doping the ytterbium ion replaces the gadolinium or yttrium. The ionic radii of these cations are [79]:

Gd^{3+}: 93.8 pm

Y^{3+}: 90.0 pm

Yb^{3+}: 86.8 pm

As the ionic radii of these lanthanides are all similar, good quality crystals can be grown [75].

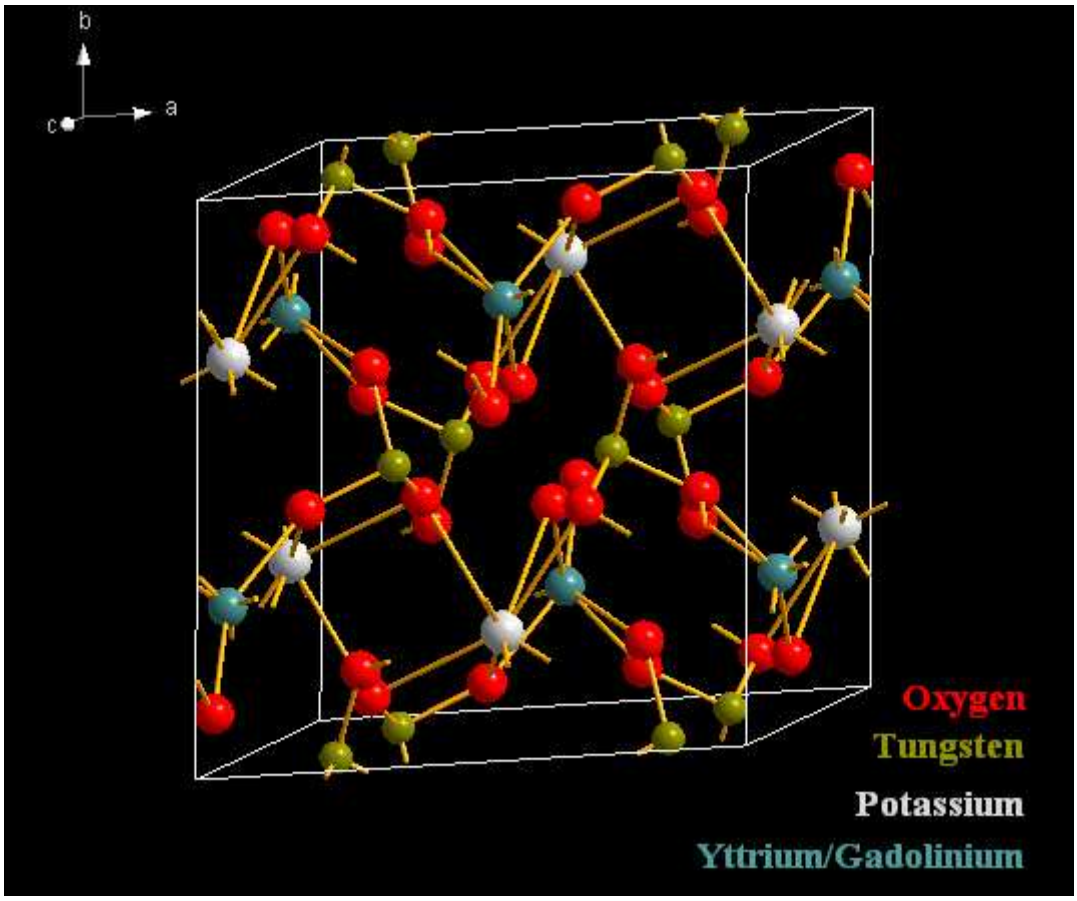

Fig. 1.2. Image illustrating the crystal structure of KYW/KGdW. When doping with ytterbium, the Yb ion replaces the yttrium or gadolinium. Image was drawn using in *Diamond* using data from [75].

1.3.2 Thermal Properties

The thermal expansion co-efficients in the principal system, $\mathbf{X_1'}$, $\mathbf{X_2'}$, $\mathbf{X_3'}$, for KGdW [75] and KYW [80], together with the orientation of these vectors are shown below:

KGdW

$$(a_{ij}) = \begin{pmatrix} 10.64 & 0 & 0 \\ 0 & 2.83 & 0 \\ 0 & 0 & 23.44 \end{pmatrix} \times 10^{-6}\ \mathrm{K}^{-1}$$

KYW

$$(a_{ij}) = \begin{pmatrix} 11.0 & 0 & 0 \\ 0 & 1.9 & 0 \\ 0 & 0 & 17.8 \end{pmatrix} \times 10^{-6}\ \mathrm{K}^{-1}$$

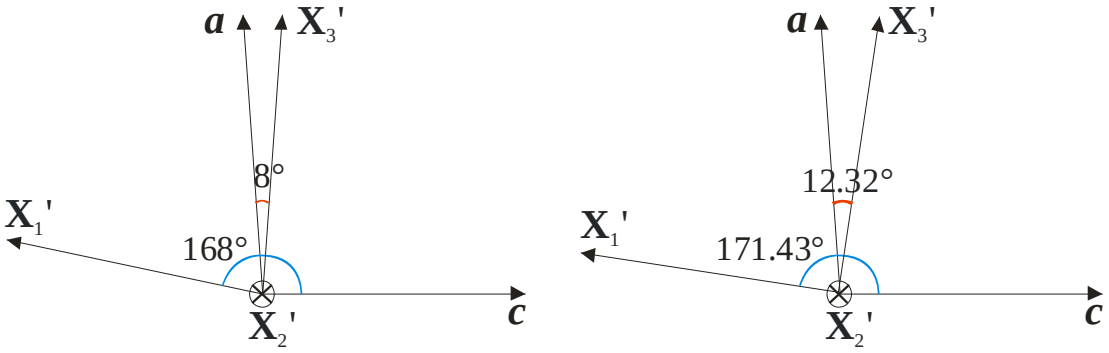

Fig. 1.3. Axes of thermal expansion co-efficients relative to crystallographic axes for (a) KGdW and (b) KYW.

Clearly the largest expansion is close to the crystallographic ***a*** axis, whilst the ***b*** axis experiences considerably less thermal expansion. The thermal conductivity of these crystals is relatively low, at only around 3 $Wm^{-1}K^{-1}$ [81]. However, the low quantum defect in these crystals when doped with Yb^{3+} helps to circumvent this problem.

1.3.3 Optical Properties

The double tungstates are characterised by relatively high refractive indices of around 2. They are also highly anisotropic due to their large crystal anisotropy with three principal optical axes, $\mathbf{N_m}$, $\mathbf{N_g}$ and $\mathbf{N_p}$, which have refractive indices of n_m, n_g and n_p respectively. A range of values for these important parameters exist in the literature and a summary of these results are given in table 1.2 where the orientation of angles φ_{cg} and φ_{am} are shown in fig. 1.4. As KYW, KGdW and KYbW are

isostructural the refractive index increase of KYW and KGdW is linear with Yb^{3+} doping concentration [82].

	KGdW [83]	**KGdW** [84]		**KGdW** [85]			**KYW** [77]	**KYbW** [86]
λ (nm)	1060	532	1546	532	1060	1546	1064	632.8
n_g	2.033	2.1091	2.0385	2.1187	2.0610	2.0514	2.0507	2.12
n_m	1.986	2.0686	2.0028	2.0627	2.0103	1.9819	2.0065	2.06
n_p	1.937	2.0352	1.9741	2.0307	1.9819	1.9718	1.9688	2.03
φ_{cg}	20°	19.3°		21.5°			17.5°	19°
φ_{am}	24°	15.3°		17.1°			13.5°	16°

Table 1.2. Principal optical axes refractive indices and axes orientation of double tungstates.

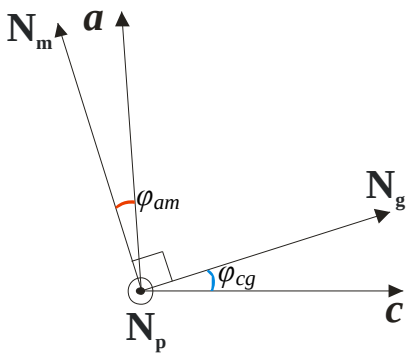

Fig. 1.4. Orientation of principal optical axes of double tungstates.

The nonlinear refractive index, n_2, is very important in a laser crystal. It can sometimes be detrimental to lasing performance, by causing optical breakdown and limiting the available output power, but it can also be advantageous as it is necessary for ultrashort pulse generation using Kerr-lens mode locking (KLM). Values for n_2 are notoriously difficult to determine and contain large errors in their stated value. Nonetheless it is agreed that the double tungstates are characterised by relatively large values of n_2 where Yb:KGdW has been quoted to have an n_2 of between ~$20x10^{-16}$ cm^2W^{-1} to $25x10^{-16}$ cm^2W^{-1} along $\mathbf{N_m}$, and ~$15x10^{-16}$ cm^2W^{-1} along $\mathbf{N_p}$ [87, 88]. In Yb(5 %):KYW values of $19x10^{-16}$ cm^2W^{-1} along $\mathbf{N_m}$ and $15x10^{-16}$ cm^2W^{-1} along $\mathbf{N_p}$ have been reported [88]. These values are all significantly higher than n_2 of Ti:sapphire at $3.1x10^{-16}$ m^2W^{-1} [89].

1.3.4 Absorption and Emission Properties

Some of the most important characteristics of a laser material are its absorption and emission properties. As mentioned in section 1.2, the ytterbium ion has a simple electronic structure with only two sublevels, but the values of the Stark levels within these sublevels are determined by the crystal field of the host and are illustrated in fig. 1.5.

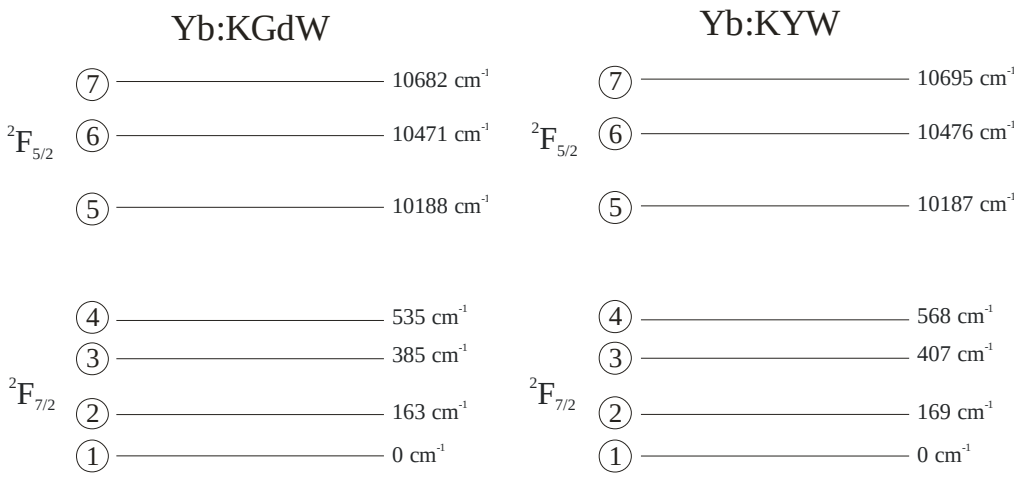

Fig. 1.5. Stark energy levels for Yb:KGdW and Yb:KYW [90]. These values correspond to a temperature of 77 K.

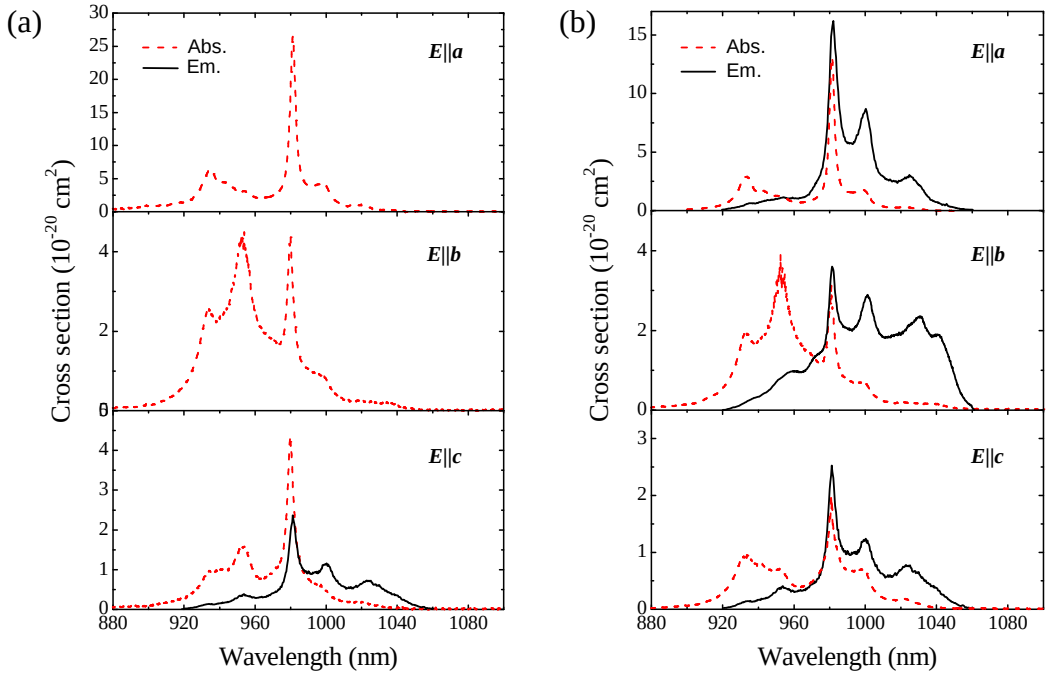

Fig. 1.6. Absorption and emission cross sections for (a) Yb:KGdW and (b) Yb:KYW. Measurements performed by our collaborators in Minsk.

In fig. 1.6 the absorption and emission cross sections as a function of wavelength are illustrated. These measurements were made by our collaborators in Minsk. As can be expected from the crystal structure, the absorption and emission spectra are highly anisotropic, where ***E*||*a*** has the strongest absorption and emission cross sections, although all axes are characterised by high cross sections when compared to many other laser materials. The absorption peak for ***E*||*a*** is found at 981.2 nm, which overlaps well with the emission from commercially available InGaAs laser diodes [46]. This is an inherent advantage of ytterbium lasers, enabling compact and efficient laser pumping. The high emission cross sections and broad emission bandwidths are suitable for supporting ultrashort pulses. The quantum efficiency of such a laser is very high at ~0.96, which substantially reduces the heat deposited in the crystal. This helps circumvent the problems associated with the poorer thermal properties of KGdW and KYW when compared to some other hosts. Some key properties of these materials are shown in table 1.3.

Property	**Yb:KGdW**	**Yb:KYW**
Absorption peak wavelength	981.2 nm	981.2 nm
Absorption linewidth	3.7 nm	3.5 nm
Peak absorption cross section	1.2×10^{-19} cm^2	1.33×10^{-19} cm^2
Emission peak wavelength	1023 nm	1025 nm
Emission linewidth	20 nm	16 nm
Peak emission cross section	2.9×10^{-20} cm^2	3×10^{-20} cm^2
Fluorescence lifetime	275 μs [84]	230 μs [52]

Table 1.3. Key properties of Yb:KGdW and Yb:KYW.

1.3.5 Summary of Previous Lasing Performance

The outstanding optical properties of Yb:KGdW and Yb:KYW have now been outlined, and excellent lasing results have been achieved from these materials over the

past 13 years. Lasing was first demonstrated in 1997 [57], using Ti:sapphire pumping where a 72 % slope efficiency was achieved in Yb:KGdW and 78 % in Yb:KYW. Diode pumping was also reported, but with poorer efficiency due to the emission wavelength of the diode, which was 965 nm. Higher slope efficiencies have now been achieved, with an 86.9 % slope efficiency reported under gain-switched Ti:sapphire pumping [90]. Slope efficiencies achieved with diode pumping have dramatically improved and slope efficiencies exceeding 80 % have been reported [71]. Excellent *Q*-switched and Raman results have been achieved [64], and ultrashort pulses have also been demonstrated. Pulses as short as 100 fs have been observed in Yb:KGdW, where a SESAM was used as the mode-locking element [91], and even shorter pulses of 66 fs have been demonstrated in an Yb:KYW laser [92]. High output powers from mode-locked Yb:KGdW lasers have been generated, with 5 W demonstrated for 134 fs pulses, and 10 W for 433 fs pulses [93]. Steps have also been taken towards creating waveguide lasers based on these materials [94], and low thresholds and excellent slope efficiencies from planar waveguides have now been reported [95-97].

1.4 The Quasi-Three-Level Laser

Lasers are typically described by a four-level system, however ytterbium lasers fall into the category of a quasi-three-level laser. This is partly because they use only three energy levels but additionally, and most significantly, because the lower lasing level is thermally populated at room temperature. This means that greater pumping is required for population inversion to be achieved in a quasi-three-level laser than for a typical four-level laser, to overcome the lower lasing level's population. The laser will also suffer from reabsorption losses, as the emitted lasing wavelength can be absorbed as it propagates through the crystal. The theory of the quasi-three-level lasers are described in greater detail by Fan and Byer [98]. The important end-result is that the absorbed pump power required to reach lasing threshold, $P_{abs,th}$, for a TEM_{00} beam is described by the equation:

$$P_{abs,th} = \frac{3\pi hc}{8 f_{1(0)} \tau_{upp} \lambda_p \eta_p} \left(\frac{\delta}{2\sigma_a(\lambda_l)} + N_{0(3)} L \right) \left(w_l^2 + w_p^2 \right) \qquad \text{Eq. 1.1}$$

where h is Planck's constant, c is the speed of light, $f_{1(0)}$ is the fractional population of the upper lasing level, τ_{upp} is the upper state laser lifetime, δ is the cavity roundtrip loss, $\sigma_a(\lambda_l)$ is the absorption cross section at the lasing wavelength, $N_{0(3)}$ is the population of the lower lasing level, L is the crystal length, w_l is the average laser mode's radius in the cavity and w_p is the average pump mode's cavity waist. The additional factor of ¾ arises from the degeneracy of the upper and lower laser levels, which are 3 and 4 respectively.

Thus it is clear that a low lasing threshold requires relatively high upper state lifetime and $f_{1(0)}$, but low losses, small population in the lower laser level, and small pump and cavity mode radii. For beam profiles which are not TEM_{00} the pump and laser mode volume will be modified, yet small waists will still produce the lowest thresholds. This equation applies to both bulk and waveguide geometries, but of course in a waveguide the pump and laser mode radii maintain a small size over the entire crystal length, and so the values of w_l and w_p are typically smaller in a waveguide laser than a bulk laser. The advantages of using a waveguide geometry in quasi-three-level lasers is therefore apparent. Even although the round-trip losses, δ, typically increase in a waveguide, with good waveguide fabrication the propagation losses can be negligible compared to the reabsorption losses which arise from the upper lasing level population, $N_{0(3)}$. Thus the $N_{0(3)}L$ term dominates over $\delta/2\sigma_a(\lambda_l)$ and so the increased loss in δ results in negligible detrimental performance compared to the bulk, but there is the added advantage of a small waist throughout the laser volume resulting in lower thresholds for the waveguide design.

1.5 Continuous and Pulsed Lasing

Lasers can be designed to run continuously or in pulse trains, where the pulses can have durations ranging from milliseconds down to femtoseconds. Pulses in the millisecond to nanosecond regime are often created by *Q*-switching [99] whilst the ultrashort pulses of pico- or femtosecond duration are generated using mode locking [100]. Both of these techniques rely on the losses in the cavity being modulated in some manner, but the mechanism responsible for the pulse formation is different in the two cases. These two situations are now briefly described.

1.5.1 *Q*-switching

In *Q*-switching, the quality, or *Q*, of the cavity is switched from high to low values. For a relatively large portion of the time the *Q*-value is low, thus losses are high and lasing threshold cannot be reached. As a result of increased losses the feedback into the cavity is reduced and so population inversion can build up to a value beyond that which would normally be reached under CW operation. The energy stored in the gain medium is limited by the spontaneous emission of the material. For a short duration, the quality of the cavity is then increased. This allows lasing to occur, as the gain in the cavity now far exceeds the losses, and so consequently all the energy is released from the cavity in a short space of time. This is illustrated in fig. 1.7. Thus *Q*-switching is a technique employed for creating very energetic and short pulses of radiation.

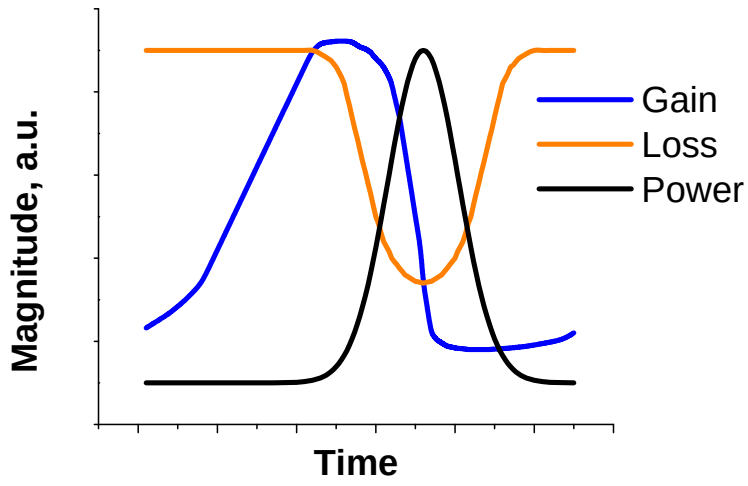

Fig. 1.7. Illustration of loss and gain modulation in a *Q*-switched cavity leading to short, energetic pulses.

Various active and passive methods are available for modulating the losses in a cavity. Typical techniques include acousto-optic modulation for active *Q*-switching or saturable absorbers for passive *Q*-switching [101]. A more in-depth overview of *Q*-switching and the parameters necessary for its optimisation can be found in [37].

1.5.2 Mode Locking

Mode locking is the name given to the technique used to generate ultrashort pulses, where an ultrashort pulse is defined as pulses with durations shorter than a nanosecond. In a CW cavity there are normally many longitudinal modes, or frequencies, present which oscillate within the cavity with no fixed phase relationship, as illustrated in fig. 1.8 (a). This results in an irradiance which varies insignificantly over time, giving a continuous and constant output. However, if by some means the modes are all positioned such that there is a fixed phase relationship between them, then at one point the waves will constructively interfere leading to high irradiance whilst elsewhere there is a minimal background signal. This results in very short bursts of light, as illustrated in fig. 1.8 (b). The duration of the pulse created using this technique depends upon the number of modes which have been locked together, and thus a broader bandwidth can lead to shorter pulses, in accordance with the bandwidth theorem:

$$\Delta\omega\Delta\tau \geq p \qquad \text{Eq. 1.2}$$

where $\Delta\omega$ is the full spectral range of the laser cavity; $\Delta\tau$ is the pulse duration and p is a constant which depends on the pulse shape. In a passively mode-locked cavity this is normally 0.315 corresponding to a sech^2 pulse shape.

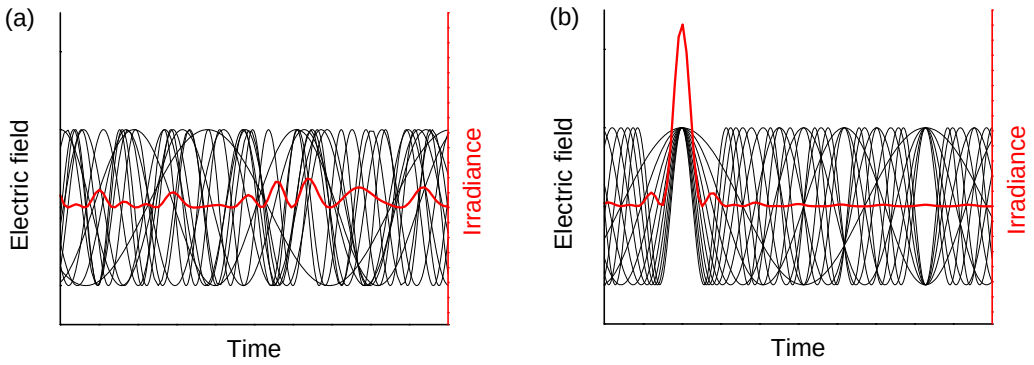

Fig. 1.8. (a) the different frequencies oscillate with no fixed relationship, leading to a CW irradiance output. (b) the different frequencies are locked together, leading to short pulses of mode-locked light.

The two sides of Eq. 1.2 are only equal for a transform limited pulse. In other cases the pulse is said to be chirped. This means that different spectral components arrive at slightly different times as a result of dispersion within the cavity. The dispersion of the cavity is therefore usually modified using prisms [102] in the cavity such that the overall dispersion of the cavity is zero, leading to the shortest and most intense pulses. A more detailed overview of mode locking is available from many sources [103, 104].

Two techniques are generally employed for passive mode locking: Kerr-lens mode locking (KLM) [38] or saturable absorber mode locking, where semiconductor saturable absorber mirrors (SESAMs) are frequently used [105]. Advantages of SESAM mode locking over KLM include that it is generally self-starting and that restraints on cavity design are somewhat relaxed. This is especially important for the construction of waveguide lasers and consequently SESAMs are the devices used in this thesis.

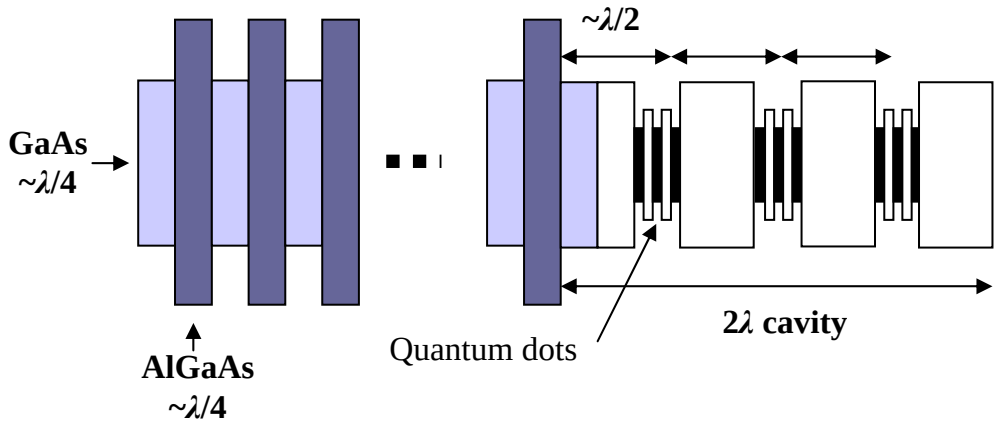

Fig. 1.9. Typical structure of a QD-SESAM, with saturable absorbers which are often made of quantum wells or quantum dots embedded within a Bragg mirror.

The principle of mode locking is that the low intensity CW radiation within a cavity experiences high losses, whilst the short duration but high intensity spikes experience low losses and thus lase preferentially. A SESAM consists of an absorbing region, which is able to be saturated at high intensities, embedded within a Bragg mirror. The reflectivity of the device is therefore dependent on the incident fluence and so provides high levels of loss to low intensity light, but under spikes of high intensity light then high reflectivity is provided by the Bragg mirror. These spikes then build up

into a train of mode-locked pulses which are emitted from the cavity. Thus mode locking can be achieved by simply and compactly replacing an end mirror with a SESAM in an otherwise CW cavity. A typical SESAM structure is illustrated in fig. 1.9.

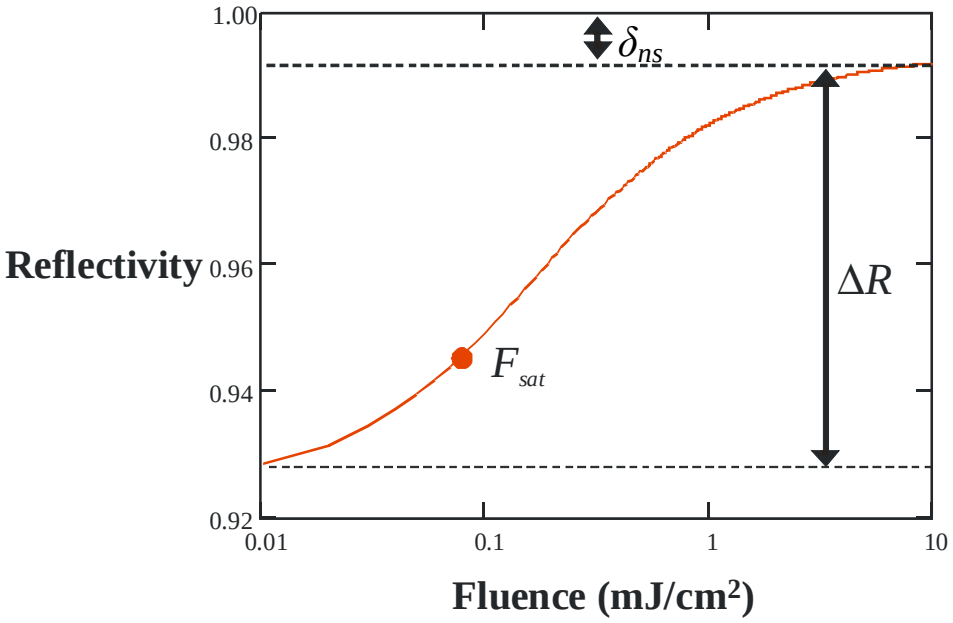

Fig. 1.10. Typical fluence-dependent reflectivity curve illustrating saturation fluence, modulation depth and non-saturable losses of the device.

SESAMs can be designed to provide various amounts of absorption and to be saturated at different levels of incident fluence. SESAMs are therefore generally described by some key parameters which are now defined. The modulation depth, ΔR, is the amount of saturable absorption present, or the change in reflectivity of the device experienced as a result of saturation. The linear reflectivity, R_{lin}, describes the reflectivity provided at low light levels under no saturation of the absorber layers. Ideally R_{lin} and ΔR would add up to 1 as the SESAM would provide 100 % reflectivity under saturation. However, due to scattering and some non-saturable absorption in the device, there are always some unwanted losses and these are known as the non-saturable losses, δ_{ns}. The saturation fluence, F_{sat}, is defined by the fluence required to change the reflectivity by $1/e$ of its modulation depth. Other characteristics of the device are the recovery time, τ_{rec}, which is the time taken for the absorption to recover after having been saturated, and the reflectivity bandwidth provided by the Bragg mirror. Some of these parameters are illustrated in fig. 1.10, where a typical SESAM's

fluence dependant reflectivity curve is shown. Although the SESAM is here described within the context of mode locking, a SESAM is also often employed as the saturable absorber in *Q*-switching where greater modulation depths are typically used.

1.6 Waveguide Theory

A waveguide is a dielectric structure which confines light, allowing light to travel long distances without diverging, as might otherwise be expected due to diffraction. Guiding is achieved by using a structure consisting of a high refractive index core region surrounded by a region or regions of lower refractive index/indices which is known as the cladding. Light propagates along the core region. The refractive index profile can gradually change throughout the media, or can be a step-like function. In the following explanation a step-like function is considered for simplicity. For a refractive index profile which varies in only one dimension, *x*, a planar waveguide is formed, which confines the light in *x* while allowing the light to diffract along *y* as the beam propagates along *z*. A channel waveguide is formed when the refractive index varies in two dimensions, *x* and *y*, confining the light in these two dimensions with propagation occurring along the third dimension, *z*. These two possibilities are illustrated in fig. 1.11.

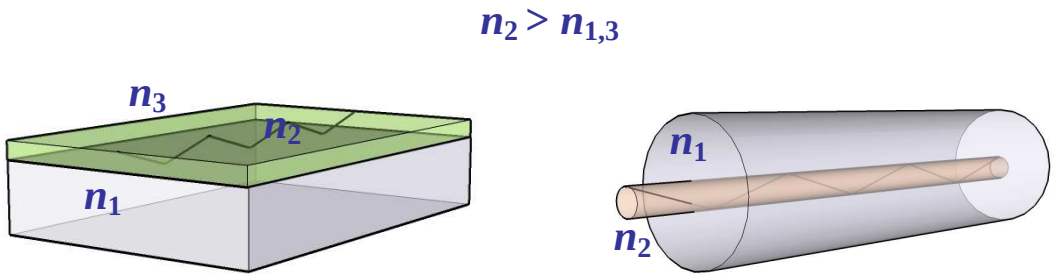

Fig. 1.11. Planar and channel waveguides, where light is confined in 1 or 2 dimensions.

In the following explanation the planar waveguide, being the simplest case, is considered using ray optics. The channel waveguide is an extension of this to include a further dimension. In-depth considerations of waveguide theory can be found in a variety of textbooks [106, 107] where explanations using both ray optics and Maxwell's equations can be found.

It is necessary to start by recalling that the refractive index, n, of a material is the ratio of the phase velocity, c, of light in a vacuum to the phase velocity of the light in the material, v_p:

$$n = \frac{c}{v_p} \qquad \text{Eq. 1.3}$$

Also recall that for a ray incident on a boundary at angle θ_i, part of this ray is reflected at θ_r (where $\theta_r = \theta_i$) and part of this ray is refracted at angle θ_t, where this angle can be determined from Snell's law:

$$n_i \sin\theta_i = n_t \sin\theta_t \qquad \text{Eq. 1.4}$$

where i and t denote the incidence and transmission sides of a boundary respectively as illustrated in fig. 1.12.

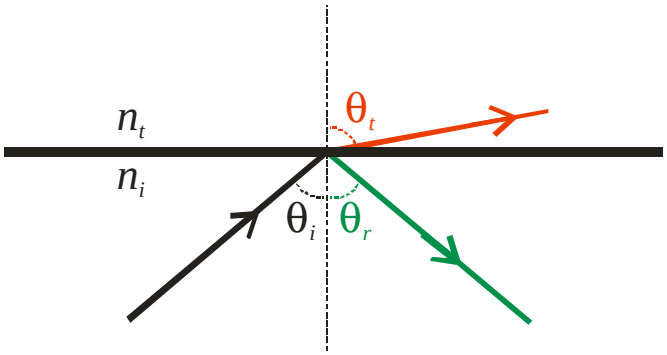

Fig. 1.12. Ray diagram illustrating the reflection and transmission which occur when light is incident on a boundary between two media of different refractive indices, where $n_i > n_t$.

From Snell's law, Eq. 1.4, it is apparent that at certain values of θ_i, defined as those greater than the critical angle, θ_c, no solution for θ_t can be found, provided $n_i > n_t$. Instead, all the light is reflected in a condition known as total internal reflection. In the case of a second boundary, as illustrated in fig. 1.13, reflection occurs at both boundaries. This is the basic principle of optical guiding, and explains, using ray optics, how light is able to propagate over large distances through a core of relatively high refractive index. A more involved derivation can be found by considering electromagnetic theory following from Maxwell's equations, giving essentially the

same result but with an additional feature: this is that the field of the propagating beam extends slightly beyond the boundary in what is known as the evanescent field. This evanescent field decays exponentially as it permeates the boundary. As a result of this, the reflected wave experiences a small phase shift upon reflection, known as the Goos-Hänchen shift [108].

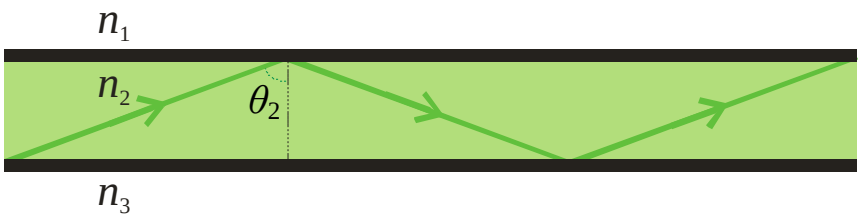

Fig. 1.13. If θ_2 is greater than the critical angle, and n_2 is greater than $n_{1,3}$, then total internal reflection occurs at both boundaries allowing optical guiding.

From this simple treatment it may seem that guiding can occur for a continuum of angles, θ, so long as $\theta > \theta_c$ and $n_i > n_t$. However, there is a third condition which must be met and this is known as the standing wave condition.

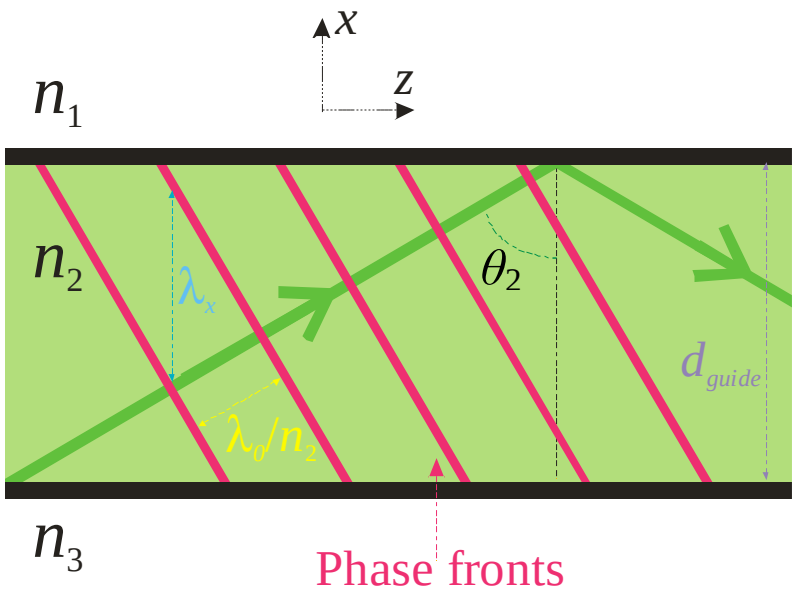

Fig. 1.14. Illustration of wavelength of the x component of the electric field, which is used to derive the waveguide standing wave condition.

The ray illustrated in fig. 1.14 has an electric field which has a component in the x and z directions. If we consider the component along the x direction we see that this electric field component travels both along $+x$ and $-x$, due to the reflection at the

boundary. This electric field component has a wavelength, λ_x, which from basic trigonometry is given by:

$$\lambda_x = \frac{\lambda_0}{n_i \cos\theta_i} \qquad \text{Eq. 1.5}$$

In order for the propagating ray to be contained in the x direction it therefore follows that the wavelength, λ_x, of the $+x$ and $-x$ electric field components must interfere to form a standing wave. If this were not the case a travelling wave would be formed which would propagate in the x direction, and thus the power would be lost from within the core region. Thus, upon a round trip of the field about the x-direction, $2d_{guide}$, there must be an integral number, m, of 2π phase shifts. The round-trip phase shift caused by the number of wavelengths of the x-component of the electric field minus the Goos-Hänchen phase shift, φ_1 and φ_2, for each reflection must therefore equal an integral number of 2π:

$$\frac{2d_{guide}}{\lambda_x} 2\pi - \varphi_1 - \varphi_2 = 2m\pi \qquad \text{Eq. 1.6}$$

Combining this with Eq. 1.5 we find

$$\frac{4\pi d_{guide} n_2 \cos\theta_2}{\lambda_0} - \varphi_1 - \varphi_2 = 2m\pi \qquad \text{Eq. 1.7}$$

or

$$k_0 d_{guide} n_2 \cos\theta_2 - \frac{\varphi_1}{2} - \frac{\varphi_2}{2} = m\pi \qquad \text{Eq. 1.8}$$

This is the standing wave condition where m is the mode number. Three conditions which must be met in order to attain guiding have now been presented, and it is found that, provided $n_2 > n_{1,3}$ and $\theta_c > \theta_2$, certain discrete propagation angles, or modes, can be guided. It is thus possible to estimate the number of modes which can be guided by re-arranging Eq. 1.8 for m, where the phase shift introduced by reflection is given by

Eq. 1.9 for a transverse electric (TE) mode or Eq. 1.10 for a transverse magnetic (TM) mode.

$$\tan\frac{\varphi_{1_{TE}}}{2}=\frac{\sqrt{n_2^{\,2}\sin^2\theta_2-n_1^{\,2}}}{n_2\cos\theta_2} \qquad \text{Eq. 1.9}$$

$$\tan\frac{\varphi_{1_{TM}}}{2}=\frac{n_2\sqrt{n_2^{\,2}\sin^2\theta_2-n_1^{\,2}}}{n_1^{\,2}\cos\theta_2} \qquad \text{Eq. 1.10}$$

When characterising optical waveguides some normalised parameters are often used, and so these will now be defined.

The normalised frequency parameter, V, is given by:

$$V=k_0 d_{guide}\sqrt{n_2^{\,2}-n_1^{\,2}} \qquad \text{Eq. 1.11}$$

An effective index of the guide, n_{eff}, is defined as the ratio of the z component of k, k_z, to k, thus:

$$n_{eff}=\frac{k_z}{k_0}=n_2\sin\theta_2 \qquad \text{Eq. 1.12}$$

We can then define a normalised guide index, b:

$$b=\frac{\left(n_{eff}^{\,2}-n_1^{\,2}\right)}{\left(n_2^{\,2}-n_1^{\,2}\right)} \qquad \text{Eq. 1.13}$$

Finally an asymmetry parameter, a, for the general case where $n_1 \neq n_3$ is introduced:

$$a_{TE}=\sqrt{\frac{n_3^{\,2}-n_1^{\,2}}{n_2^{\,2}-n_3^{\,2}}} \qquad \text{Eq. 1.14}$$

$$a_{TM} = \left(\frac{n_2^{\,2}}{n_1^{\,2}} \right) a_{TE} \qquad \text{Eq. 1.15}$$

where TE and TM represent Transverse Electric and Transverse Magnetic modes respectively.

These can be substituted into Eq. 1.8 to provide a generalised standing wave condition [109]:

$$V\sqrt{1-b} = m\pi + \tan^{-1}\left(\sqrt{\frac{b}{1-b}} \right) + \tan^{-1}\left(\sqrt{\frac{b+a}{1-b}} \right) \qquad \text{Eq. 1.16}$$

A numerical simulation of Eq. 1.16 gives rise to b versus V plots, which allows n_{eff} to be calculated for a given normalised frequency, V, and mode, m. When n_{eff} tends to n_3 then b tends to zero, and in practical terms this means the mode is very weakly confined to the core and thus experiences large exponential decay into the cladding. For $b < 0$ no real solution is found, and guiding does not occur. By setting $b = 0$ in Eq. 1.16 we can determine the normalised cut-off frequency, V_m, which can support the m-th order mode. From this we can find the minimum thickness, d_{guide}, able to support a given wavelength, λ, or the maximum wavelength, λ, which can be supported for a given core thickness. As b tends to 1, n_{eff} tends to n_2, and so tight confinement is achieved with a very small evanescent field.

An interesting point to note is that for the special case when $n_1 = n_3$ then the fundamental mode ($m = 0$) is not cut-off, and all wavelengths can be guided along such a symmetric waveguide, no matter how thin the core.

The above derivation is for the simple case of a planar waveguide. Channel waveguides are similar, although slightly more complex, and so the mode cut-off conditions for channel waveguides will only briefly be presented here. As before, in Eq. 1.11:

$$V = 2rk_0\sqrt{n_2^{\,2} - n_1^{\,2}} \qquad \text{Eq. 1.17}$$

where r is the core radius, and thus $2r$ is the core diameter. It can be shown that, for a step-index fibre, the cut-off for single mode operation is $V = 2.405$ [110, 111]. i.e. if $V < 2.405$ the waveguide will be single mode, and for $V > 2.405$ the guide is multimode. The number of guided modes can be estimated from:

$$m \sim \frac{V^2}{2} \qquad \text{Eq. 1.18}$$

For a graded index waveguide the guided mode calculations become again more complex, but nevertheless models of guided modes for any arbitrary refractive index are available in the literature. However, for the purposes of this thesis, estimates based on Eq. 1.17 and Eq. 1.18 are used.

1.7 Waveguide Fabrication

Whilst the fabrication of waveguides in glasses is not always a straightforward process, it is significantly simpler than the fabrication of crystalline waveguides. Despite the challenges, several methods for the creation of crystalline waveguides have now been developed [112]. These include: liquid phase epitaxy (LPE), thermal bonding, pulsed laser deposition (PLD), ion indiffusion, reactive ion etching and ion beam etching, ion beam implantation and wet chemical etching, proton exchange, and ultrafast laser inscription (ULI).

Amongst these techniques, LPE and thermal bonding are particularly attractive methods for the production of low-loss planar waveguides. The particular advantage of thermal bonding is that dissimilar materials can be fused together, creating a waveguide with a high numerical aperture. Additionally the spectrum from the active layer is unaffected, and cladding material with high thermal conductivity can be chosen. Using this technique waveguides with low losses of less than 1 $dBcm^{-1}$ have been demonstrated [113]. The main restriction of this technique is that it requires atomically flat surfaces in order for efficient bonding by van der Waal forces.

LPE is a method of growing an oriented single crystalline layer onto a seed crystal [114]. A molten super-saturated solution of the necessary elements is contained within a platinum crucible at the growth temperature, as shown in fig. 1.15. This growth temperature is carefully chosen such that it is high enough to prevent spontaneous crystal growth, yet it is also below the saturation temperature and so the introduction of a seed crystal to this solution will induce growth of an oriented crystal on the seed's facets. The seed crystal is dipped into this solution and is rotated as it is gradually pulled from the melt (~1 μm/min). Once the crystal is removed from the melt it is rapidly spun to remove excess flux, and it is then very gradually cooled or pulled from the furnace so as to avoid any thermal stress. A disadvantage of the technique is that it requires small lattice mismatch, but this is easily satisfied by the materials used in the experimental work presented herein. As LPE is a near-thermodynamic process, good quality crystalline layers which can act as planar waveguides can be grown with losses as low as 0.05 $dBcm^{-1}$ [115]. This technique is used in Chapter 4 to grow Yb:KYW planar waveguides.

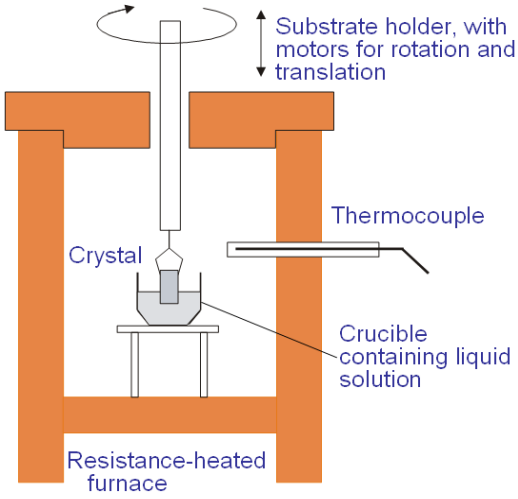

Fig. 1.15. Typical setup used for growth of waveguides by liquid phase epitaxy.

Methods for channel waveguide fabrication in crystals are still underdeveloped and typically result in high losses. One competitive method for the creation of buried channel waveguides is ion implantation [116, 117], where a lower refractive index barrier is constructed by the ion beam at a depth determined by the beam's energy. A disadvantage of this technique is that colour-centres are formed, however it is possible

to remove these by annealing. Propagation losses as low as 0.7 $dBcm^{-1}$ have been demonstrated [118], but values of 1 $dBcm^{-1}$ – 2 $dBcm^{-1}$ are more typical.

ULI is a fairly novel technique for writing waveguides which was first demonstrated in 1997 [119]. In this technique an ultrashort pulse is focused into a dielectric material. This creates high intensities in the focal volume where multiphoton and avalanche ionisation occur leading to a modification of the sample. By translating the sample through the focal volume, as illustrated in fig. 1.16, a modified channel is created. The sample can be translated longitudinally or transversally. Even though longitudinal writing, by its very nature, creates a symmetric waveguide, transversal writing is often the preferred technique as there is no limit on the length of waveguide which can be fabricated. In glasses waveguides are typically formed within the written volume, whilst in crystals, as with ion implantation, a lower index barrier is often created at the focal volume. The foremost contributory factor to the waveguide formation is the stress-induced refractive index increase in a surrounding region [120]. Waveguides fabricated using this technique are described in section 3.6 and Chapters 5 and 6.

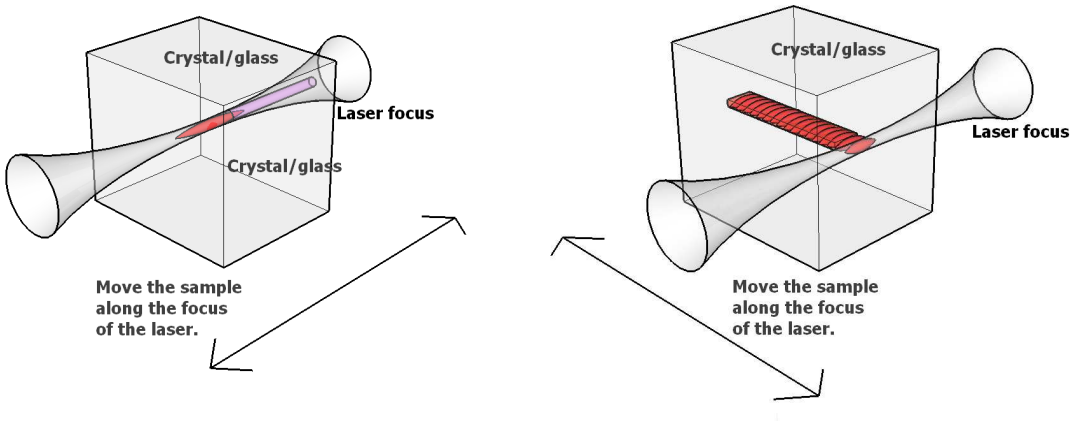

Fig. 1.16. Schematics of longitudinal and transversal ULI geometries.

The physical mechanisms responsible for the refractive index changes are not currently fully understood: however, it is widely agreed that the quality of the fabricated waveguide depends strongly on material type and writing parameters. The writing parameters which have been identified as significant are: pulse energy, pulse duration, repetition rate, scan speed, wavelength, focusing geometry, polarisation, and writing direction (as a result of wavefront tilt). When writing waveguides in our

samples we therefore tried to vary these parameters as much as possible over our limited sample size to enable optimisation of writing conditions for good quality waveguides. The particular set-up used in our experiments is described in section 2.2. Losses as low as 0.6 $dBcm^{-1}$ have previously been demonstrated in crystalline channel waveguides fabricated by ULI [121], but typical losses are currently greater than 2 $dBcm^{-1}$. As the physics of the writing process is further understood, however, it is envisioned that optimised waveguides with significantly lower losses are feasible.

1.8 Conclusion and Thesis Synopsis

In this chapter the background to the experiments presented in the remainder of this thesis have been described, from the crystalline materials chosen for this work – Yb:KGdW and Yb:KYW – and their quasi-three-level nature, to waveguide theory and fabrication techniques. In the following chapters a description of the experimental work carried out is presented. Firstly the general experimental techniques which were used for many of the experiments are described in Chapter 2. Chapter 3 presents the characterisation of a novel quantum dot (QD)-SESAM and the formation of channel waveguides in a QD-doped glass. Progress towards creating compact and integrated laser devices is then made as Chapter 4 presents a planar waveguide Yb:KYW laser, where the waveguide was fabricated by liquid phase epitaxy. Chapter 5 presents experimental realisation of channel waveguide lasers in Yb:KGdW and Yb:KYW, fabricated by the novel technique of ultrashort pulse laser inscription. In Chapter 6 micro-Raman and micro-luminescence measurements of these channel waveguides are discussed, providing some insight into the structural changes to the crystals responsible for the channel waveguide formation. Chapter 7 then summarises and concludes the work presented in this thesis, with a look towards the future goals and possible challenges faced in further development of this work.

1.9 References

[1] T. H. Maiman, "Stimulated Optical Radiation in Ruby," Nature **187,** 493 (1960).

[2] C. H. Townes, "A Century of Nature: Twenty-One Discoveries that Changed Science and the World", University of Chicago Press, L. Garwin and T. Lincoln, 2003, p.107-112

[3] E. Leith and J. Upatnieks, "Reconstructed Wavefronts and Communication Theory," Journal of the Optical Society of America **52,** 1123-1130 (1962).

[4] D. G. Peterson and A. Yariv, "Interferometry and Laser Control with Solid Fabry-Perot Etalons," Applied Optics **5,** 985-991 (1966).

[5] J. Russell. In 3501586: United States, 1970.

[6] J. Russell. In 3806643; Batelle Development Corporation: United States, 1974.

[7] C. P. Fucetola, H. Korre and K. K. Berggren, "Low-cost interference lithography," Journal of Vacuum Science & Technology B **27,** 2958-2961 (2009).

[8] F. Allario, S. Katzberg and J. Hoell, "Interferometric Measurements of Atmospheric Species", Sringer-Verlag, D. Killinger and A. Mooradian, 1983, Optical and laser remote sensing, p.71-77

[9] V. E. Derr and C. G. Little, "A Comparison of Remote Sensing of Clear Atmosphere by Optical, Radio, and Acoustic Radar Techniques," Applied Optics **9,** 1976-1992 (1970).

[10] I. D. Jung, F. X. Kartner, N. Matuschek, D. H. Sutter, F. Morier-Genoud, G. Zhang, U. Keller, V. Scheuer, M. Tilsch and T. Tschudi, "Self-starting 6.5-fs pulses from a Ti:Sapphire laser," Optics Letters **22,** 1009-1011 (1997).

[11] D. Stevenson, B. Agate, X. Tsampoula, P. Fischer, C. T. A. Brown, W. Sibbett, A. Riches, F. Gunn-Moore and K. Dholakia, "Femtosecond optical transfection of cells: viability and efficiency," Optics Express **14,** 7125-7133 (2006).

[12] D. C. Clary, "Femtochemistry and femtobiology - Preface," Chemical Physics **350,** 1-1 (2008).

[13] F. Carbone, P. Baum, P. Rudolf and A. H. Zewail, "Structural preablation dynamics of graphite observed by ultrafast electron crystallography," Physical Review Letters **100,** 035501 (2008).

[14] J. S. Baskin and A. H. Zewail, "Freezing atoms in motion: Principles of femtochemistry and demonstration by laser stroboscopy," Journal of Chemical Education **78,** 737-751 (2001).

[15] A. H. Zewail, "Femtochemistry: Atomic-scale dynamics of the chemical bond," Journal of Physical Chemistry A **104,** 5660-5694 (2000).

[16] D. Huang, E. A. Swanson, C. P. Lin, J. S. Schuman, W. G. Stinson, W. Chang, M. R. Hee, T. Flotte, K. Gregory, C. A. Puliafito and J. G. Fujimoto, "Optical Coherence Tomography," Science **254,** 1178-1181 (1991).

[17] F. H. Loesel, J. P. Fischer, M. H. Götz, C. Horvath, T. Juhasz, F. Noack, N. Suhm and J. F. Bille, "Non-thermal ablation of neural tissue with femtosecond laser pulses," Applied Physics B-Lasers and Optics **66,** 121-128 (1998).

[18] K. Dowling, M. J. Dayel, M. J. Lever, P. M. W. French, J. D. Hares and A. K. L. Dymoke-Bradshaw, "Fluorescence lifetime imaging with picosecond resolution for biomedical applications," Optics Letters **23,** 810-812 (1998).

[19] R. A. Hella, "Material Processing with High-Power Lasers," Optical Engineering **17,** 198-201 (1978).

[20] R. R. Gattass and E. Mazur, "Femtosecond laser micromachining in transparent materials," Nature Photonics **2,** 219-225 (2008).

[21] G. J. Spühler, P. S. Golding, L. Krainer, I. J. Kilburn, P. A. Crosby, M. Brownell, K. J. Weingarten, R. Paschotta, M. Haiml, R. Grange and U. Keller, "Multi-wavelength source with 25 GHz channel spacing tunable over C-band," Electronics Letters **39,** 778-780 (2003).

[22] P. F. Moulton, "Tunable Solid-State Lasers," Proceedings of the IEEE **80,** 348-364 (1992).

[23] T. R. Steele, D. C. Gerstenberger, A. Drobshoff and R. W. Wallace, "Broadly Tunable High-Power Operation of an All-Solid-State Titanium-Doped Sapphire Laser System," Optics Letters **16,** 399-401 (1991).

[24] P. Lacovara, H. K. Choi, C. A. Wang, R. L. Aggarwal and T. Y. Fan, "Room-Temperature Diode-Pumped Yb:YAG Laser," Optics Letters **16,** 1089-1091 (1991).

[25] L. F. Johnson, J. E. Geusic and L. G. Van Uitert, "Coherent Oscillations From Tm^{3+}, Ho^{3+}, Yb^{3+} and Er^{3+} Ions in Yttrium Aluminium Garnet," Applied Physics Letters **7,** 127-129 (1965).

[26] S. A. Payne, L. L. Chase, H. W. Newkirk, L. K. Smith and W. F. Krupke, "$LiCaAlF_6:Cr^{3+}$: a Promising New Solid-State Laser Material," IEEE Journal of Quantum Electronics **24,** 2243-2252 (1988).

[27] R. C. Stoneman and L. Esterowitz, "Efficient, Broadly Tunable, Laser-Pumped Tm-YAG and Tm-YSGG CW Lasers," Optics Letters **15,** 486-488 (1990).

[28] L. Esterowitz, R. Allen, M. Kruer, F. Bartoli, L. S. Goldberg, H. P. Jenssen, A. Linz and V. O. Nicolai, "Blue-Light Emission by a $Pr:LiYF_4$ Laser Operated at Room-Temperature," Journal of Applied Physics **48,** 650-652 (1977).

[29] D. Jaque, J. C. Lagomacini, C. Jacinto and T. Catunda, "Continuous-wave diode-pumped Yb : glass laser with near 90% slope efficiency," Applied Physics Letters **89,** 121101 (2006).

[30] H. Zhang, X. Meng, P. Wang, L. Zhu, X. Liu, R. Cheng, J. Dawes, P. Dekker, S. Zhang and L. Sun, "Slope efficiency of up to 73% for Yb : $Ca_4YO(BO_3)_3$ crystal laser pumped by a laser diode," Applied Physics B-Lasers and Optics **68,** 1147-1149 (1999).

[31] S. Backus, C. G. Durfee, M. M. Murnane and H. C. Kapteyn, "High power ultrafast lasers," Review of Scientific Instruments **69,** 1207-1223 (1998).

[32] R. Paschotta, J. A. der Au, G. J. Spühler, F. Morier-Genoud, R. Hovel, M. Moser, S. Erhard, M. Karszewski, A. Giesen and U. Keller, "Diode-pumped passively mode-locked lasers with high average power," Applied Physics B-Lasers and Optics **70,** S25-S31 (2000).

[33] F. Roser, J. Rothhard, B. Ortac, A. Liem, O. Schmidt, T. Schreiber, J. Limpert and A. Tunnermann, "131 W 220 fs fiber laser system," Optics Letters **30,** 2754-2756 (2005).

[34] E. P. Ostby, L. Yang and K. J. Vahalal, "Ultralow-threshold Yb^{3+}: SiO_2 glass laser fabricated by the solgel process," Optics Letters **32,** 2650-2652 (2007).

[35] L. Yang, T. Carmon, B. Min, S. M. Spillane and K. J. Vahala, "Erbium-doped and Raman microlasers on a silicon chip fabricated by the sol-gel process," Applied Physics Letters **86,** 091114 (2005).

[36] J. J. Zayhowski and P. L. Kelley, "Optimization of Q-Switched Lasers," IEEE Journal of Quantum Electronics **27,** 2220-2225 (1991).

[37] J. J. Degnan, "Optimization of Passively Q-Switched Lasers," IEEE Journal of Quantum Electronics **31,** 1890-1901 (1995).

[38] D. E. Spence, P. N. Kean and W. Sibbett, "60-fsec Pulse Generation from a Self-Mode-Locked Ti-Sapphire Laser," Optics Letters **16,** 42-44 (1991).

[39] F. Krausz, M. E. Fermann, T. Brabec, P. F. Curley, M. Hofer, M. H. Ober, C. Spielmann, E. Wintner and A. J. Schmidt, "Femtosecond Solid-State Lasers," IEEE Journal of Quantum Electronics **28,** 2097-2122 (1992).

[40] R. Yasuhara, T. Kawashima, T. Ikegawa, O. Matsumoto, T. Kurita, T. Sekine, M. Miyamoto, K. Iyama, Y. Tsuchiya, J. Kawanaka, T. Norimatsu, M. Nakatsuka, Y. Izawa and H. Furukawa, "Diode-pumped thermally controlled zig-zag slab laser with 20-J pulse energy in 10 ns at 10-Hz repetition rate," Pacific Rim Conference on Lasers and Electro-Optics**,** 77-78 (2005).

[41] J. Schröder, T. D. Vo and B. J. Eggleton, "Repetition-rate-selective, wavelength-tunable mode-locked laser at up to 640 GHz," Optics Letters **34,** 3902-3904 (2009).

[42] C. T. A. Brown, M. A. Cataluna, A. A. Lagatsky, E. U. Rafailov, M. B. Agate, C. G. Leburn and W. Sibbett, "Compact laser-diode-based femtosecond sources," New Journal of Physics **6** (2004).

[43] U. Keller, "Recent developments in compact ultrafast lasers," Nature **424,** 831-838 (2003).

[44] W. F. Krupke, "Ytterbium solid-state lasers - The first decade," IEEE Journal of Selected Topics in Quantum Electronics **6,** 1287-1296 (2000).

[45] J. Emsley, The Elements, Oxford: Clarendon, 1989

[46] M. C. Wu, N. A. Olsson, D. Sivco and A. Y. Cho, "A 970-nm Strained-Layer InGaAs/GaAlAs Quantum Well Laser for Pumping an Erbium-Doped Optical Fiber Amplifier," Applied Physics Letters **56,** 221-223 (1990).

[47] P. W. Atkins, "Physical Chemistry", Oxford University Press, 5th edition, 1994, p.453

[48] G. Herzberg, Translated by J. W. C. Spinks, "Atomic Spectra and Atomic Structure", Dover Publications, 2nd edition, 1944, p.88

[49] G. Herzberg, Translated by J. W. C. Spinks, "Atomic Spectra and Atomic Structure", Dover Publications, 2nd edition, 1944, p.92&135

[50] T. Taira, W. M. Tulloch and R. L. Byer, "Modeling of quasi-three-level lasers and operation of cw Yb:YAG lasers," Applied Optics **36,** 1867-1874 (1997).

[51] A. Brenier, G. Metrat, N. Muhlstein, F. Bourgeois and G. Boulon, "Growth by the top nucleated floating crystal method and spectroscopic properties of Yb^{3+}-doped $KGd(WO_4)_2$," Optical Materials **16,** 189-192 (2001).

[52] K. Petermann, D. Fagundes-Peters, J. Johannsen, M. Mond, V. Peters, J. J. Romero, S. Kutovoi, J. Speiser and A. Giesen, "Highly Yb-doped oxides for thin-disc lasers," Journal of Crystal Growth **275,** 135-140 (2005).

[53] S. A. Payne, L. K. Smith, L. D. Deloach, W. L. Kway, J. B. Tassano and W. F. Krupke, "Laser, Optical, and Thermomechanical Properties of Yb-Doped Fluorapatite," IEEE Journal of Quantum Electronics **30,** 170-179 (1994).

[54] L. D. DeLoach, S. A. Payne, L. L. Chase, L. K. Smith, W. L. Kway and W. F. Krupke, "Evaluation of Absorption and Emission Properties of Yb^{3+} Doped Crystals for Laser Applications," IEEE Journal of Quantum Electronics **29,** 1179-1191 (1993).

[55] K. I. Schaffers, L. D. DeLoach and S. A. Payne, "Crystal growth, frequency doubling, and infrared laser performance of Yb^{3+}:$BaCaBO_3F$," IEEE Journal of Quantum Electronics **32,** 741-748 (1996).

[56] A. Brenier, "A new evaluation of Yb^{3+}-doped crystals for laser applications," Journal of Luminescence **92,** 199-204 (2001).

[57] N. V. Kuleshov, A. A. Lagatsky, V. G. Shcherbitsky, V. P. Mikhailov, E. Heumann, T. Jensen, A. Diening and G. Huber, "CW laser performance of Yb and Er,Yb doped tungstates," Applied Physics B-Lasers and Optics **64,** 409-413 (1997).

[58] H. Zhang, X. Meng, P. Wang, L. Zhu, X. Liu, R. Cheng, J. Dawes, P. Dekker, S. Zhang and L. Sun, "Slope efficiency of up to 73% for Yb:$Ca_4YO(BO_3)_3$ crystal laser pumped by a laser diode," Applied Physics B-Lasers and Optics **68,** 1147-1149 (1999).

[59] V. E. Kisel, A. E. Troshin, N. A. Tolstik, V. G. Shcherbitsky, N. V. Kuleshov, V. N. Matrosov, T. A. Matrosova and M. I. Kupchenko, "Spectroscopy and continuous-wave diode-pumped laser action of Yb^{3+}:YVO_4," Optics Letters **29,** 2491-2493 (2004).

[60] J. Petit, P. Goldner and B. Viana, "Laser emission with low quantum defect in Yb:$CaGdAlO_4$," Optics Letters **30,** 1345-1347 (2005).

[61] J. Petit, B. Viana, P. Goldner, D. Vivien, P. Louiseau and B. Ferrand, "Laser oscillation with low quantum defect in Yb:$GdVO_4$, a crystal with high thermal conductivity," Optics Letters **29,** 833-835 (2004).

[62] X. Mateos, R. Solé, J. Gavaldà, M. Aguiló, J. Massons, F. Díaz, V. Petrov and U. Griebner, "Crystal growth, spectroscopic studies and laser operation of Yb^{3+}-doped potassium lutetium tungstate," Optical Materials **28,** 519-523 (2006).

[63] A. A. Lagatsky, N. V. Kuleshov and V. P. Mikhailov, "Diode-pumped CW lasing of Yb:KYW and Yb:KGW," Optics Communications **165,** 71-75 (1999).

[64] A. A. Lagatsky, A. Abdolvand and N. V. Kuleshov, "Passive Q switching and self-frequency Raman conversion in a diode-pumped Yb:$KGd(WO_4)_2$ laser," Optics Letters **25,** 616-618 (2000).

[65] F. Brunner, G. J. Spühler, J. A. der Au, L. Krainer, F. Morier-Genoud, R. Paschotta, N. Lichtenstein, S. Weiss, C. Harder, A. A. Lagatsky, A. Abdolvand, N. V. Kuleshov and U. Keller, "Diode-pumped femtosecond Yb:$KGd(WO_4)_2$ laser with 1.1-W average power," Optics Letters **25,** 1119-1121 (2000).

[66] H. Liu, J. Nees and G. Mourou, "Diode-pumped Kerr-lens mode-locked Yb:$KY(WO_4)_2$ laser," Optics Letters **26,** 1723-1725 (2001).

[67] J. H. Liu, U. Griebner, V. Petrov, H. J. Zhang, J. X. Zhang and J. Y. Wang, "Efficient continuous-wave and Q-switched operation of a diode-pumped Yb : $KLu(WO_4)_2$ laser with self-Raman conversion," Optics Letters **30,** 2427-2429 (2005).

[68] A. S. S. de Camargo, I. A. A. Terra, L. A. D. Nunes and M. S. Li, "Energy transfer processes in Yb^{3+}-Tm^{3+} co-doped sodium alumino-phosphate glasses with improved 1.8 μm emission," Journal of Physics-Condensed Matter **20,** 255240 (2008).

[69] R. H. Page, K. I. Schaffers, P. A. Waide, J. B. Tassano, S. A. Payne, W. F. Krupke and W. K. Bischel, "Upconversion-pumped luminescence efficiency of rare-earth-doped hosts sensitized with trivalent ytterbium," Journal of the Optical Society of America B-Optical Physics **15,** 996-1008 (1998).

[70] P. Samuel and S. M. Babu, "Growth and characterization of Ytterbium doped $KGd(WO_4)_2$ single crystal," Crystal Research and Technology **43,** 1036-1040 (2008).

[71] A. A. Lagatsky, C. T. A. Brown and W. Sibbett, "Highly efficient and low threshold diode-pumped Kerr-lens mode-locked Yb:KYW laser," Optics Express **12,** 3928-3933 (2004).

[72] R. C. J. Draper, "Crystal Pulling", Pergamon Press, B. R. Pamplin, 1st Edition, 1975, Crystal Growth, p.497

[73] C. Pujol, M. Aguiló, F. Díaz and C. Zaldo, "Growth and characterisation of monoclinic $KGd_{1-x}RE_x(WO_4)_2$ single crystals," Optical Materials **13,** 33-40 (1999).

[74] J. Viscakas, I. Mochalov, A. Mikhailov, R. Klevtsova and A. Liubimov, "$KGd(WO_4)_2$ crystal structure and Raman scattering," Lietuvos Fizikaos Rinkinys **28,** 224 (1988).

[75] M. C. Pujol, R. Solé, J. Massons, J. Gavaldà, X. Solans, C. Zaldo, F. Díaz and M. Aguiló, "Structural study of monoclinic $KGd(WO_4)_2$ and effects of lanthanide substitution," Journal of Applied Crystallography **34,** 1-6 (2001).

[76] L. Macalik, J. Hanuza and A. A. Kaminskii, "Polarized infrared and Raman spectra of $KGd(WO_4)_2$ and their interpretation based on normal coordinate analysis," Journal of Raman Spectroscopy **33,** 92-103 (2002).

[77] A. A. Kaminskii, A. F. Konstantinova, V. P. Orekhova, A. V. Butashin, R. F. Klevtsova and A. A. Pavlyuk, "Optical and nonlinear laser properties of the χ^3 Active monoclinic α-$KY(WO_4)_2$ crystals," Crystallography Reports **46,** 665-672 (2001).

[78] L. Macalik, J. Hanuza and A. A. Kaminskii, "Polarized Raman spectra of the oriented $NaY(WO_4)_2$ and $KY(WO_4)_2$ single crystals," Journal of Molecular Structure **555,** 289-297 (2000).

[79] R. D. Shannon, "Revised effective ionic radii and systematic studies of interatomic distances in halides and chalcogenides," Acta Crystallographica Section A **32,** 751-767 (1976).

[80] M. C. Pujol, X. Mateos, R. Solé, J. Massons, J. Gavaldà, F. Díaz and M. Aguiló, "Materials Science Forum","Linear thermal expansion tensor in $KRE(WO_4)_2$ (RE=Gd, Y, Er, Yb) monoclinic crystals", Trans Tech

Publications Ltd, 2001, Epdic 7: European Powder Diffraction, Pts 1 and 2, 378-3, p.710-715

[81] V. Petrov, F. Guell, J. Massons, J. Gavaldà, R. M. Solé, M. Aguiló, F. Díaz and U. Griebner, "Efficient tunable laser operation of Tm : $KGd(WO_4)_2$ in the continuous-wave regime at room temperature," IEEE Journal of Quantum Electronics **40,** 1244-1251 (2004).

[82] F. Gardíllou, Y. E. Romanyuk, C. N. Borca, R. P. Salathé and M. Pollnau, "Lu, Gd codoped $KY(WO_4)_2$:Yb epitaxial layers: towards integrated optics based on $KY(WO_4)_2$," Optics Letters **32,** 488-490 (2007).

[83] I. V. Mochalov, "Laser and nonlinear properties of the potassium gadolinium tungstate laser crystal $KGd(WO_4)_2:Nd^{3+}$ (KGW:Nd)," Optical Engineering **36,** 1660-1669 (1997).

[84] S. Biswal, S. P. O'Connor and S. R. Bowman, "Thermo-optical parameters measured in ytterbium-doped potassium gadolinium tungstate," Applied Optics **44,** 3093-3097 (2005).

[85] M. C. Pujol, M. Rico, C. Zaldo, R. Solé, V. Nikolov, X. Solans, M. Aguiló and F. Díaz, "Crystalline structure and optical spectroscopy of Er^{3+}-doped $KGd(WO_4)_2$ single crystals," Applied Physics B-Lasers and Optics **68,** 187-197 (1999).

[86] M. C. Pujol, X. Mateos, R. Solé, J. Massons, J. Gavaldà, X. Solans, F. Díaz and M. Aguiló, "Structure, crystal growth and physical anisotropy of $KYb(WO_4)_2$, a new laser matrix," Journal of Applied Crystallography **35,** 108-112 (2002).

[87] A. Major, I. Nikolakakos, J. S. Aitchison, A. I. Ferguson, N. Langford and P. W. E. Smith, "Characterization of the nonlinear refractive index of the laser crystal Yb : $KGd(WO_4)_2$," Applied Physics B-Lasers and Optics **77,** 433-436 (2003).

[88] N. Thilmann, G. Stromqvist, M. C. Pujol, V. Pasiskevicius, V. Petrov and F. Díaz, "Nonlinear refractive indices in Yb3+-doped and undoped monoclinic double tungstates $KRE(WO_4)_2$ where RE=Gd, Y, Yb, Lu," Applied Physics B-Lasers and Optics **96,** 385-392 (2009).

[89] A. Major, F. Yoshino, I. Nikolakakos, J. S. Aitchison and P. W. E. Smith, "Dispersion of the nonlinear refractive index in sapphire," Optics Letters **29,** 602-604 (2004).

[90] N. V. Kuleshov, A. A. Lagatsky, A. V. Podlipensky, V. P. Mikhailov and G. Huber, "Pulsed laser operation of Yb-doped $KY(WO_4)_2$ and $KGd(WO_4)_2$," Optics Letters **22,** 1317-1319 (1997).

[91] G. Paunescu, J. Hein and R. Sauerbrey, "100-fs diode-pumped Yb : KGW mode-locked laser," Applied Physics B-Lasers and Optics **79,** 555-558 (2004).

[92] A. Schmidt, S. Rivier, W. B. Cho, J. H. Yim, S. Y. Choi, S. Lee, F. Rotermund, D. Rytz, G. Steinmeyer, V. Petrov and U. Griebner, "Sub-100 fs single-walled carbon nanotube saturable absorber mode-locked Yb-laser operation near 1 μm," Optics Express **17,** 20109-20116 (2009).

[93] G. R. Holtom, "Mode-locked Yb : KGW laser longitudinally pumped by polarization-coupled diode bars," Optics Letters **31,** 2719-2721 (2006).

[94] M. Pollnau, Y. E. Romanyuk, F. Gardíllou, C. N. Borca, U. Griebner, S. Rivier and V. Petrov, "Double tungstate lasers: From bulk toward on-chip integrated waveguide devices," IEEE Journal of Selected Topics in Quantum Electronics **13,** 661-671 (2007).

[95] Y. E. Romanyuk, C. N. Borca, M. Pollnau, S. Rivier, V. Petrov and U. Griebner, "Yb-doped $KY(WO_4)_2$ planar waveguide laser," Optics Letters **31,** 53-55 (2006).

[96] F. M. Bain, A. A. Lagatsky, S. V. Kurilchick, V. E. Kisel, S. A. Guretsky, A. M. Luginets, N. A. Kalanda, I. M. Kolesova, N. V. Kuleshov, W. Sibbett and C. T. A. Brown, "Continuous-wave and Q-switched operation of a compact, diode-pumped Yb^{3+}:$KY(WO_4)_2$ planar waveguide laser," Optics Express **17,** 1666-1670 (2009).

[97] D. Geskus, S. Aravazhi, E. Bernhardi, C. Grivas, S. Harkema, K. Hametner, D. Günther, K. Wörhoff and M. Pollnau, "Low-threshold, highly efficient Gd^{3+}, Lu^{3+} co-doped $KY(WO_4)_2$:Yb^{3+} planar waveguide lasers," Laser Physics Letters **6,** 800-805 (2009).

[98] T. Y. Fan and R. L. Byer, "Modeling and CW Operation of a Quasi-Three-Level 946 nm Nd:YAG Laser," IEEE Journal of Quantum Electronics **23,** 605-612 (1987).

[99] A. E. Siegman, "Lasers", University Science Books, 1986, p.1004

[100] A. E. Siegman, "Lasers", University Science Books, 1986, p.1041&1104

[101] A. E. Siegman, "Lasers", University Science Books, 1986, p.1007

[102] R. L. Fork, O. E. Martinez and J. P. Gordon, "Negative Dispersion Using Pairs of Prisms," Optics Letters **9,** 150-152 (1984).

[103] G. H. C. New, "Pulse Evolution in Mode-Locked Quasicontinuous Lasers," IEEE Journal of Quantum Electronics **QE10,** 115-124 (1974).

[104] A. E. Siegman, "Lasers", University Science Books, 1986, p.1104-1128

[105] U. Keller, D. A. B. Miller, G. D. Boyd, T. H. Chiu, J. F. Ferguson and M. T. Asom, "Solid-State Low-Loss Intracavity Saturable Absorber for Nd-YLF Lasers - an Antiresonant Semiconductor Fabry-Perot Saturable Absorber," Optics Letters **17,** 505-507 (1992).

[106] D. L. Lee, "Electromagnetic Principles of Integrated Optics", John Wiley and Sons, 1986

[107] A. W. Snyder and J. D. Love, "Optical Waveguide Theory", Chapman and Hall, 1983

[108] D. L. Lee, "Electromagnetic Principles of Integrated Optics", John Wiley and Sons, 1986, p.67-73

[109] D. L. Lee, "Electromagnetic Principles of Integrated Optics", John Wiley and Sons, 1986, p.92

[110] D. L. Lee, "Electromagnetic Principles of Integrated Optics", John Wiley and Sons, 1986, p.295-297

[111] A. W. Snyder and J. D. Love, "Optical Waveguide Theory", Chapman and Hall, 1983, p.252-257

[112] M. Pollnau and Y. E. Romanyuk, "Optical waveguides in laser crystals," Comptes Rendus Physique **8,** 123-137 (2007).

[113] C. T. A. Brown, C. L. Bonner, T. J. Warburton, D. P. Shepherd, A. C. Tropper, D. C. Hanna and H. E. Meissner, "Thermally bonded planar waveguide lasers," Applied Physics Letters **71,** 1139-1141 (1997).

[114] B. Ferrand, B. Chambaz and M. Couchaud, "Liquid phase epitaxy: A versatile technique for the development of miniature optical components in single crystal dielectric media," Optical Materials **11,** 101-114 (1999).

[115] I. Chartier, B. Ferrand, D. Pelenc, S. J. Field, D. C. Hanna, A. C. Large, D. P. Shepherd and A. C. Tropper, "Growth and Low-Threshold Laser Oscillation of an Epitaxially Grown Nd Yag Wave-Guide," Optics Letters **17,** 810-812 (1992).

[116] P. D. Townsend, "Optical Effects of Ion-Implantation," Reports on Progress in Physics **50,** 501-558 (1987).

[117] S. J. Field, D. C. Hanna, D. P. Shepherd, A. C. Tropper, P. J. Chandler, P. D. Townsend and L. Zhang, "Ion-Implanted Nd-YAG Wave-Guide Lasers," IEEE Journal of Quantum Electronics **27,** 428-433 (1991).

[118] L. Laversenne, P. Hoffmann, M. Pollnau, P. Moretti and J. Mugnier, "Designable buried waveguides in sapphire by proton implantation," Applied Physics Letters **85,** 5167-5169 (2004).

[119] K. M. Davis, K. Miura, N. Sugimoto and K. Hirao, "Writing waveguides in glass with a femtosecond laser," Optics Letters **21,** 1729-1731 (1996).

[120] V. Apostolopoulos, L. Laversenne, T. Colomb, C. Depeursinge, R. P. Salathe, M. Pollnau, R. Osellame, G. Cerullo and P. Laporta, "Femtosecond-irradiation-induced refractive-index changes and channel waveguiding in bulk Ti^{3+}:Sapphire," Applied Physics Letters **85,** 1122-1124 (2004).

[121] R. Osellame, M. Lobino, N. Chiodo, M. Marangoni, G. Cerullo, R. Ramponi, H. T. Bookey, R. R. Thomson, N. D. Psaila and A. K. Kar, "Femtosecond laser writing of waveguides in periodically poled lithium niobate preserving the nonlinear coefficient," Applied Physics Letters **90,** 241107-241109 (2007).

Chapter 2

Experimental Techniques

2.1 Introduction

Several experimental techniques which were performed during this thesis were common to multiple experiments. To save on repetition these techniques are described within this chapter. When appropriate more detailed descriptions of set-ups and methods are contained within the experimental chapter concerned. The chapter begins with a description of the set-up used for channel waveguide fabrication. Procedures used to construct lasers and measurements concerned with laser performance are then explained. Finally methods for loss measurements are described.

2.2 Ultrafast Laser Inscription

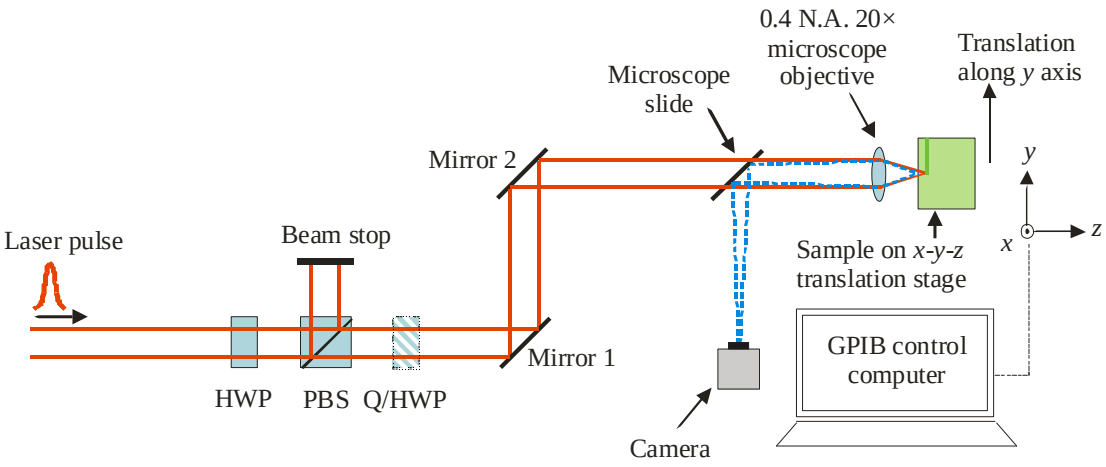

Fig. 2.1. Ultrafast laser writing set-up as used at Heriot Watt University to inscribe channel waveguides. (Q/H)WP = (quarter/half-)waveplate; PBS = polarising beamsplitter.

The channel waveguides that are presented in this work were fabricated by ULI through a collaboration with Heriot Watt University. All waveguide inscription was carried out on a set-up illustrated in fig. 2.1. An ultrafast laser source was passed through a half-waveplate placed in combination with a polarising beamsplitter. This allowed the incident pulse energy to be easily controlled by rotation of the waveplate.

A further waveplate was sometimes inserted, as shown in the diagram, so that various polarisation states could be used to write the waveguides. Two mirrors aligned the writing beam's path and a microscope objective focused the pulses into the material. A microscope slide was used to reflect a small portion of the reflected light into a camera to provide an image of the facet. This monitored the writing beam's size and ensured the beam was kept at a constant depth within the material. The sample itself was mounted on a motorised high precision *x-y-z* stage connected to a computer and this was used to translate the sample along the laser focus at a range of translation speeds.

Two laser sources were used during waveguide writing experiments. The first, which was used to create the channel waveguides described in section 3.6, was a regeneratively amplified Ti:sapphire laser. This produced 130 fs pulses centred on 800 nm at a 5 kHz repetition rate. An adjustable slit was used in combination with a 0.4 N.A. (20×) objective to focus the pulses into the crystal. This was able to create waveguides with a symmetric cross-section. The second source, which was used to fabricate channel waveguides in Yb:KGdW and Yb:KYW as described in Chapter 5, was an Yb:fibre laser (*Fianium Ltd.*). This operated at a 500 kHz repetition rate delivering 1.3 ps pulses at 1064 nm.

2.3 Laser Design and Performance

2.3.1 Laser Pump Source

All lasers built in this work required a pump source at 980 nm which was readily provided by compact and efficient InGaAs laser diodes. The laser diode used as a pump source for all lasing experiments, and for some waveguide loss characterisation measurements, was a *JDS Uniphase* InGaAs fibre-coupled laser diode, which provided almost 500 mW when a forward current of 850 mA was applied. The output power of the laser diode as a function of current is shown in fig. 2.2. The output from the fibre was a diffraction limited fundamental Gaussian mode (i.e M^2 of 1) and was linearly polarised. The fibre was mounted together with a microscope objective on an *x-y-z* fibre mount stage, and by using pinholes for alignment the pump output could be

collimated. This beam was passed through a half-waveplate which was rotated to obtain horizontal polarisation. For waveguide laser cavities a Faraday Isolator was inserted into the beam path at this point to prevent any back-reflections from damaging the laser diode. A further half-waveplate could also be inserted after the Faraday Isolator so that various pumping polarisations could be investigated. A lens or microscope objective was then placed in the beam path, mounted on an *x*-*y*-*z* stage, to focus the pump beam into the laser gain medium.

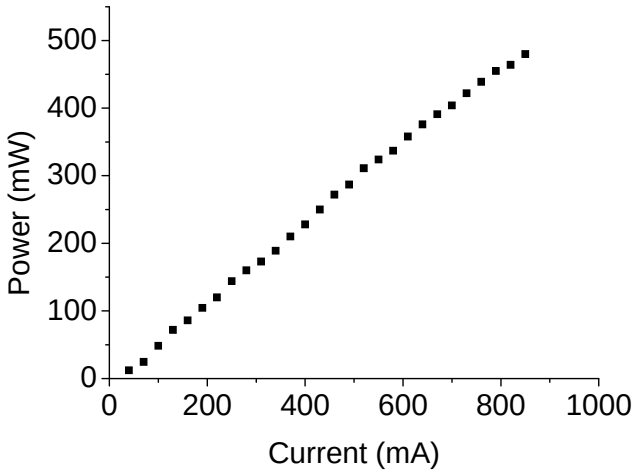

Fig. 2.2. Output power of InGaAs laser diode.

2.3.2 Asymmetric Z-fold Cavities

When building a laser cavity with low thresholds and high slope efficiency it is necessary to have high pump and laser mode overlap within the gain medium, together with tight foci. In a bulk laser medium tight foci are typically achieved using a four mirror asymmetric z-fold cavity, which is illustrated in fig. 2.3, where M_1 and M_2 are curved mirrors. Using this design a further focus of the laser mode is formed at the end mirror, M_3, of the short arm. This is particularly advantageous in cavities which employ a SESAM for mode locking, as high fluences are required on the SESAM and this can be obtained by replacing M_3 with the SESAM. The long arm is collimated making the beam from this arm suitable for use as the cavity output. Intra-cavity elements, such as prisms for the compensation of dispersion, can also be easily inserted in this arm. Brewster cut crystals are usually used as the gain material, resulting in no Fresnel loss, but the angled crystal introduces astigmatism to the

cavity. However, by carefully choosing the angles of the folding mirrors this astigmatism can be completely compensated for.

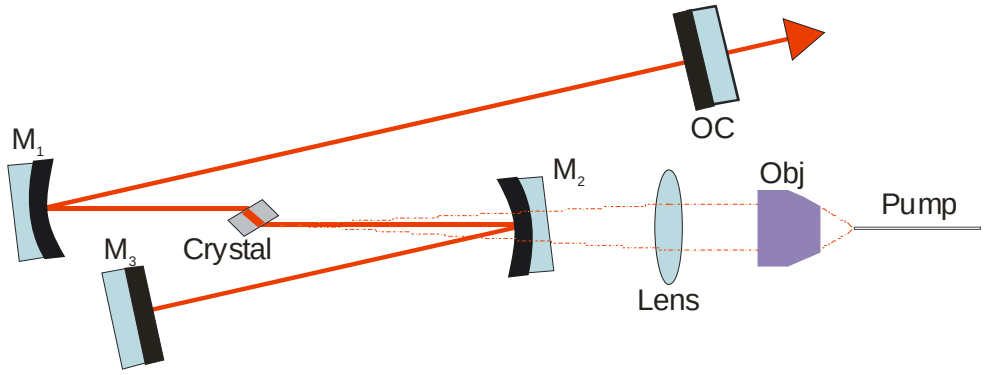

Fig. 2.3. Z-fold cavity configuration consisting of 2 curved mirrors, M_1 and M_2, an end mirror, M_3, and an output coupler (OC). An objective (Obj) and lens collimate and refocus the pump beam into the crystal. In this design, a focus is formed on M_3 which van be replaced by a SESAM for mode-locking experiments.

The z-fold cavity designs used in this thesis were calculated using the programme *LCAV* to ascertain the positions and angles of mirrors to be used together with the cavity mode sizes along the length of the cavity. These calculations used standard ABCD matrices for Gaussian beams travelling through optical elements [1].

2.3.3 Waveguide Cavities

One of the significant advantages of using waveguides as laser gain media is the opportunity to form compact laser geometries. Thus for the waveguide lasers built in this thesis simple monolithic two mirror cavities were constructed using plane-plane mirrors, as illustrated in fig. 2.4. Thin fused silica substrates, coated for high reflectivity at 1040 nm, and also high transmission at 980 nm for the case of the pump input mirror (M_1), were used as these could be directly attached to the end facets of the waveguide. They were typically held to the crystal facets using surface tension provided by a thin layer of fluorinert liquid (n = 1.303), but they could also be mounted on *x-y-z* stages and held against the waveguide end facets directly. Transmission of the mirrors was recorded for different mounting methods, as the refractive index boundary affects the reflectivity. The crystal was typically mounted

on a copper block, but no additional active cooling of the sample was found to be necessary. The waveguide was mounted on an *x*-*y*-*φ*-*θ* stage for alignment. An anti-reflection coated objective placed after the waveguide collected the output from the waveguide. For characterisation of lasing performance a dichroic mirror, which reflected light from 1010 nm – 1100 nm whilst transmitting 980 nm, allowed the laser output to be separated from any residual pump. To image the end facet of the waveguide and provide information about guiding behaviour a ×50 long working distance (20 mm) objective was mounted together with a silicon-based CCD camera. The long working distance objective allowed images to be viewed easily without impinging on other mounts. Images were typically taken of the end facet to determine the position and profile of the guided mode, but images from above were also viewed, showing the propagation of the light along the waveguide. This view was particularly useful when aligning the pump with the waveguide.

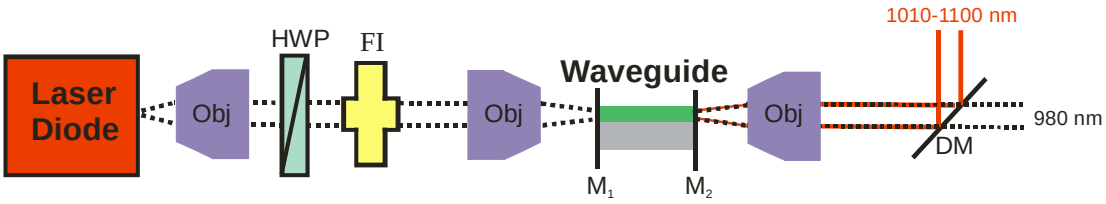

Fig. 2.4. Geometry of waveguide laser cavity. Obj = objective; HWP = half-waveplate; FI = Faraday isolator; M = mirror; DM = dichroic mirror. Objectives were mounted on *x*-*y*-*z* stages whilst the waveguide was mounted on an *x*-*z*-*φ*-*θ* stage.

2.3.4 Absorbed Pump Power

An upper limit on the absorbed pump power was calculated by comparing the throughput power when launched into the doped region to that of the bulk undoped region in a similar way to that described by Pelenc *et al*. [2]. The transmitted pump power, P_{t_guide}, through the waveguide region is:

$$P_{t\_guide} = P_i T_{obj} T_F^{\,2} (1 - \delta_{launch} A) \qquad \text{Eq. 2.1}$$

Where P_i is the incident power, which is taken as the power after the Faraday Isolator; T_{obj} is the transmission of the objective; T_F is the transmission of the end facets; δ_{launch}

is the launch efficiency; and A is the single pass absorption. The power transmitted through the undoped bulk region is related to the incident power by the equation:

$$P_{t\_bulk} = P_i T_{obj} T_F{}^2 \qquad \text{Eq. 2.2}$$

In the case of single pass absorption the absorbed pump power can then be easily found using the equation:

$$P_a = P_i T_{obj} (1 - R_1) \delta_{launch} A \qquad \text{Eq. 2.3}$$

Where R_1 is the reflectivity of the incident mirror at the pump wavelength.

However, in the case of high reflection of the pump at the second facet then the second, third and subsequent pass absorption of the pump must be considered. The absorbed pump power is then represented by the relationship:

$$P_a = P_i T_{obj} (1 - R_1) \delta_{launch} A \left[1 + (1 - A) R_2 + (1 - A^2) R_2 R_1 + (1 - A)^3 R_2{}^2 R_1 + (1 - A)^4 R_2{}^2 R_1{}^2 + \ldots \right] \qquad \text{Eq. 2.4}$$

To calculate this accurately the launch efficiency and single pass absorption must be separable from one another, but in practice these are difficult to separate. Thus, instead, an upper limit for absorbed pump was calculated by assuming 100 % launch efficiency, where $\delta_{launch} = 1$ and thus δ_{launch}, can simply be removed from the equation leaving:

$$P_a = P_i T_{obj} (1 - R_1) A \left[1 + (1 - A) R_2 + (1 - A^2) R_2 R_1 + (1 - A)^3 R_2{}^2 R_1 + (1 - A)^4 R_2{}^2 R_1{}^2 + \ldots \right] \qquad \text{Eq. 2.5}$$

This equation is used in Chapter 4 to calculate the absorbed pump powers in low loss planar waveguides.

2.3.5 Laser Performance

There are several measurements which are usually taken to assess the performance of a laser. Firstly laser threshold must be reached and in order to identify threshold a large area (5×5 mm^2) *New Focus* Germanium detector was used. This was connected to an oscilloscope which was triggered by a chopper inserted into the path of the pump beam. The chopper was not strictly necessary but was useful to differentiate between the luminescence and lasing. Once lasing threshold was reached and optimised the output power had to be determined and maximised, and this was easily done using a power meter. The pump power was then gradually decreased and the corresponding output power measured, allowing the slope efficiency of the laser to be determined. The wavelength of the laser was measured with an *IST-Rees* spectrum analyser. For *Q*-switched performance, pulse duration could simply be determined using the *New Focus* detector and a 2 GHz oscilloscope, as the response time of the detector and the bandwidth of the oscilloscope were suitable for the measurement of the ns pulses which were produced. Mode-locked pulse durations were measured with a non-collinear intensity autocorrelator, while the repetition rate could be measured using an RF-spectrum analyser.

A further important laser characteristic is the beam quality. This is usually quoted in terms of the beam's M^2 value, which is a factor determining the divergence of the laser beam compared to the diffraction of a fundamental diffraction limited mode. The waist of a beam as it propagates through a focus is given by [3]:

$$w(z) = w_0 \sqrt{\left[1 + \left(M^2 \frac{z}{z_R}\right)^2\right]} \qquad \text{Eq. 2.6}$$

where w_0 is the beam waist at the focus, z is the propagation distance and z_R is the Rayleigh range given by:

$$z_R = \frac{\pi w_0^{\,2}}{\lambda} \qquad \text{Eq. 2.7}$$

These values are illustrated in fig. 2.5.

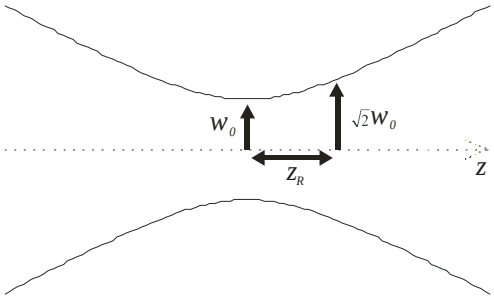

Fig. 2.5. Gaussian beam propagation along z where w_0 is the beam waist at the focus and z_R is the Rayleigh range.

Thus M^2 of the beams used in this thesis can be determined by finding the value of M^2 which fits the above function to the experimental data concerned. When measuring this value the beam waist must, of course, be known and therefore it is important that the waist of a beam is defined. Many definitions for beam waists are employed, but for M^2 measurements to be strictly accurate the second moment of the beam is required [3]. The second moment of a beam along x (or alternatively along y) with an intensity profile $I(x,y)$ is defined in equation 2.8 where x_0 is the centre of gravity of the beam.

$$\sigma_x^2 = \frac{\int_{-\infty}^{\infty} (x - x_0)^2 I(x,y)\,dxdy}{\int_{-\infty}^{\infty} I(x,y)\,dxdy} \qquad \text{Eq. 2.8}$$

This measurement is very sensitive to noise, making it very difficult to perform accurately. For Gaussian beams the second moment beam radius corresponds to the beam radius at e^{-2} intensity. This can be determined very easily with most beam profilers, and this definition is thus widely used when measuring M^2. Therefore in this thesis M^2 was measured based on the e^{-2} definition of beam waist for Gaussian beams. For beams which strongly deviated from a Gaussian precise values of M^2 are not given but comments on the beam quality are provided.

2.3.6 Caird Plots

The slope efficiency of a laser depends on the round-trip cavity losses, including output coupling transmission. Different output couplers therefore typically give different slope efficiencies. Consequently, by measuring the slope efficiency obtained with different output couplers, it is possible to calculate the propagation losses in the laser by means of the Caird plot [4] which uses the relation:

$$\eta = \eta_0 \frac{T_{OC}}{T_{OC} + \delta} \qquad \text{Eq. 2.9}$$

where T_{OC} is transmission of output coupler, δ represents round-trip propagation losses, excluding output coupling, η is the slope efficiency, and η_0 is the intrinsic slope efficiency, which is the maximum slope efficiency theoretically possible with no losses in the cavity. This can be simply rearranged into the common format used to represent a straight line:

$$\frac{1}{\eta} = \frac{1}{\eta_0} + \frac{\delta}{\eta_0}\frac{1}{T_{OC}} \qquad \text{Eq. 2.10}$$

Thus by plotting $1/\eta$ against $1/T_{OC}$ it is possible to find η_0 based on the intercept and with this to find δ based on the gradient of the slope. Unlike Findlay-Clay analysis [5], this method has little dependence on re-absorption losses [6], and is thus a useful technique for estimating losses in a quasi-three-level laser such as the Yb systems investigated in this thesis.

2.4 Waveguide Loss Measurements

The insertion loss of a waveguide, δ_{ins}, can be given by Eq. 2.11, where the same notation is used as in Eq. 2.1.

$$\delta_{ins} = 1 - \frac{P_{t\_guide}}{P_i} \qquad \text{Eq. 2.11}$$

Insertion loss is typically made up of several contributing factors – Fresnel loss, R_F (where this is equal to $1-T_F$); absorption loss, A; coupling loss, δ_{coup}; and propagation loss, δ_{prop}. Fresnel loss can be easily determined from the refractive indices of the materials involved and the angles of incidence of the beams. Fresnel losses, R_F, are given by [7]:

$$R_{pi} = \left[\frac{n_1 \cos(\theta_2) - n_2 \cos(\theta_1)}{n_1 \cos(\theta_2) + n_2 \cos(\theta_1)} \right]^2 \qquad \text{Eq. 2.12}$$

And

$$R_s = \left[\frac{n_1 \cos(\theta_1) - n_2 \cos(\theta_2)}{n_1 \cos(\theta_1) + n_2 \cos(\theta_2)} \right]^2 \qquad \text{Eq. 2.13}$$

for pi and sigma polarised light respectively. Here, n is refractive index, θ is angle and 1 corresponds to the first material whilst 2 corresponds to the second material. For waveguide geometries normal incidence is used and so for both polarisations R_F is given by:

$$R_{pi} = R_s = \left[\frac{n_1 - n_2}{n_1 - n_2} \right]^2 \qquad \text{Eq. 2.14}$$

Once the Fresnel reflection loss is determined it can be subtracted from the insertion loss. When calculating losses it is convenient to work in decibels. A power ratio can be easily converted to decibels using:

$$\alpha_{dB} = -10 \log_{10} \left(\frac{P_t}{P_i} \right) \qquad \text{Eq. 2.15}$$

Absorption losses can be determined from the absorption cross section of the material, or alternatively measurements are often made at a wavelength of negligible absorption, leaving only coupling and propagation losses.

Difficulty arises when trying to separate coupling loss and propagation loss. A typical method for determining propagation loss is the cut-back technique [8], where insertion losses are measured for various sample lengths by cutting the sample back. If identical coupling schemes are used for each sample length then the propagation losses can be determined independently from the coupling loss. However, the major drawback of this technique is that it requires samples which are dispensable. Unfortunately the samples used in this work are unique and precious, and so the cut-back method was not suitable. Other techniques which can be used include scattering loss measurements [9] and Fabry-Perot fringe contrast measurements [10], neither of which are straightforward measurements. A simple method which was implemented was a straightforward transmission measurement. Although this includes coupling loss it was possible to minimise this contribution by experimenting with various coupling optics. The set-up used for this is described below. A second method which was used was the luminescence decay method [11] which is a particularly attractive technique as it is independent of coupling loss and can be used to measure losses over a broad wavelength range with only one run of measurements. The set-up used for this technique is described in section 2.4.2.

2.4.1 Transmission Method

The transmission loss method is perhaps the simplest method, where a light source is coupled into the waveguide and the transmitted power is measured. In cases where light which has not travelled through the waveguide is able to reach the detector a pinhole is used to block this contribution. Absorption and Fresnel losses are accounted for, leaving a measurement of the combined coupling, and propagation loss. Various input coupling optics are used until the measured loss is minimised. At this point the coupling efficiency is assumed to be 100 %, giving an upper limit for the propagation loss. Losses can be determined by this method at any wavelength for which there is a suitable source. The sources used throughout this work were: an InGaAs laser diode operating at 980 nm as described in section 2.3.1; a 1064 nm Nd:YVO_4 laser; a tunable fibre coupled laser source operating around 1300 nm; and a fibre coupled source of 1550 nm amplified spontaneous emission (ASE).

2.4.2 Luminescence Decay Method

The luminescence decay method involves face-pumping a small cross-section of the channel waveguide. The luminescence from this excited spot must travel along the length of the waveguide at which point it is collected and detected with an optical spectrum analyser (OSA). By translating the position of the pump along the length of the waveguide it is possible to change the position of the excited spot in the waveguide. Thus the excited luminescence has to propagate along different lengths of waveguide before reaching the detector and a signal which varies exponentially as a function of length is recorded. Assuming the coupling is identical for each excited spot then this gives a measurement which depends only on propagation loss and this can be extracted from the exponential decay.

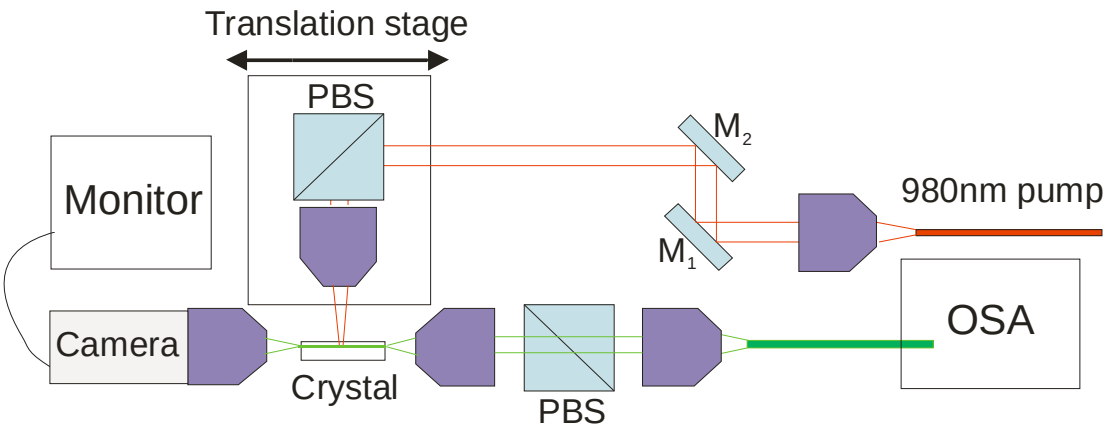

Fig. 2.6. Set-up used for luminescence decay loss measurements. M = mirror; PBS = polarising beam splitter; OSA = optical spectrum analyser.

The set-up used to perform this measurement is shown in fig. 2.6. The 980 nm InGaAs laser diode described in section 2.3.1 was used as a pump source. This was collimated with a 30× objective and steered along a straight path from M_2 which was aligned using pinholes together with mirrors M_1 and M_2. A polarising beamsplitter was used as a third mirror to deflect the beam by 90° into a 10× objective which focused the pump into a small section of the waveguide. The polarising beamsplitter and 10× objective were mounted together on a translation stage, so that the position of waveguide cross-section excitation could be varied. At one end of the waveguide an imaging system was set up, using the standard 50× long working distance objective

and CCD camera with monitor as described in section 2.3.3. This was to ensure accurate alignment and identification of the structure. At the other end facet of the waveguide the signal was collected with a standard 20× objective and passed through a polarising beam splitter. This allowed the losses to be determined for polarisation along different axes. The luminescence was then coupled into a single mode fibre using a 30× objective and detected by an OSA.

Steps were taken to ensure minimal background luminescence from outside the waveguide cross-section was able to reach the detector. Firstly, prior to pumping and detecting the luminescence signal, the optical fibre was disconnected from the OSA and was instead used to deliver a fibre coupled 1300 nm source to the sample. The guided mode was viewed with a camera. This ensured optimal alignment of the microscope objectives and fibre with the waveguide, minimising coupling loss such that close to 100 % of the luminescence from the waveguide, together with minimal background light, was detected by the OSA. To confirm that this was indeed the case, when initially taking measurements a polarising maintaining fibre was also alternatively placed against the waveguide facet to collect the luminescence. This had a mode size of 3.3 μm e^{-2} radius, and therefore ensured only light which propagated along the waveguide was detected. Crucially, although returning a noisier signal, this gave a result with the same decay curve confirming the validity of the measurements obtained using bulk optics.

2.5 Conclusions

This chapter has described many of the experimental techniques which have been used in subsequent chapters to obtain the presented results. The set-up used at Heriot Watt University to fabricate channel waveguides was described, and this set-up was used to create the waveguides presented in Chapter 3 and Chapter 5. The laser source described in section 2.3.1 was used extensively for various experiments, from pumping to characterising waveguide losses. Bulk laser cavities, as described in section 2.3.2 were used in Chapters 3 and 4, whilst waveguide laser geometries were used for experiments in Chapters 4 and 5. Finally several methods for estimating losses were described and these techniques have been used throughout this thesis.

2.6 References

[1] H. Kogelnik and T. Li, "Laser Beams and Resonators," Applied Optics **5,** 1550-1567 (1966).

[2] D. Pelenc, B. Chambaz, I. Chartier, B. Ferrand, C. Wyon, D. P. Shepherd, D. C. Hanna, A. C. Large and A. C. Tropper, "High Slope Efficiency and Low-Threshold in a Diode-Pumped Epitaxially Grown Yb:YAG Wave-Guide Laser," Optics Communications **115,** 491-497 (1995).

[3] A. E. Siegman, "How to (Maybe) Measure Laser Beam Quality", Stanford University, 1997

[4] J. A. Caird, S. A. Payne, P. R. Staver, A. J. Ramponi, L. L. Chase and W. F. Krupke, "Quantum Electronic-Properties of the $Na_3Ga_2Li_3F_{12}:Cr^{3+}$ Laser," IEEE Journal of Quantum Electronics **24,** 1077-1099 (1988).

[5] D. Findlay and R. A. Clay, "The Measurement of Internal Losses in 4-Level Lasers," Physics Letters **20,** 277-278 (1966).

[6] S. A. Payne, L. L. Chase, H. W. Newkirk, L. K. Smith and W. F. Krupke, "$LiCaAlF_6:Cr^{3+}$: a Promising New Solid-State Laser Material," IEEE Journal of Quantum Electronics **24,** 2243-2252 (1988).

[7] E. Hecht, "Optics", Addison-Wesley, 2nd edition, 1990, p.95-102

[8] R. G. Hunsperger, "Integrated Optics, Theory and Technology", Springer-Verlag, 1982, p.83-85

[9] Y. Okamura, S. Yoshinaka and S. Yamamoto, "Measuring Mode Propagation Losses of Integrated Optical-Waveguides - a Simple Method," Applied Optics **22,** 3892-3894 (1983).

[10] R. Regener and W. Sohler, "Loss in Low-Finesse Ti-$LiNBO_3$ Optical Wave-Guide Resonators," Applied Physics B-Photophysics and Laser Chemistry **36,** 143-147 (1985).

[11] P. C. Mogensen, P. M. Smowton and P. Blood, "Measurement of optical mode loss in visible emitting lasers," Applied Physics Letters **71,** 1975-1977 (1997).

Chapter 3
Quantum Dot Saturable Absorbers

3.1 Introduction

The advantages and applications of compact ultrashort pulsed lasers around 1 micron have been outlined in Chapter 1. The constraints on the cavity design in KLM make this an unsuitable method for the generation of ultrashort pulses from a monolithic Yb:tungstate waveguide laser, limiting the suitability of this technique for the generation of efficient, compact and user friendly ultrafast laser sources. SESAMs, however, can generate self-starting mode locking and can be simply inserted into the cavity of a suitable laser to produce ultrashort pulses. The only constraint on cavity design is that the SESAM is placed at a position in the cavity where there is high fluence, i.e. where the laser spot size is small so as to fully saturate the device. This can be readily satisfied in a channel waveguide laser with its tightly confined operating mode, and thus SESAMs are inherently suitable for integration with waveguide lasers.

In this chapter a novel quantum dot (QD)-SESAM is described and characterised. This QD-SESAM was used to generate fs pulses from a standard z-fold Yb:KYW resonator [1]. Although this SESAM was used to mode lock a traditional bulk Yb:tungstate laser, in principle such SESAMs can also be integrated with waveguide lasers to support fs pulses, showing the potential of these devices. Work is also presented on the first example of channel waveguides in QD-glass fabricated by ULI [2]. The high non-saturable losses meant that this device was not suitable for mode-locking experiments. However, as the waveguide writing conditions are further explored it may be possible to create low-loss waveguides in such a material.

The work in this chapter was the result of a large collaboration, and thus it is important that the work done by others is duly acknowledged here. The QD-SESAM

design and growth was performed by collaborators at *Innolume*[1], the laser cavity was designed and built by my colleague here in St Andrews, Dr Alexander Lagatsky, and the reflectivity parameters of the QD-SESAM were experimentally measured and fitted to models by myself. The QD-glass was fabricated by A. A. Lipovskii[2] and was provided through a collaboration with Belarus National Technical University[3]; ULI was carried out at Heriot Watt University under the direction of Dr Robert Thomson[4]; and waveguide characterisation was performed by myself.

3.2 Quantum Confinement

The density of states of a material describes the number of states it is possible to occupy at a given energy level. For a bulk piece of semiconductor material, provided the incident energy is greater than the bandgap energy, electrons can be excited to some upper state, and the density of states available is greater for higher energies, as shown by the black plot in fig. 3.1. If the size of the semiconductor is reduced in one dimension to a size which is comparable to the electron's de Broglie wavelength then the density of states becomes quantised [3]. In a QW the confinement is in one dimension resulting in a step-like function for the density of states as illustrated in blue in fig. 3.1. In a QD the electron becomes confined in three dimensions allowing only discrete energies to be absorbed. This results in very sharp delta-like functions for the density of states of a QD as illustrated by the red plot in fig. 3.1. The quantum confinement experienced by an electron in a cubic QD can be mathematically described by [4]:

$$E_{n_x,n_y,n_z} = \frac{\hbar^2\pi^2}{2m_e}\left(\frac{n_x^{\,2}}{L_x^{\,2}} + \frac{n_y^{\,2}}{L_y^{\,2}} + \frac{n_z^{\,2}}{L_z^{\,2}}\right) \qquad \text{Eq. 3.1}$$

where E is the energy, h is Planck's constant, m_e is the effective mass of the electron, n is the quantum number, L is the length of the dot and x, y, z represent the direction.

[1] D.A. Livshits, Innolume GmbH, Konrad-Adenauer-Allee 11, 44263 Dortmund, Germany
[2] St Petersburg State Polytechnical University, 195251 St Petersburg, Russia
[3] A. M. Malyarevich, K. V. Yumashev, Research Institute for Optical Materials and Technologies, Belarus National Technical University, 17 Nezavisimosti Ave. 65, 220053 Minsk, Belarus
[4] R. R. Thomson, N. D. Psaila, A. K. Kar, School of Engineering and Physical Sciences, David Brewster Building, Heriot Watt Univeristy, Edinburgh EH14 4AS

This is clearly similar to the discrete allowed energy levels in an atom, and consequently QDs are sometime described as “artificial atoms”. Evidently, by varying the size of the QD, the energy levels are shifted and so the absorption of QDs can be tuned by varying dot size. QDs are typically grown by self-organised growth [5], and this results in dots with a variation of sizes. Consequently there is inhomogeneous broadening of the absorption energies, and broad absorption bandwidths can be achieved, illustrated in green in fig. 3.1.

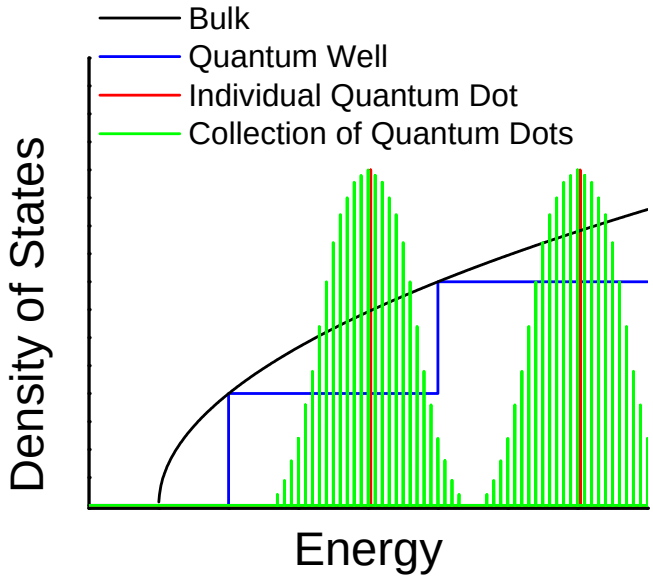

Fig. 3.1. Density of states for bulk (black), quantum well (blue) and quantum dot (red and green) semiconductor devices, illustrating the quantised nature which arises as a result of the quantum confinement.

3.3 Quantum Dots versus Quantum Wells

Quantum dots and quantum wells are both used as saturable absorbers for mode locking lasers. These can be used in transmission or, when combined with a high reflector, in reflection as a SESAM or SBR (saturable Bragg reflector). The key properties of a saturable absorber – absorption, bandwidth, recovery time, modulation depth, saturation fluence and non-saturable loss – were briefly defined in Chapter 1. Quantum wells have typically been used as saturable absorbers, but quantum dots have recently been introduced as a competitor with some key advantages.

The modulation depth in a saturable absorber is due to the filling of the conduction band with excited electrons from the valance band. This reduces the absorption of the device and thus increases the reflectivity. The modulation depth can therefore be tailored by varying the amount of absorber present, through using thicker layers, more layers separated by spacer layers, or alternatively by varying the position of the saturable absorber within the device. Usually the modulation depth is controlled by choosing a suitable number of absorbing layers, as variation of the layer thickness or layer position also affects the saturation fluence and recovery time. For mode locking, modulation depths of < 2 % are typically used [6]. Values greater than this can lead to *Q*-switching instabilities [7]. However, where *Q*-switching is desirable much larger values can be used, with modulation depths up to 30 % not unusual for a *Q*-switched device. Variation in the number and distribution of both QWs and QDs when used as saturable absorbers allows the modulation depths to be tailored to the appropriate application.

The advantages of QDs over QWs become apparent when considering the absorption bandwidth, recovery time and saturation fluence of the device. As explained in section 3.2 an individual QD has a sharp “atom-like” absorption peak, which acts as an excellent saturable absorber at that particular wavelength. The fact that there is a variation in QD sizes during growth therefore results in broadband absorption and so QD saturable absorbers can still be suitable for generating ultrashort pulses. A further advantage is that the recovery time of QDs is made up of two temporal response functions: a fast decay with a large decay constant, plus a slower and weaker relaxation [8]. The slow decay helps stabilise mode locking whilst the fast decay is advantageous in generating the shortest pulses. Similarly short recovery times in QWs can only be achieved by post-processing techniques such as ion implantation which increase the non-saturable losses. Incorporation of a p-n junction in a QD-SESAM has allowed external control of the device and has led to stabilisation of mode locking [9], whilst the application of a reverse bias across the device has produced shorter pulses, suggesting this could introduce a reduction in the device’s recombination time [10]. Perhaps the greatest advantage of QDs over QWs is the reduced saturation fluence, which is a result of the strong and sharp absorption provided by the high density of states of an individual QD, and is also enhanced by the slow component of the device’s recovery dynamics.

Femtosecond operation has been previously demonstrated using QDs as saturable absorbers at 1.3 μm [11, 12], and in the work presented here fs pulses were generated at 1040 nm [1] using a QD-SESAM.

3.4 Yb:KYW Mode Locked with a QD-SESAM

3.4.1 Description of the QD-SESAM

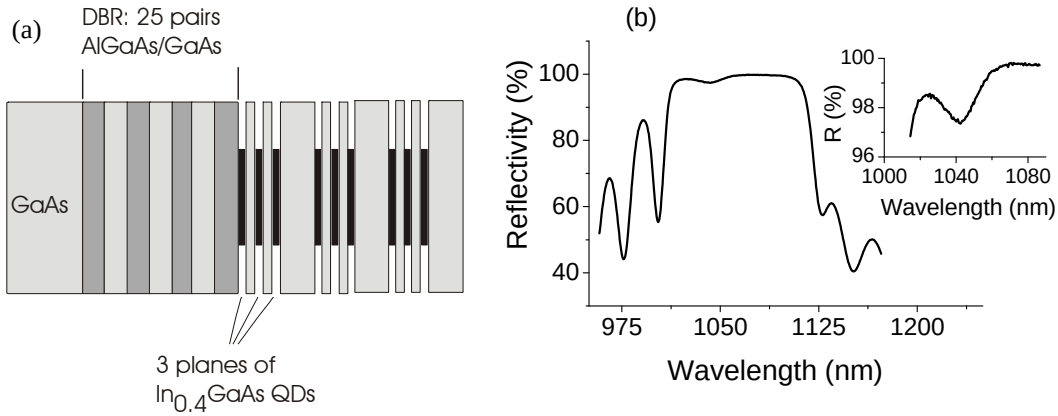

Fig. 3.2. (a) Diagram of QD-SESAM, QD-5-233 as was used in mode-locking experiments, (b) Measured low intensity reflectivity of QD-SESAM, QD-5-233.

The QD-SESAM (QD-5-233) which was used for mode-locked experiments was grown by molecular beam epitaxy (MBE) at ~600 °C. It consisted of three QD regions and a distributed Bragg reflector (DBR). The DBR was formed from 25 pairs of $\lambda/4$ GaAs and $Al_{0.9}Ga_{0.1}As$ layers, providing high reflectivity over the range 1010 nm – 1100 nm. The three QD regions were separated by ~$\lambda/4$ GaAs layers, where λ is the wavelength in the layer, and each QD region consisted of three further QD layers separated by 20 nm thick GaAs spacers, creating an anti-resonant device. A simple schematic of the QD-SESAM is shown in fig. 3.2 (a). The QDs themselves were formed by depositing 9 periods of 0.075 nm InAs and 0.1 nm GaAs and the subsequent self-organized growth resulted in prismatic QDs of ~7 nm lateral size with a dot density of $5x10^{10}$ cm^{-2}. The low reflectivity was measured with a Perkin Elmer Lambda 6000 spectrophotometer and the obtained data is presented in fig. 3.2 (b). It shows that the SESAM provided a peak absorption centred at around 1040 nm, with

an estimated modulation depth when fully saturated of ~2.4 % and a maximum total absorption of 2.5 %.

3.4.2 Laser Cavity and Mode-locked Performance

A highly asymmetric z-fold cavity was built with a cavity design as illustrated in fig. 3.3. The gain medium was a 10 at. % doped 1.2 mm long Brewster cut Yb^{3+}:KYW crystal. The cavity consisted of two curved mirrors with radii of curvature of 100 mm (M1) and 75 mm (M2), the QD-SESAM described above and an output coupler (OC) with a transmission of 3 %. The spot size on the SESAM was 200 μm. Second order dispersion was compensated for with an SF10 prism pair, where the prisms were separated by 50 cm. The pump source was a near-diffraction limited 3.5 W tapered laser diode operating at 980 nm.

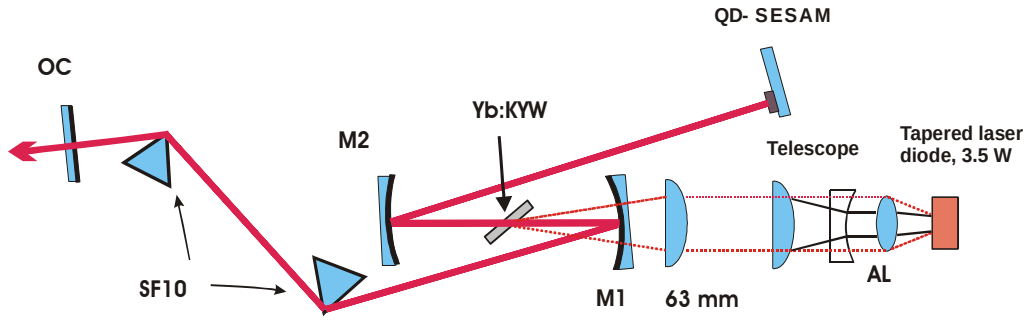

Fig. 3.3. Cavity arrangement for Yb:KYW laser when mode locked

Excellent mode-locked results were achieved from this laser [1], with 200 fs pulses at 107 MHz with 1.15 W of average output power. When operating in CW the output power was 1.8 W, showing a modest reduction upon insertion of the SESAM. By slight adjustment of the cavity even shorter pulses of 114 fs were obtained for 0.5 W average output power. The laser was stably mode locked when intracavity fluences were greater than 100 μJcm^{-2}.

3.5 SESAM Characterisation

3.5.1 Modelling of Fluence-Dependent SESAM Reflectivity.

In order to effectively use and optimise SESAMs it is important to be able to characterise them accurately. The fluence-dependent non-linear reflectivity of a SESAM at a particular operating wavelength can be characterised by three of the important SESAM parameters: the linear reflectivity at zero pulse energy, R_{lin}; the non-saturable losses, δ_{ns}; and the saturation fluence, F_{sat}. These parameters cannot be directly obtained, but must rather be extrapolated from a plot of the non-linear reflectivity. Correct extrapolation of these values requires precise measurement of the reflectivity curve and accurate modelling. A method and model for such characterisation of SESAMs was developed by Haiml [13], and this is implemented here for characterisation of two novel QD-SESAMs.

The band structure of a SESAM is approximated by a two-level system where intraband relaxation, trapping and recombination are assumed to be negligible. The model also assumes that the pulse is shorter than the recovery time of the device, whilst the device's recovery time is less than the time between two consecutive pulses. The behaviour of a two level system is described by [14], with the result:

$$\frac{d\alpha(z,t)}{dt} = -\alpha(z,t)\frac{2\sigma}{\hbar\omega}I(z,t) \qquad \text{Eq. 3.2}$$

where t is time, σ is the absorption and emission cross sections (these are equal for a two level system), z is position in the direction of the beam propagation, h is Planck's constant, ω is frequency of the incident light, I is intensity and α is the absorption co-efficient.

A microscopic definition of F_{sat} is given by [13]:

$$\frac{d\alpha(z,t)}{dt} = -\frac{\alpha(z,t)I(z,t)}{F_{sat}} \qquad \text{Eq. 3.3}$$

and thus:

$$F_{sat} = \frac{\hbar\omega}{2\sigma} \qquad \text{Eq. 3.4}$$

The rate of change of intensity through a saturable absorber is given by:

$$\frac{dI(z,t)}{dt} = -\alpha(z,t)I(z,t) \qquad \text{Eq. 3.5}$$

Solving Eq. 3.3 and Eq. 3.5 allows the pulse energy transmitted through a saturable absorber of length L to be calculated [15]. In a SESAM, as there is a high reflector contained within the device, the reflected pulse energy for an absorber of length $L/2$ is equivalent to the energy transmitted through a normal absorber of length L. Thus the reflectivity is given by [13]:

$$R(F_p) = \frac{\ln\left[1 + R_{lin}\left(\exp S - 1\right)\right]}{S} \qquad \text{Eq. 3.6}$$

where R_{lin} is the reflectivity for zero incident pulse energy and S is the saturation parameter, given by:

$$S = \frac{F_p}{F_{sat}} \qquad \text{Eq. 3.7}$$

Eq. 3.6 assumes that for infinitely high fluences the reflectivity reaches 100 %, but for a real device there will always be some residual losses, δ_{ns}. Eq. 3.6 can be modified to account for this by using a scaling factor, R_{ns}, where $R_{ns} = 1 - \delta_{ns}$.

$$R(F_p) = R_{ns}\frac{\ln\left[1 + \frac{R_{lin}}{R_{ns}}\left(\exp S - 1\right)\right]}{S} \qquad \text{Eq. 3.8}$$

This was confirmed to be valid providing non-saturable losses were < 10 % [13], which is the case for SESAMs described herein. For higher losses the general form of Eq. 3.8 still applies, but there is a small increase in the apparent value of F_{sat}. Further deviations are also observed for very high fluences where non-linear processes such as two photon absorption begin to occur leading to a roll-over in the reflectivity curve. This can again easily be accounted for with a scaling factor, but was not necessary for the SESAMs considered in this work where no roll-over was observed.

Eq. 3.8 gives the reflectivity for a flat top spot which has constant fluence, F_p, given by:

$$F_p = \frac{E_p}{\pi w^2} \qquad \text{Eq. 3.9}$$

In a laser the spot has a Gaussian shape, and therefore the reflectivity needs to be calculated for fluence with a Gaussian profile, $F_{p,Gauss}(r)$,

$$F_{p,Gauss}(r) = F_0 \exp\left(\frac{-2r^2}{w^2}\right) \qquad \text{Eq. 3.10}$$

where F_0 is the peak fluence and w is the beam radius at $1/e^2$. The pulse energy, E_p, is given by:

$$E_p = \int_0^\infty 2\pi r F_{p,Gauss}(r) dr = \tfrac{1}{2} F_0 \pi w^2 \qquad \text{Eq. 3.11}$$

and the reflectivity of the SESAM as a function of r is therefore given by:

$$R(r) = R_{ns} \frac{\ln\left[1 + \frac{R_{lin}}{R_{ns}}\left(\exp\left[\frac{F_{p,Gauss}(r)}{F_{sat}}\right] - 1\right)\right]}{\left[\frac{F_{p,Gauss}(r)}{F_{sat}}\right]} \qquad \text{Eq. 3.12}$$

The total reflectivity of the SESAM for a Gaussian pulse requires integrating the reflectivity at a point, *r*, over the spatial energy distribution of the pulse.

$$R_{Gauss}(F_p) = \frac{1}{E_p}\int_0^{\infty} 2\pi r F_{p,Gauss}(r) R\left(F_{p,Gauss}(r)\right) dr \qquad \text{Eq. 3.13}$$

Using *Mathcad*, Eq. 3.13 was fitted to experimental data obtained for two QD-SESAMs so that the properties of the devices could be characterised. The fitted functions gave sensible values for the parameters, δ_{ns}, ΔR and F_{sat}. The fit deviation was small over a large fluence range indicating a good agreement between the experimental data and the fitted model. The method used to experimentally determine the SESAM's reflectivity is now described.

3.5.2 Experimental Set-up for Measuring Non-linear Reflectivity

In order to determine the performance of a SESAM in a particular cavity a second laser with similar wavelength and pulse duration is required. Thus a second cavity was constructed with similar performance to that described in 3.4.1. This had a similar cavity to that shown in fig. 3.3, but M1 and M2 had radii of curvature of 100 mm and 150 mm respectively and the QD-SESAM was replaced with a more typical QW-SESAM. The spot size incident on the SESAM was 150 μm. This laser produced a pulse centred at 1040.3 nm with a FWHM of 6.5 nm. The pulse duration from the laser was 198 fs and the repetition rate was 91.4 MHz. The spectrum and autocorrelation for this pulse are shown in fig. 3.4.

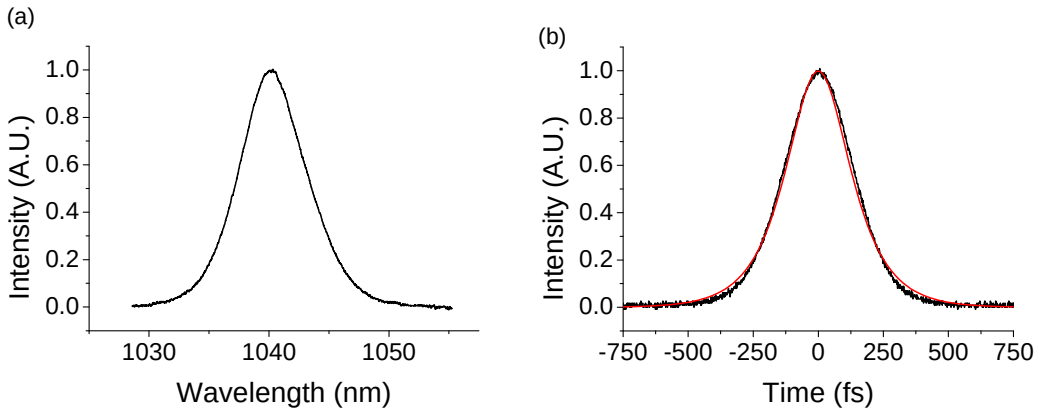

Fig. 3.4. (a) Spectrum and (b) autocorrelation of pulse used for SESAM characterisation.

This laser was then used as the source for measuring the non-linear reflectivity in a simple set-up as illustrated in fig. 3.5. A half-waveplate was used together with a polarising beamsplitter to vary the incident pulse fluence, F_p, so that the reflectivity could be measured over a large fluence range. A 25 mm lens was used to focus the laser onto the SESAM, creating a spot radius on the SESAM of 13.5 μm at $1/e^2$. This was measured with a beam profiler, and the beam was confirmed to have a Gaussian shape, as required for the model developed in section 3.5.1. The QD-SESAM was placed at the focus and was angled to reflect the light along a deviated path, which was rotated from the incident beam by 33°. Ideally the measurements would have been taken under normal incidence, so as to minimise the reflectivity shift of the SESAM, and while this angle was as small as was practically possible with the available mounts it nevertheless represents rather a large departure from this scenario. However, given the close agreement of the low intensity reflectivity measurement with that from the spectrophotometer this shift was not believed to significantly alter the result. Furthermore, spectrophotometer measurements suggest the absorption does not significantly change up to angles of ~60º. A power meter was used to measure the incident and reflected power.

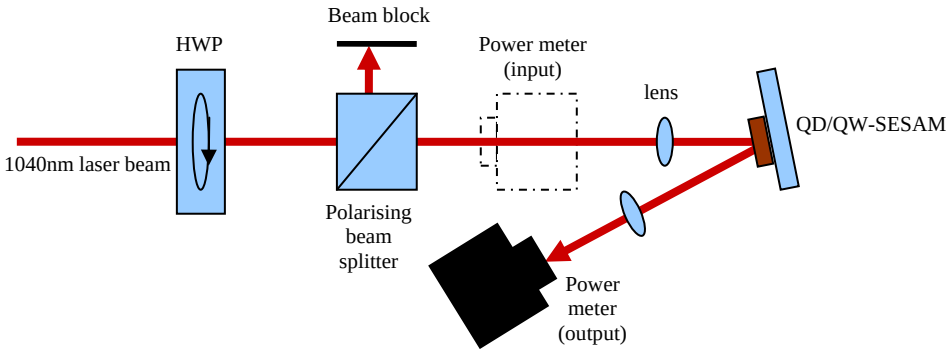

Fig. 3.5. Set-up used to characterise QD-SESAM. HWP = half-waveplate.

The total incident pulse fluence was simply calculated:

$$F_p = \frac{P_i}{f_{rep}.\pi.w^2} \qquad \text{Eq. 3.14}$$

and the reflectivity was determined from the ratio of reflected power to incident power, taking into account the losses introduced by the lenses.

3.5.3 Characterisation of QD-SESAM, s-571-80QD

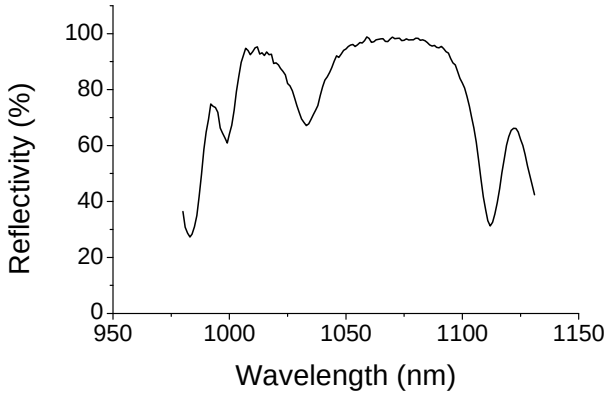

Fig. 3.6. Low intensity reflectivity of QD-SESAM, s571-80-QDs

Before characterising the QD-SESAM (s-QD5-233) used for the mode-locked laser described in section 3.4.1 a second QD-SESAM (s-571-80QD) was characterised. This SESAM had 80 QD layers and thus a larger modulation depth which was easier to characterise. This was used as a sanity check that the experiment was performed correctly and that the fitted function gave accurate results. The reflectivity of the SESAM at a very low intensity was measured using a spectrophotometer, and this is shown in fig. 3.6. The linear reflectivity at 1040 nm is therefore estimated to be around 80 %, with a modulation depth of ~15 %.

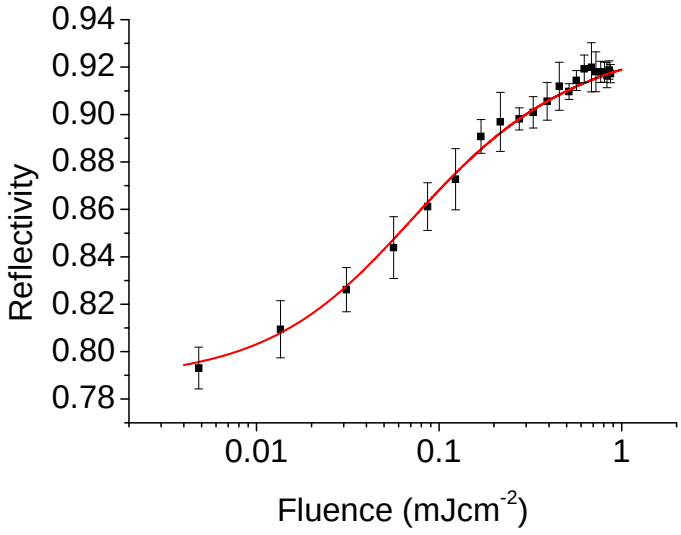

Fig. 3.7. Reflectivity as a function of fluence for QD-SESAM, s571-80-QDs with experimental data points for the SESAM shown in black, and a fitted curve plotted in red defined by the parameters: 78.8 % linear reflectivity; 6.8 % non-saturable losses; 37 μJcm^{-2} saturation fluence.

The experimental data for the reflectivity as a function of fluence, together with the modelled function are shown in fig. 3.7. The best fit was obtained when the SESAM key parameters in the model were set to be R_{lin} = 78.8 % R_{ns} = 93.2 %, ΔR = 14.4 % (modulation depth) and F_{sat} = 37 μJcm^{-2}, showing close agreement with those assumed from the low intensity measurement, and confirming the validity of the model.

3.5.4 Characterisation of QD-SESAM, QD-5-233

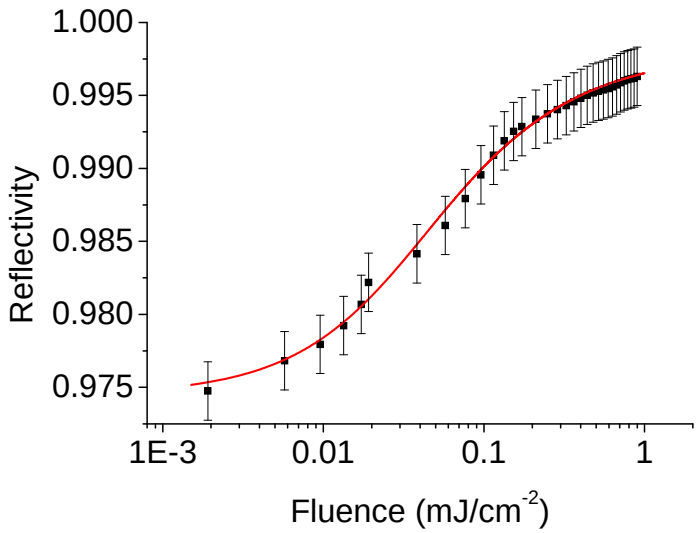

Fig. 3.8. Reflectivity as a function of fluence with data points for the QD-SESAM, QD-5-233, and a fitted curve shown by the red plot defined by: 97.45 % linear reflectivity; 0.2 % non-saturable losses; 25 μJcm^{-2} saturation fluence.

QD-5-233, the QD-SESAM described in 3.4.1, was then characterised using the same method. This was expected to be more difficult to measure, as the smaller modulation depth increases the significance of the measurement error. However, by taking several readings and averaging it was still possible to obtain a curve which could be used for characterisation. The experimental data and the model function are shown in fig. 3.8 and give the key parameters of the SESAM as R_{lin} = 97.45 %, R_{ns} = 99.8 %, ΔR = 2.35 % and F_{sat} = 25 μJcm^{-2}. This compares very well with the expected modulation depth of 2.4 %, and linear reflectivity of 97.4 % which can be estimated from the low fluence graph shown in fig. 3.2 (b).

The deviation of the experimental data points from the fit was found to be very small, showing the suitability of this fit [13]. The very low non-saturable losses of 0.2 % are typical losses for a high reflecting Bragg structure, showing the non-saturable losses of the QD layers to be negligible.

3.6 Channel Waveguides in a Quantum Dot Doped Glass

Saturable absorbers can be used in either transmission or reflection, where the difference is only that of design. Here, ULI was used to inscribe a channel waveguide in a QD saturable absorber for use in transmission. Such a device has advantages which include the potential for integration with a channel waveguide gain material, and also a reduced average pulse saturation fluence as a result of the maintenance of high intensities over the entire sample length. This could enable mode locking to be more easily obtained.

3.6.1 Quantum Dot Sample

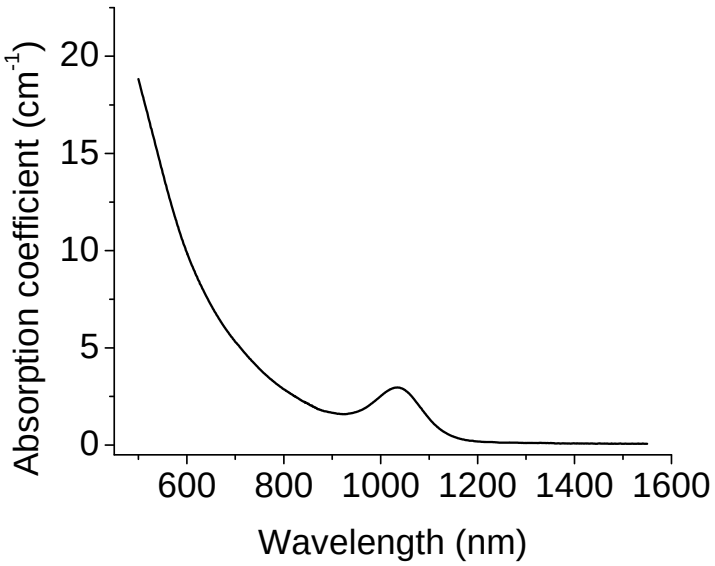

Fig. 3.9. Absorption coefficient of 3.2 nm PbS quantum dots in a silicate glass matrix.

A 0.85 cm long silicate glass matrix containing PbS quantum dots was used as a sample for waveguide writing experiments [2]. The dot size was 3.2 nm providing a first excitonic absorption peak at around 1 μm. The absorption of the bulk sample was

measured with a Perkin Elmer spectrophotometer and is shown in fig. 3.9. It has strong absorption, of 2.87 cm^{-1} at the 800 nm writing wavelength. This is unusual for ultrafast laser inscription, as typically the writing wavelength is chosen to have negligible linear absorption.

3.6.2 Waveguide Writing Conditions

Waveguides were written at Heriot Watt University using a 5 kHz Ti:sapphire laser with 130 fs circularly polarised pulses in the set-up described in section 2.2. Forty-nine waveguides were written 200 μm below the glass surface. These were written with thirteen different pulse energies ranging from 12.6 μJ to 85.6 μJ at four different writing speeds: 0.1 mms^{-1}, 0.2 mms^{-1}, 0.4 mms^{-1} and 0.8 mms^{-1}. The final set at 85.6 μJ was incomplete due to restrictions on the sample size.

3.6.3 Waveguide Loss Measurements

Waveguide losses were estimated using the simple transmission technique as described in section 2.3. A 980 nm InGaAs fibre coupled laser diode was used as the source for the measurements. The bulk glass sample has an absorption co-efficient of 2.11 cm^{-1} at this wavelength, corresponding to 7.8 dB of loss over the crystal length after subtracting Fresnel losses. Guiding was observed in all samples written at pulse energies greater than 24 μJ, irrespective of writing speed, with the exception of six structures which were not able to guide (written at 45.6 μJ and 53.6 μJ). The poor performance of these structures was due to the poor quality of the glass in the concerned vicinity, rather than as a result of the writing conditions.

The best waveguide was found to be formed with 74 μJ pulse energy at the lowest writing velocity, 0.1 mms^{-1}. The best coupling was obtained when using a 16× objective to collimate the laser source followed by a 25 mm lens to focus the light into the waveguide. This gave a e^{-2} spot size radius of 7 μm. The guided mode had a radius of 11 μm, which was Gaussian and symmetric as illustrated in fig. 3.10. Assuming negligible coupling loss and subtracting Fresnel losses, the waveguide loss at 980 nm was determined to be 8 dB over the sample length. The next challenge was to separate

the absorption from the propagation loss. This was to enable estimation of the propagation loss for the waveguide, but also to determine whether or not the quantum dots were preserved during the writing process.

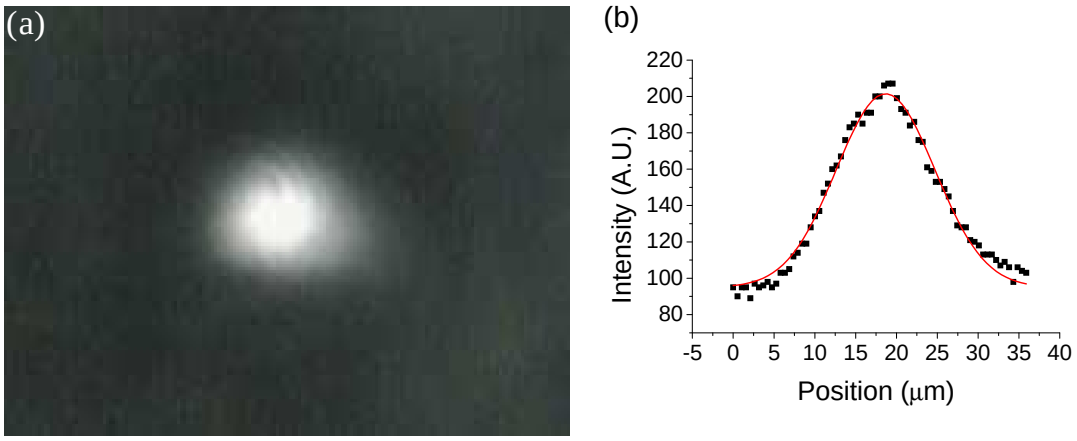

Fig. 3.10. (a) Image of guided mode. (b) Horizontal profile of guided mode, showing a waist (e^{-2} radius) of 11 μm.

Losses were therefore measured at 1550 nm, away from the absorption peak of the quantum dots, to establish an estimate for the waveguide propagation loss. A source of amplified spontaneous emission (ASE) was used for this measurement, using the same transmission method previously described. At this wavelength the absorption over the 0.85 cm length of glass is only 0.26 dB. A 30× objective was used to collimate the source and a 10× objective was used to focus into the waveguide, giving a spot radius of 12 μm. Assuming 100 % coupling efficiency, the waveguide propagation losses were 2.5 dB over the sample length (0.68 cm^{-1} or 2.9 $dBcm^{-1}$). Using this as an estimate for the propagation losses at 980 nm, the absorption losses can be estimated at 5.5 dB, or 1.5 cm^{-1}. This shows that there has been some modification to the quantum dots as a result of the direct writing, reducing the absorption characteristics of the device, and thus also the modulation depth. Further experiments are necessary to determine whether the relaxation rate is also modified. Regardless of the outcome, this is still an important first step towards the creation of a waveguide saturable absorber which could be used for creating fully integrated and pulsed waveguide lasers.

3.7 Conclusions and Future Outlook

In conclusion, a set-up and model for accurately characterising the key parameters of a SESAM's non-linear reflectivity has been described. This allowed the characterisation of a novel QD-SESAM which was used to generate fs pulses from an Yb:KYW laser. The QD-SESAM was found to have a non-saturable loss of only 0.2 % and a saturation fluence of only 25 μJcm^{-2}, which is significantly lower than the 100 μJcm^{-2} saturation fluence of anti-resonant QW-SESAMs [1]. In the future such a device could be integrated in a waveguide Yb:tungstate laser to create a compact and efficient ultrafast laser source. Currently, QD-SESAMs are only available as high reflectors, and are therefore not ideal for use in monolithic cavities. However, recently, output-coupling QW-SESAMs have been demonstrated [16, 17], and are now even commercially available (as described in section 4.6). Thus it is anticipated that output-coupling QD-SESAMs may also soon be available, characterised by fast relaxation times, low non-saturable losses and low saturation fluences, and therefore suitable for ultrafast pulse generation through integration with waveguide lasers. The first examples of QD-glass channel waveguides formed by ULI were also described. The propagation losses were estimated to be rather high at 2.9 $dBcm^{-1}$, and the absorption coefficient was reduced with respect to the bulk, suggesting some modification to the QDs within the inscribed region. However, this was an important first step towards fabrication of channel waveguides in saturable absorbers for future integration with waveguide lasers.

3.8 References

[1] A. A. Lagatsky, F. M. Bain, C. T. A. Brown, W. Sibbett, D. A. Livshits, G. Erbert and E. U. Rafailov, "Low-loss quantum-dot-based saturable absorber for efficient femtosecond pulse generation," Applied Physics Letters **91,** 231111 (2007).

[2] A. M. Malyarevich, K. V. Yumashev, A. A. Lagatsky, F. M. Bain, C. T. A. Brown, W. Sibbett, R. R. Thomson, A. K. Kar, A. A. Onushchenko, A. A. Zhilin and A. A. Lipovskii, "Optical Waveguides in Glasses Doped with Lead Sulfide Quantum Dots," Physics, Chemistry and Application of Nanostructures**,** 140-143 (2009).

[3] R. Dingle, A. C. Gossard and W. Wiegmann, "Direct Observation of Superlattice Formation in a Semiconductor Heterostructure," Physical Review Letters **34,** 1327-1330 (1975).

[4] D. A. Neaman, "Semiconductor Physics and Devices: Basic Principles", McGraw-Hill, 3rd edition, 2003, Chapter 2, p.24-55

[5] N. N. Ledentsov, V. M. Ustinov, A. Y. Egorov, A. E. Zhokov, M. V. Maximov, I. G. Tabatadze and P. S. Kop'ev, "Optical properties of heterostructures with InGaAs-GaAs quantum clusters," Semiconductors **28,** 832-834 (1994).

[6] G. J. Spühler, R. Paschotta, R. Fluck, B. Braun, M. Moser, G. Zhang, E. Gini and U. Keller, "Experimentally confirmed design guidelines for passively Q-switched microchip lasers using semiconductor saturable absorbers," Journal of the Optical Society of America B-Optical Physics **16,** 376-388 (1999).

[7] C. Hönninger, R. Paschotta, F. Morier-Genoud, M. Moser and U. Keller, "Q-switching stability limits of continuous-wave passive mode locking," Journal of the Optical Society of America B-Optical Physics **16,** 46-56 (1999).

[8] E. U. Rafailov, S. J. White, A. A. Lagatsky, A. Miller, W. Sibbett, D. A. Livshits, A. E. Zhukov and V. M. Ustinov, "Fast quantum-dot saturable absorber for passive mode-locking of solid-state lasers," IEEE Photonics Technology Letters **16,** 2439-2441 (2004).

[9] A. A. Lagatsky, E. U. Rafailov, W. Sibbett, D. A. Livshits, A. E. Zhukov and V. M. Ustinov, "Quantum-dot-based saturable absorber with p-n junction for

mode-locking of solid-state lasers," IEEE Photonics Technology Letters **17,** 294-296 (2005).

[10] D. B. Malins, A. Gomez-Iglesias, S. J. White, W. Sibbett, A. Miller and E. U. Rafailov, "Ultrafast electroabsorption dynamics in an InAs quantum dot saturable absorber at 1.3 μm," Applied Physics Letters **89,** 171111 (2006).

[11] A. McWilliam, A. A. Lagatsky, C. T. A. Brown, W. Sibbett, A. E. Zhukov, V. M. Ustinov, A. P. Vasil'ev and E. U. Rafailov, "Quantum-dot-based saturable absorber for femtosecond mode-locked operation of a solid-state laser," Optics Letters **31,** 1444-1446 (2006).

[12] M. P. Lumb, E. Clarke, E. Harbord, P. Spencer, R. Murray, F. Masia, P. Borri, W. Langbein, C. G. Leburn, C. Jappy, N. K. Metzger, C. T. A. Brown and W. Sibbett, "Ultrafast absorption recovery dynamics of 1300 nm quantum dot saturable absorber mirrors," Applied Physics Letters **95,** 041101 (2009).

[13] M. Haiml, R. Grange and U. Keller, "Optical characterization of semiconductor saturable absorbers," Applied Physics B-Lasers and Optics **79,** 331-339 (2004).

[14] A. E. Siegman, "Lasers", University Science Books, 1986, p.203-210&292-294

[15] A. E. Siegman, "Lasers", University Science Books, 1986, p.297-299&1104-1107

[16] R. C. Sharp, D. E. Spock, N. Pan and J. Elliot, "190-fs passively mode-locked thulium fiber laser with a low threshold," Optics Letters **21,** 881-883 (1996).

[17] G. J. Spühler, S. Reffert, M. Haiml, M. Moser and U. Keller, "Output-coupling semiconductor saturable absorber mirror," Applied Physics Letters **78,** 2733-2735 (2001).

Chapter 4
Yb:KYW LPE-grown Planar Waveguide Laser

4.1 Introduction

Several methods are available for the creation of crystalline waveguides (see section 1.7). One of the best developed methods is that of Liquid Phase Epitaxy (LPE). This technique has been used here, in a collaboration between ourselves and two Institutes in Minsk[1,2], to create an Yb:KYW planar waveguide for use as a laser gain medium. Initially, a 100 μm layer of Yb:KYW was grown on a crystal of undoped KYW. The crystal was used in a bulk cavity configuration, so that the quality of the layer and its suitability as a laser gain material could be assessed. Based on the feedback of this characterisation, a 14 μm layer of Yb:KYW was grown on an undoped KYW crystal, creating an Yb:KYW planar waveguide. This waveguide was used as the gain material in the first demonstration of a compact, monolithic cavity, LPE-grown Yb:KYW planar waveguide laser, and lasing with high efficiencies and low thresholds were achieved [1]. Using an output coupling SESAM, *Q*-switching was also observed from the LPE-grown planar waveguide. This was the first example of *Q*-switching from such a device.

4.2 Growth of Yb:KYW on KYW by LPE

A brief description of LPE was provided in section 1.7, but the particular application of this technique to Yb-doped tungstates is outlined here. The similarity of the ionic radii of Yb and Y (see section 1.3.1) means that Yb:KYW and KYW have similar lattices which make them very compatible and suitable for growth by LPE. Indeed, it is possible to grow crack-free layers with Yb doping concentrations as high as 15 % [2]. Since KYbW and KYW are isostructural the refractive index of Yb:KYW

[1] S. V. Kurilchick, V. E. Kisel and N.V. Kuleshov, Institute for Optical Materials and Technologies, Belarusian National Technical University, 65 Nezavistimosti Avenue, 220013 Minsk, Belarus
[2] S. A. Guretsky, A. M. Luginets, N. A. Kalanda, I. M. Kolesova, The Scientific and Practical Materials Research Center, NASB, 17 P. Brovkistr., 220072 Minsk, Belarus

increases linearly with doping concentration [3]. However, this linear increase is fairly small and therefore the disadvantage of working with these materials is the similarity of their refractive indices. Waveguides grown with these materials have a limited numerical aperture, even with 15 % doping. This low numerical aperture can be overcome by co-doping the layer with other rare-earth/trivalent ions in order to increase the refractive index contrast. However, since the lattice structure of Yb:KYW is already similar to the seed lattice, one needs to ensure that the addition of further ions to the layer does not also reduce the quality of the layer due to a higher lattice mismatch. By careful tailoring of the different co-dopants it is possible to grow layers which simultaneously have high numerical apertures and a low lattice mismatch. This has successfully been employed to create high quality layers with a large numerical aperture [4, 5].

The single-crystalline layers of Yb:KYW grown for lasing experiments were grown on the (010) plane of α-KYW crystals of 3 mm and 4 mm length. Crystal forming oxide concentrations of less than 24 mol. % were used, and the supercooling temperatures were in the range of 0.8 K to 1.5 K. Growth was performed at a rate of 0.6 µm/min to 1.2 µm/min. In the 3 mm crystal the Yb doping level was 10 at. % and in the 4 mm crystal it was 3 at. %. Initially, a 100 µm layer was grown on the 3 mm long crystal. This was Brewster cut, and the facets of the waveguides were polished for lasing experiments. The laser performance of the layer was characterised, providing feedback on the layer quality to our collaborators in Minsk. A 14 µm layer was then grown on the 4 mm long plane-plane cut crystal, and the facets were polished flat for laser experiments. This planar waveguide was used in a laser cavity to construct the first monolithic LPE grown Yb:KYW laser [1]. Based on the 3 % doping level, the refractive index contrast was estimated to be $\sim 1\times10^{-3}$ [3], which is able to support two transverse modes along the $\mathbf{N_p}$ axis at 1000 nm. Future work on creating integrated devices may, however, involve co-doping and/or overgrowing the doped layer with an undoped layer to provide tighter and more symmetric confinement. This would allow higher efficiencies and full integration of the laser with other optical components.

4.3 Lasing from 100 µm Yb:KYW Layer

The pump source for this laser was a linearly polarised fibre-coupled InGaAs laser diode with diffraction limited output operating at 981 nm with a maximum output power approaching 500 mW, as described in section 2.3.1. A ×30 microscope objective collimated the pump light, and a 63 mm lens was used to end-pump the Yb(10 at. %):KYW layer, providing a pump spot size of 29 µm (e^{-2} diameter). Before constructing a laser cavity around the crystal, the pump transmission through the crystal as a function of incident pump power was measured. This allowed the absorbed pump power to be inferred for calculations of slope efficiencies and laser performance. The transmission as a function of incident pump power is shown in fig. 4.1. The behaviour shown is typical, as the absorption becomes saturated at high pumping due to the depopulation of the ground state. This leads to the transmission increasing as the pump power increases until a point of rollover.

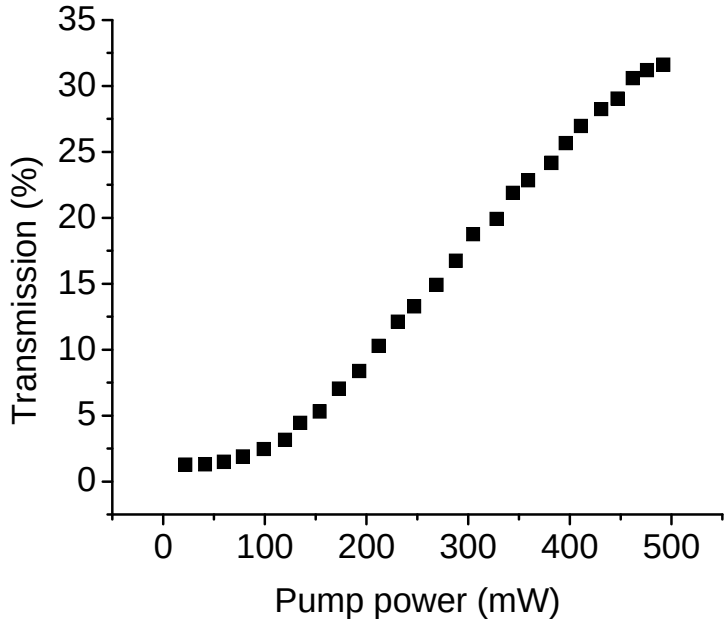

Fig. 4.1. Percentage of transmitted pump as a function of incident pump power. This shows absorption saturation at high pump powers as the ground level becomes depopulated.

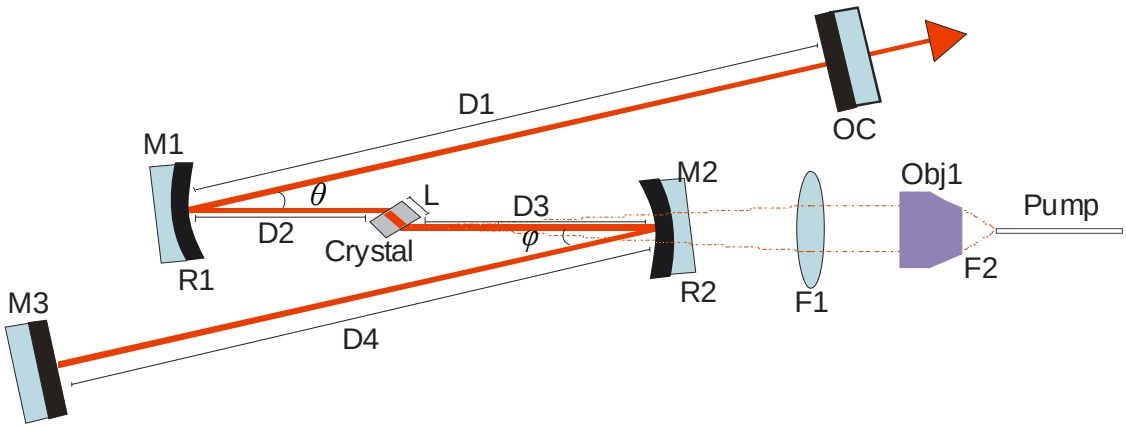

Fig. 4.2. Assymmtric 4-mirror laser cavity design for the 100 µm thick LPE layer planar waveguide gain material. An InGaAs laser diode is used as the pump source. All other elements are as listed in the following table (4.1).

Cavity property	Symbol	Value
Distance from output coupler (OC) to first curved mirror (M1)	D1	490 mm
Radius of curvature of M1	R1	50 mm
M1 fold angle	θ	16°
Distance from M1 to crystal	D2	25.1 mm
Crystal length	L	3 mm
Distance from crystal to second curved mirror (M2)	D3	37.26 mm
Radius of curvature of M2	R2	75 mm
M2 fold angle	φ	16°
Distance from M2 to end mirror (M3)	D4	420 mm
Focal length of lens (F1)	F1	63 mm
Focal length of objective (Obj1)	F2	6.2 mm

Table 4.1. Parameters used in the 4-mirror asymmetric cavity design, relating to the figure illustrated in fig. 4.2.

A schematic of the standard four mirror asymmetric cavity design is shown in fig. 4.2 and the associated parameters are outlined in table 4.1. A variety of output couplers were used to assess the performance of the layer. The exact output coupling of each

output coupler, at the laser operation wavelength, was later determined using a Perkin Elmer Lambda 950 spectrophotometer and the values are shown in fig. 4.3. The Brewster angle for the crystal was 63.4° and the cavity waist in the crystal had an e^{-2} diameter of 30 µm. The laser cavity was built as close to this geometry as possible, with fine adjustment of crystal and mirror positions until lowest lasing threshold and highest output power was achieved. The lasing results for are shown in fig. 4.3 and summarised in table 4.2.

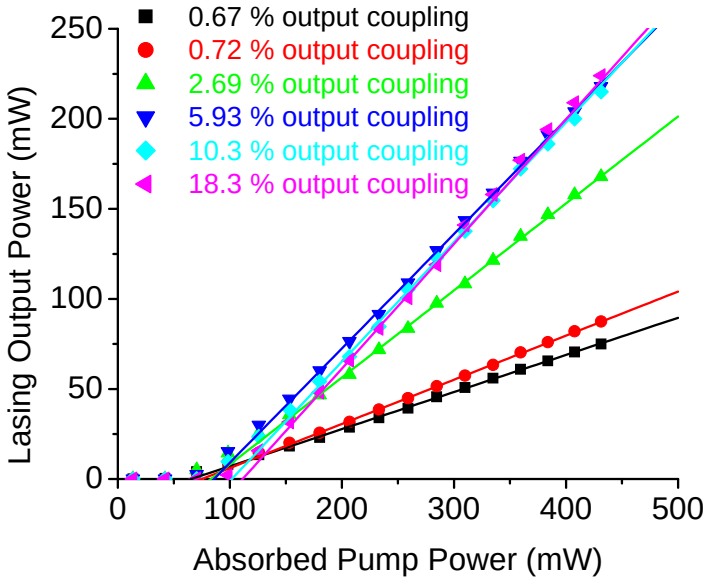

Fig. 4.3. Yb:KYW LPE-thin film laser performance for a variety of output couplers.

Measured output coupling (%)	0.67	0.73	2.7	5.9	10.3	18.3
Lasing wavelength (nm)	1039.6	1038.6	1035.9	1030.9	1029.6	1028.7
Slope efficiency (%)	20.6	24.5	48.3	63.5	66.4	69.2

Table 4.2. Summary of Yb:KYW thin-film laser results.

It is clear from these results that the lasing wavelength decreases as higher value output couplers are used. This behaviour is typical of quasi-three-level lasers, and can be attributed to the pump-dependence of the gain profiles at threshold [6-9].

The maximum output power achieved was 224 mW, for only 431 mW absorbed pump power, and the corresponding slope efficiency was 69.2 %. There was no sign of rollover of the laser output, implying significantly higher output powers could be achieved with higher pumping. The lowest threshold was 53 mW absorbed pump power and this was obtained with 0.67 % output coupling.

Using these results it was simple to calculate the losses in the waveguide by means of the Caird plot (see section 2.3.6), which plots:

$$\frac{1}{\eta} = \frac{1}{\eta_0} + \frac{\delta}{\eta_0}\frac{1}{T_{OC}} \qquad \text{Eq. 4.1}$$

The relevant plot is shown in fig. 4.4, where errors are estimated based on the deviation of points from the fitted straight line.

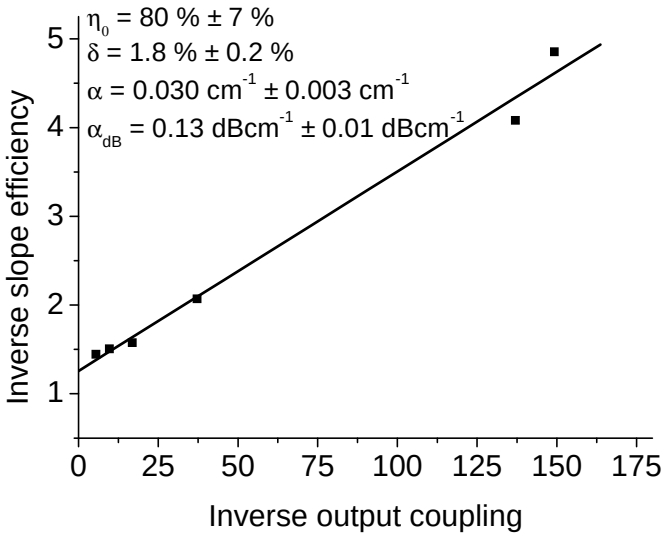

Fig. 4.4. A Caird plot for the 100 µm LPE-grown Yb:KYW laser, allowing the intrinsic slope efficiency and losses to be calculated.

The losses of 0.03 cm^{-1}, or 0.13 $dBcm^{-1}$, are very low and comparable to those of bulk Yb:KYW crystals, showing the suitability of LPE for growing single crystalline layers. These losses are likely to be due to small amounts of scattering due to defects or absorption from impurities. Feedback was given to collaborators in Minsk to enable them to improve the growth of their thin films. The laser performance of this

crystalline layer is comparable to the performance of bulk devices [10] and shows the potential for creating a waveguide laser using this technique.

4.4 Lasing from 14 µm Yb:KYW Planar Waveguide

For the planar waveguide experiments the 3 % doped, 4 mm long plane-plane crystal was used, with a 14 µm single-crystalline layer of Yb:KYW grown on top of undoped KYW. The same InGaAs single-mode laser diode as used in previous experiments (section 2.3) was used as a pump source, although the pumping geometry was different. A ×30 microscope objective collimated the pump light, which was then polarised horizontally, corresponding to the crystallo-optic $\mathbf{N_m}$ axis. This is close to the crystallographic ***a*** axis, to make use of the strong pump absorption for this axis in Yb:KYW (see section 1.3.4). The polarised beam was passed through a Faraday Isolator to prevent back reflections from the plane-cut crystal damaging the laser diode. The Faraday Isolator reduced the incident pump by around 15 %. A range of microscope objectives and lenses with focal lengths ranging from 8 mm – 25 mm were investigated for coupling into the planar waveguide. The best performance was achieved when using a ×10 objective, which had a 15.4 mm focal length and provided a pump spot beam diameter of 18 µm.

When constructing the waveguide laser cavity a different resonator design was used. One of the main advantages of a waveguide geometry is the possibility to construct a compact monolithic laser system. Thus, rather than use a bulky four mirror cavity, a simple plane-plane cavity was constructed. Very thin coated fused silica substrates were used as mirrors. The input mirror was coated for high transmission at 980 nm and high reflection at 1010 nm – 1100 nm mirrors. Although the mirrors were designed for an air-mirror interface, the mirrors performed equally well when in contact with the waveguide facet using index matching fluid (n = 1.303). Similarly thin output couplers with transmissions of 1 %, 3 % and 5 % in the region 1010 nm – 1100 nm were grown on fused silica substrates, and the output couplers were also either held near the output facet on a mount, or placed in contact with the waveguide facet using fluorinert, creating a simple monolithic plane-plane cavity. A × 10 objective was used to collimate the output from the cavity, and the laser output was

separated from any residual pump using a dichroic beamsplitter. This set-up is illustrated in fig. 4.5.

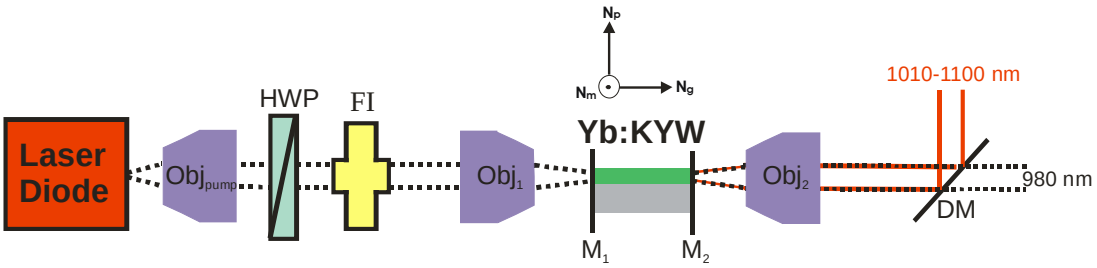

Fig. 4.5. Monolithic laser cavity design. Pumping is from an InGaAs laser diode at 980 nm, with an M^2 of 1. Obj$_{pump}$ = ×30 microscope objective; Obj$_1$ and Obj$_2$ = ×10 microscope objective; HWP = half-waveplate; FI = Faraday Isolator; M$_1$ = incoupling mirror, HT at 980 nm and HR 1010-1100 nm; waveguide is 3 at. % doped Yb:KYW on bulk KYW crystal; M$_2$ = output coupler; DM = dichroic mirror, HT at 980 nm, HR 1010-1100 nm at 45°. Crystallograpic axes are as labelled.

No active cooling of the sample was used. By cooling the sample it is envisioned that lower thresholds could be achieved, as there would be lower population of the lower laser level leading to reduced re-absorption losses. However, cooling would complicate the system, and this cavity design shows the ability of this material to lase in an extremely simple cavity configuration.

An upper limit on the absorbed pump power was calculated by comparing the throughput power when launched into the doped region to that of the bulk undoped region in a similar way to that described by Pelenc et al. [11], as described in section 2.3.4. The slope efficiencies quoted are therefore a lower limit, and the performance could in fact be slightly better than that quoted. From the graph in fig. 4.6, which shows the transmitted pump power as a function of incident pump power, it may seem as though the absorbed pump power should decrease with increasing pump power. However, it has been shown this is not the case, and once laser threshold is reached the absorbed pump power remains approximately constant [12]. This is because the stimulated emission frees upper energy levels, preventing the absorption from experiencing further saturation.

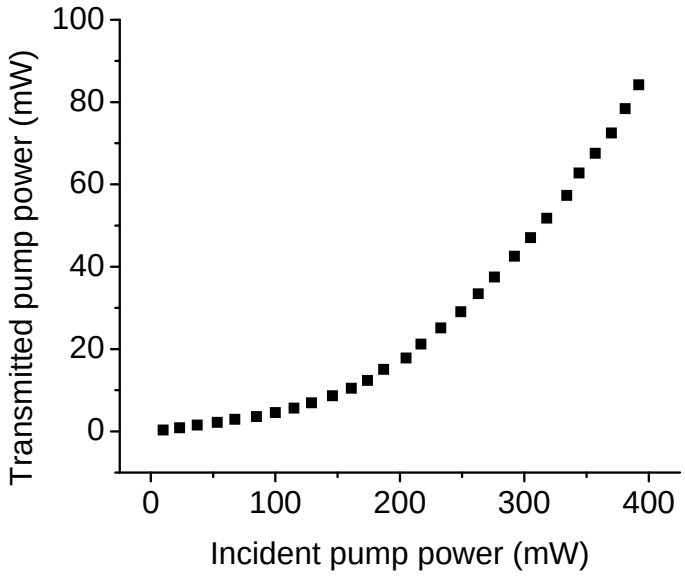

Fig. 4.6. Transmitted pump power as a function of incident pump power for Yb:KYW planar waveguide

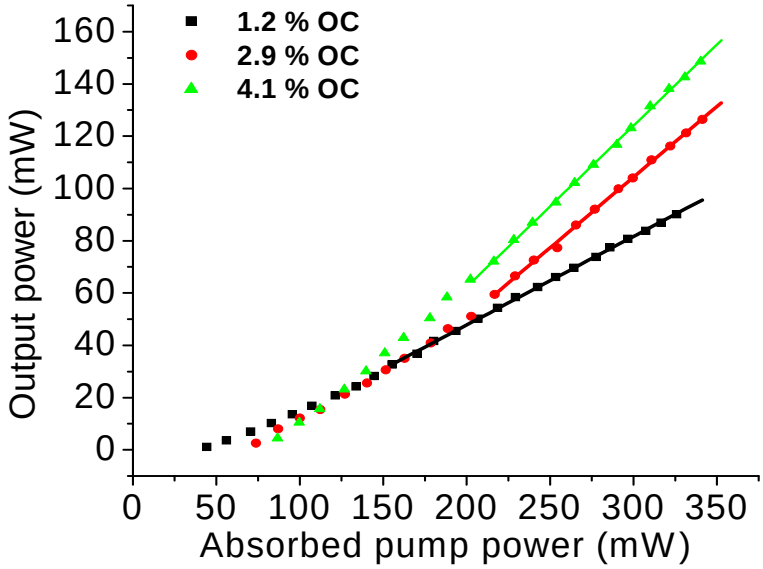

Fig. 4.7. Output power as a function of absorbed pump power for three different output couplers.

The observed results of threshold, maximum output power, wavelength and slope efficiency are shown in fig. 4.7 and summarised in table 4.3. As is clear from the table, the Yb:KYW planar waveguide laser constructed with the 1.2 % output coupler gave a low lasing threshold of only 40 mW, which is the lowest reported for an Yb:KYW laser, showing the advantage that waveguide confinement can offer even

when only in one dimension as in the planar waveguide case. The maximum output power of 148 mW for 340 mW absorbed pump and the 62 % slope efficiency measured with the 4.1 % output-coupled monolithic planar waveguide laser is comparable to the 160 mW and 63.8 % slope efficiency realised with 6 % output coupling in the four-mirror cavity described in section 4.3. The longer lasing wavelengths are a result of reduced intracavity losses, which are most likely a result of reduced re-absorption loss in the 3 % doped crystal compared to the 10 % doping used previously.

Measured output coupling	1.2 %	2.9 %	4.1 %
Threshold of absorbed pump power (mW)	40	70	80
Maximum output power (mW)	90	126	148
Slope efficiency (%)	34	54	62
Wavelength (nm)	1044	1041	1039

Table 4.3. Summary of Yb:KYW planar waveguide laser results.

To enable fuller analysis of this waveguide's lasing performance further output couplers were also used. These were not thin fused silica substrates, as used before, but were standard laser quality mirrors from *LaserOptic GmbH*, with measured transmissions of 1.7 %, 10.3 % or 18.4 % at the lasing wavelength. The performance was also quickly checked with standard 1 % and 4 % output couplers to ensure similar results were obtained with the two different mirror sets, and this was found to be the case. These output couplers were too heavy to be held on by surface tension, and so mounts were used to hold them against the crystal facet instead. However, all other aspects of the cavity design remained the same. The best performance was observed with the 10.3 % output coupler, where an output power as high as 190 mW was observed for 340 mW absorbed pump power, with a 76 % slope efficiency. Using the 18.4 % output coupler at the lasing wavelength, the power dropped significantly, and so this output coupling was evidently too high to efficiently generate power from this laser. The results for all the output couplers used with the 14 µm LPE waveguide laser are presented in fig. 4.8 and summarised in table 4.4.

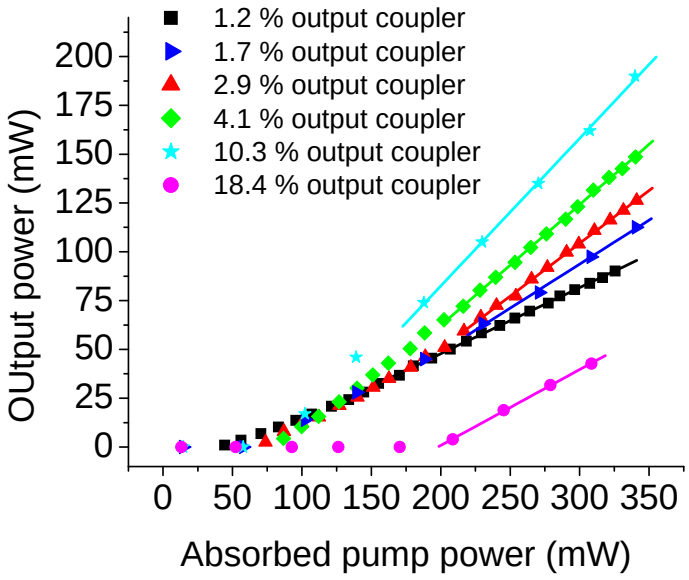

Fig. 4.8. Output power as a function of absorbed pump power for 1.2 %, 1.7 %, 2.9 %, 4.1 %, 10.3 % and 18.4 % output couplers in a planar waveguide, LPE-grown, monolithic cavity.

Measured output coupling	1.2 %	1.7 %	2.9 %	4.1 %	10.3 %	18.4 %
Absorbed pump power threshold (mW)	40	70	70	80	75	240
Maximum output power (mW)	90	112	126	148	190	43
Slope efficiency (%)	34	45	51	62	76	39
Wavelength (nm)	1044	1039	1041	1039	1038	1035

Table 4.4. Summary of 14 µm planar waveguide Yb:KYW lasing results for various output couplers.

A Caird plot (see section 2.3.6) was plotted with these results to determine the losses and intrinsic slope efficiency of this material. This plot is shown in fig. 4.9. An excellent intrinsic slope efficiency of ~90 % was obtained, close to the quantum defect of ~95 %. The losses are also extremely low at around 0.1 $dBcm^{-1}$, showing the excellent quality of waveguides grown by this technique, where the losses are essentially the same as those in bulk Yb:KYW [10].

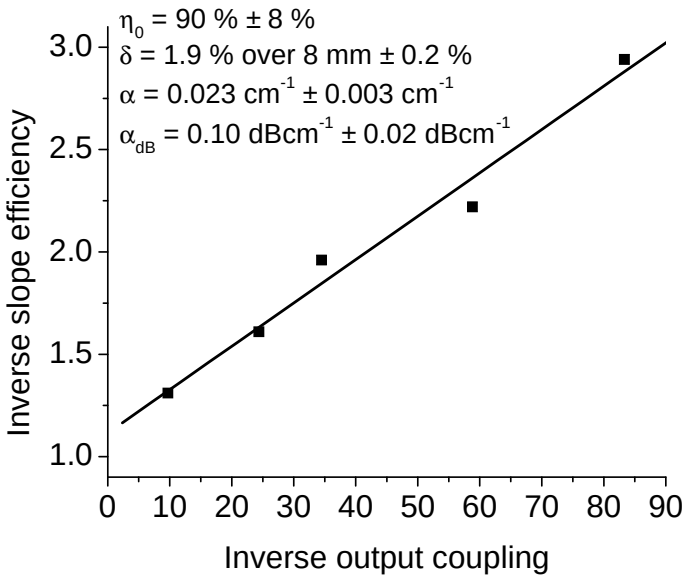

Fig. 4.9. A Caird plot for the 14 µm LPE-grown Yb:KYW laser, allowing the intrinsic slope efficiency and losses to be calculated.

To determine the size of the cavity mode two identical 50 mm lenses were used to form an image of the end facet. The residual pump was found to be negligible, but to ensure it was only the laser profile rather than the pump profile which was being viewed, a high reflecting mirror at 980 nm, which had around 40 % transmission at the lasing wavelength was used to block all pump light. The laser profile was then observed with a beam profiler, and the imaged waist, corresponding to the profile at the output facet, was found to be elliptical with e^{-2} diameters of 14 µm and 80 µm along the $\mathbf{N_p}$ and $\mathbf{N_m}$ axes respectively. The M^2 for the $\mathbf{N_p}$ axis was measured to be around 1.2, while the beam quality along the $\mathbf{N_m}$ axis was greater than 10. This poor performance of the $\mathbf{N_m}$ axis is typical of planar waveguides.

4.5 *Q*-switching from 14 µm Yb:KYW Planar Waveguide

Once the CW performance of the LPE-grown crystalline Yb:KYW layer had been assessed, attention was turned to the generation of pulses. Two output coupling SESAMs (OC-SESAMs) were purchased from *Batop*: SOC-1040-1.0-0 and SOC-1040-3-0, which have the characteristics shown in table 4.5. The reflectivity curves for the SESAMs were drawn using the *Mathcad* model described in Chapter 3,

and are shown in fig. 4.10. In order to produce pulses from the cavity, the output coupler from the CW cavity was simply replaced with an OC-SESAM.

SESAM property at 1040nm	SOC-1040-1.0-0	SOC-1040-3-0
Modulation depth (ΔR)	0.6 %	1.8 %
Non-saturable loss (δ_{ns})	0.4 %	1.2 %
Transmission (T_{OC})	1.5 %	0.4 %
Saturation fluences (F_{sat})	90 μJcm^{-2}	90 μJcm^{-2}
Relaxation time (τ_{relax})	< 10 ps	< 10 ps

Table 4.5. Properties of output coupling SESAMs used for *Q*-switching experiments.

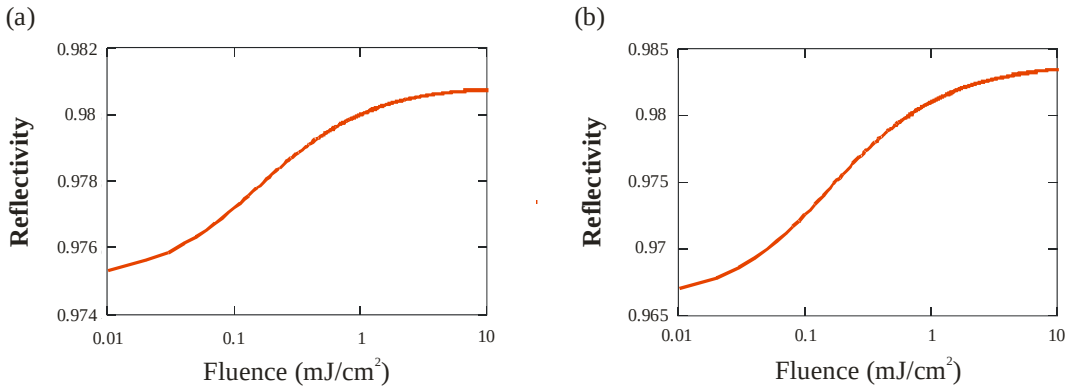

Fig. 4.10. Non-linear reflectivity curves for (a) SOC-1040-1.0-0 and (b) SOC-1040-3-0

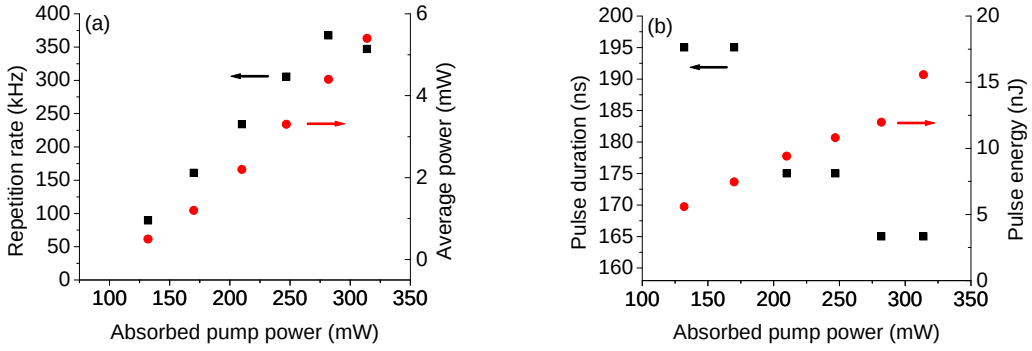

Fig. 4.11. Results for the *Q*-switched laser using the SOC-1040-3-0 output-coupling SESAM showing (a) repetition rate and average output power and (b) pulse duration and pulse energy as a function of absorbed pump power.

The SOC-1040-3-0 *Q*-switched laser produced a maximum output power of 5.5 mW, at a repetition rate of 370 kHz. The repetition rate increased with increasing pump power, as expected for a *Q*-switched laser [13]. The pulse duration decreased with increasing pump power to a value of around 165 ns, which was measured with a fast detector and a 2 GHz oscilloscope. These results are shown in fig. 4.11.

The highest output power was achieved when using SOC-1040-1.0-0. In this case stable *Q*-switching was achieved with an average output power as high as 33 mW and a threshold of under 100 mW absorbed pump power. The pulse repetition frequency increased with pump power up to a maximum of 722 kHz. The pulse duration decreased with increasing pump power to a minimum duration of 170 ns.

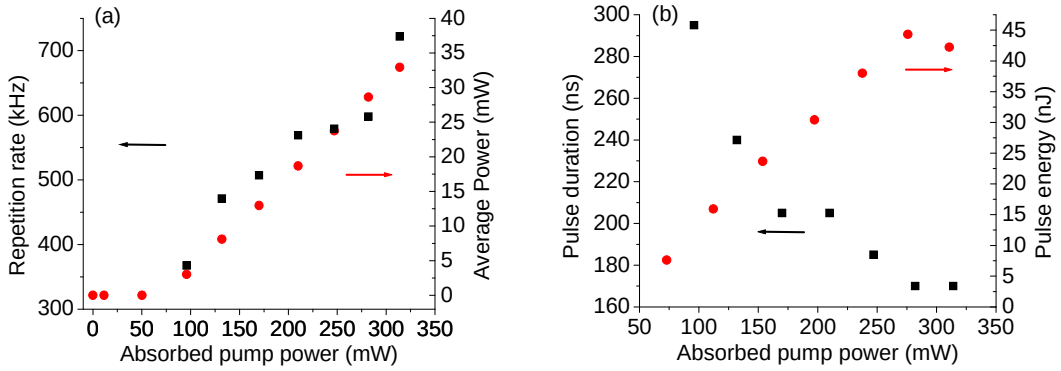

Fig. 4.12. Results for the *Q*-switched laser using SOC-1040-1.0-0 SESAM showing (a) repetition rate and average output power and (b) pulse duration and pulse energy as a function of absorbed pump power.

The maximum pulse energy was calculated to be 44 nJ, and the peak power from the *Q*-switched laser was therefore 250 mW. The central laser wavelength from the *Q*-switched LPE planar waveguide laser was 1040 nm, with a spectral bandwidth of 0.1 nm. The results obtained with this SESAM are shown in fig. 4.12.

The pulse duration of a *Q*-switched laser can be calculated from Eq. 4.2 [14, 15].

$$\tau = \frac{3.52\tau_{RT}}{\Delta R} \qquad \text{Eq. 4.2}$$

The cavity round-trip time, τ_{RT}, is 53 ps, and so when using SOC-1040-1.0-0 for *Q*-switching, with a modulation depth of 0.6 %, it may seem as though the pulse duration of the laser should be only ~30 ns, much shorter than that observed. However, the low pulse energy, together with a long pulse duration and mode area of ~900 μm^2, means that the device is not completely saturated and the full modulation depth is not utilised, resulting in longer pulses.

As a consequence of the low intensity incident on the OC-SESAM it was not possible to obtain mode locking. However, in a channel waveguide with similar performance the pulse fluence would be much higher, and could be enough to generate some ultrashort pulses. Therefore, by realising efficient channel waveguides, a mode-locked channel waveguide laser can be attained. The OC-SESAMs used here were designed with small modulation depths so that they would be suitable for ultrashort pulse generation. However, to optimise the *Q*-switched performance from this cavity a different SESAM design could be used which is more suitable to the production of stable *Q*-switching, such as larger modulation depth [15].

4.6 Partially Unstable 14 μm Yb:KYW Planar Waveguide Laser

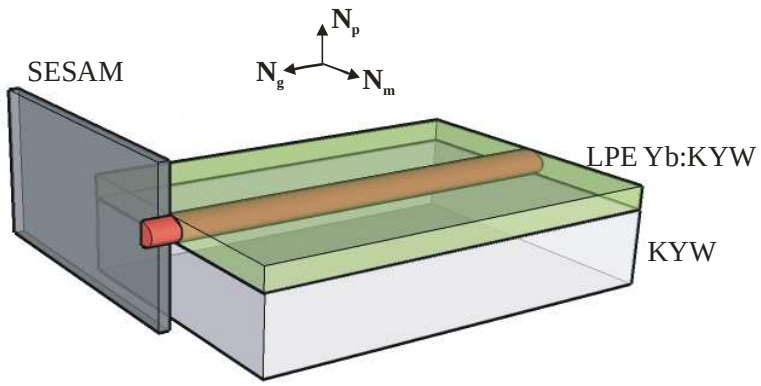

Fig. 4.13. Illustration of configuration used to create a partially unstable cavity.

Unstable cavity arrangements have previously been identified as being good options for extracting the maximum output power from a laser, while simultaneously optimising its beam quality [16]. By partially covering the guiding area with a high

reflector mirror or an output-coupling SESAM along the $\mathbf{N_m}$ axis direction, a partially geometrically unstable resonator was formed (fig. 4.13).

When using a small piece of high reflector to form the unstable cavity a maximum output power of 93 mW, and a slope efficiency of 45 % were obtained, with a threshold of around 100 mW. The laser operated around 1037 nm. The output power as a function of absorbed pump power is shown in fig. 4.14.

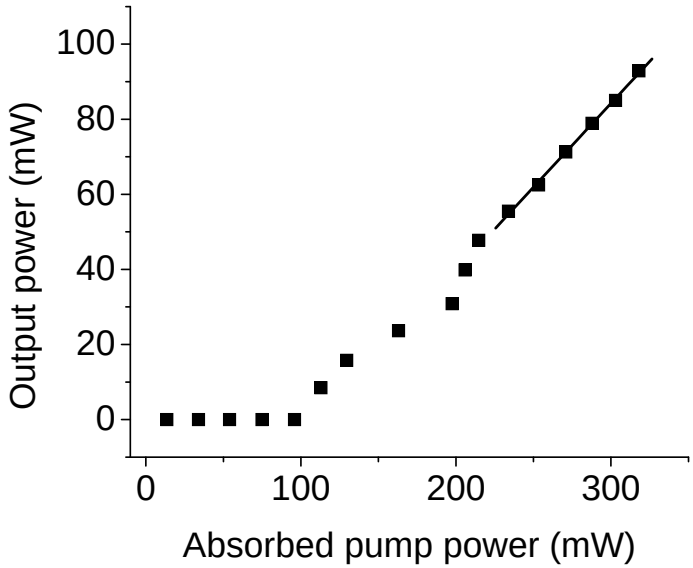

Fig. 4.14. Output power for a partially unstable cavity, formed using a high reflecting mirror that is only partially covering the waveguide gain material.

The slope efficiency of an unstable resonator depends on the output coupling in the same manner as a stable resonator [17]. Thus the slope efficiency of 45 % implies an output coupling close to 2 %, as can be noted from table 4.4. The higher absorbed pump power threshold and lower lasing wavelength compared to the results in table 4.4 imply increased losses, presumably as a result of scattering from the rough edge on the high reflecting mirror.

An interesting property of unstable cavities is that the output coupling depends on the magnification of the cavity, rather than the Fresnel number of the resonator, and thus has little dependence on the position of the mirror used to form the unstable cavity [18]. This was indeed found to be the case, as can be seen in fig. 4.15, where the

maximum power remains fairly constant over more than a millimetre of mirror translation along the $\mathbf{N_m}$ axis. The approximate position of the mirror edge compared to the centre of the pump beam was estimated by imaging the end facet, but the relative translation of the mirror is accurately known.

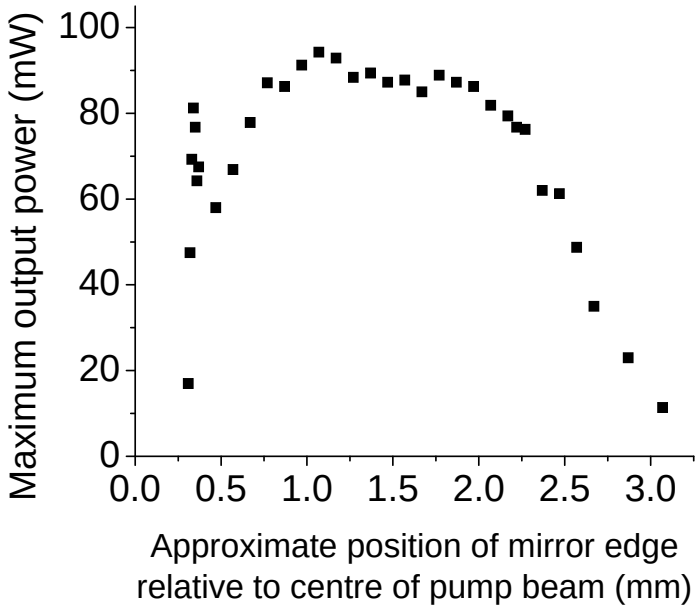

Fig. 4.15. Maximum output power from the unstable cavity as the high reflecting mirror is translated along the unstable axis.

The beam profile was clearly seen to be poor both in the near- and far-field. Even though it is possible to obtain excellent beam profiles from unstable laser cavities, this requires care in the design of the cavity. A large magnification is required in the resonator in order to have good mode discrimination leading to a good far-field beam pattern [19]. For an unstable resonator with low magnification there is a broad distribution of side lobes with only a fraction of the energy contained within the central lobe [20]. This can clearly be seen in models of the far-field beam pattern of unstable resonators with various Fresnel numbers and values of magnification, shown for example in Siegman's *Lasers* [21]. There, it is shown that the Fresnel number has little impact on the far-field beam profile, whilst the magnification significantly changes the number and distribution of side lobes. For the examples shown in [21] a magnification of 10 produces a central lobe containing more than 70 % of the total power but a magnification of 1.42 gives a beam with many side lobes and only ~15 %

of the total power is contained in the central lobe. The cavity constructed here had an output coupling of ~2 %, which corresponds to a magnification of only ~1.02. This value can be expected given that a plane-plane cavity was constructed, producing minimal magnification. The low value of magnification explains the poor quality of the far-field beam pattern. Methods for improving this will be discussed in the conclusions.

Very similar performances – in terms of average output power, slope efficiency and threshold – were obtained when using the SESAM rather than the high reflecting mirror, but with *Q*-switched rather than CW performance. The repetition rates and pulse durations were similar to those seen in the stable cavity. Using SOC-1040-1.0-0 an average output power of 87 mW was obtained, which was almost a three-fold increase of average power compared to the stable resonator. The slope efficiency was 49 % and the laser operated at 1035 nm.

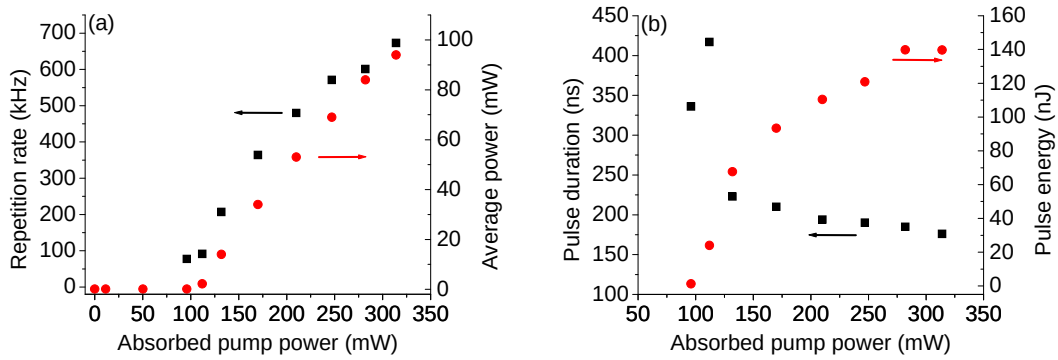

Fig. 4.16. *Q*-switched results from unstable cavity formed using SOC-1040-3-0. Very similar results were obtained with SOC-1040-1.0-0.

A similar average power of 92 mW with a 47 % slope efficiency was found when using SOC-1040-3-0 which is a dramatic increase compared with only 5.5 mW when using the same SESAM in a stable cavity configuration. In this case the lasing wavelength was centred at 1035 nm. The repetition rate at the maximum pump power level was 673 kHz, and the pulse duration was around 175 ns, showing little variation from the results obtained with the stable cavity. The pulse energy was 140 nJ and the peak power reached 794 mW. The results obtained are summarised in fig. 4.16.

4.7 Conclusions and Future Work

In this chapter, the development of planar waveguide lasers based on LPE-grown Yb:KYW have been presented. This has culminated in the demonstration of the first diode-pumped, monolithic, LPE-grown planar waveguide Yb:KYW laser [1]. This operated around 1040 nm with output powers up to 148 mW, and slope efficiencies exceeding 62 %, approaching those of bulk lasers. The propagation losses from this planar waveguide were ~0.1 $dBcm^{-1}$ at 1 μm. Low thresholds ~40 mW were observed, which is the lowest threshold observed in an Yb:KYW laser, emphasising the advantage of a waveguide configuration for quasi-three-level systems. Using a standard 10.3 % output coupler, output powers of 190 mW were observed with an excellent slope efficiency of 76 %. This result should be attainable in the monolithic cavity arrangement with the fabrication of a suitable output coupler.

Stable *Q*-switching was observed by using a saturable absorber in the cavity. A maximum average output power of 33 mW was obtained, with pulse energies of 44 nJ at 722 kHz, and with 170 ns pulse durations.

Finally, the benefits of using a partially unstable cavity could be seen as average output power and maximum pulse energy of the *Q*-switched laser increased dramatically, to 92 mW and 140 nJ respectively. The beam quality was not, however, found to improve, and this was a result of the low cavity magnification. One way to improve the beam quality of the laser would be to use an increased magnification by using a negative branch cavity, but this is not easily achievable in a monolithic device. Another option would be to use a variable reflectivity end mirror which can offer excellent mode discrimination [22], however these mirrors must be specially designed and fabricated and are not readily available. A third option is the creation of channel waveguides, which can easily produce excellent beam profiles in both axes, and if low losses are achieved then channel waveguides have the additional advantages of reduced lasing thresholds.

Mode-locked pulses could potentially be achieved from such a cavity, which would see the advent of a monolithic Yb:KYW femtosecond waveguide laser, and would

thus be an exciting development in the field of ultrafast optics. The limiting factor thus far in the demonstration of such a laser is the failure to saturate the SESAM used in the cavity. However, if the SESAM were to be saturated, which could be achievable with good quality channel waveguides or by using SESAMs with lower saturation fluences, then mode-locked femtosecond pulses would be seen from such a laser for the first time.

4.8 References

[1] F. M. Bain, A. A. Lagatsky, S. V. Kurilchick, V. E. Kisel, S. A. Guretsky, A. M. Luginets, N. A. Kalanda, I. M. Kolesova, N. V. Kuleshov, W. Sibbett and C. T. A. Brown, "Continuous-wave and Q-switched operation of a compact, diode-pumped Yb^{3+}:$KY(WO_4)_2$ planar waveguide laser," Optics Express **17,** 1666-1670 (2009).

[2] A. Aznar, R. Solé, M. Aguiló, F. Díaz, U. Griebner, R. Grunwald and V. Petrov, "Growth, optical characterization, and laser operation of epitaxial Yb:$KY(WO_4)_2$/$KY(WO_4)_2$ composites with monoclinic structure," Applied Physics Letters **85,** 4313-4315 (2004).

[3] Y. E. Romanyuk, C. N. Borca, M. Pollnau, S. Rivier, V. Petrov and U. Griebner, "Yb-doped $KY(WO_4)_2$ planar waveguide laser," Optics Letters **31,** 53-55 (2006).

[4] F. Gardíllou, Y. E. Romanyuk, C. N. Borca, R. P. Salathé and M. Pollnau, "Lu, Gd codoped $KY(WO_4)_2$:Yb epitaxial layers: towards integrated optics based on $KY(WO_4)_2$," Optics Letters **32,** 488-490 (2007).

[5] D. Geskus, S. Aravazhi, E. Bernhardi, C. Grivas, S. Harkema, K. Hametner, D. Günther, K. Wörhoff and M. Pollnau, "Low-threshold, highly efficient Gd^{3+}, Lu^{3+} co-doped $KY(WO_4)_2$:Yb^{3+} planar waveguide lasers," Laser Physics Letters **6,** 800-805 (2009).

[6] C. Li, J. C. Souriau, C. Borel and C. Wyon, "Room-Temperature Cw Laser Action of Y_2SiO_5:Yb^{3+},Er^{3+} at 1.57μm," Optics Communications **107,** 61-64 (1994).

[7] A. A. Lagatsky, N. V. Kuleshov and V. P. Mikhailov, "Diode-pumped CW lasing of Yb:KYW and Yb:KGW," Optics Communications **165,** 71-75 (1999).

[8] W. P. Risk, "Modeling of longitudinally pumped solid-state lasers exhibiting reabsortion losses," Journal of the Optical Society of America B-Optical Physics **5,** 1412 (1988).

[9] Y. Zaouter, J. Didierjean, E. Balembois, G. L. Leclin, F. Druon, P. Georges, J. Petit, P. Goldner and B. Viana, "47-fs diode-pumped Yb^{3+}:$CaGdAlO_4$ laser," Optics Letters **31,** 119-121 (2006).

[10] N. V. Kuleshov, A. A. Lagatsky, V. G. Shcherbitsky, V. P. Mikhailov, E. Heumann, T. Jensen, A. Diening and G. Huber, "CW laser performance of Yb and Er,Yb doped tungstates," Applied Physics B-Lasers and Optics **64,** 409-413 (1997).

[11] D. Pelenc, B. Chambaz, I. Chartier, B. Ferrand, C. Wyon, D. P. Shepherd, D. C. Hanna, A. C. Large and A. C. Tropper, "High Slope Efficiency and Low-Threshold in a Diode-Pumped Epitaxially Grown Yb:YAG Wave-Guide Laser," Optics Communications **115,** 491-497 (1995).

[12] R. Scheps, J. F. Myers and S. A. Payne, "End-Pumped Yb-Doped Fluorapatite Laser," IEEE Photonics Technology Letters **5,** 1285-1288 (1993).

[13] J. A. Morris and C. R. Pollock, "Passive Q-Switching of a Diode-Pumped Nd:YAG Laser with a Saturable Absorber," Optics Letters **15,** 440-442 (1990).

[14] A. A. Lagatsky, A. Abdolvand and N. V. Kuleshov, "Passive Q switching and self-frequency Raman conversion in a diode-pumped Yb:$KGd(WO_4)_2$ laser," Optics Letters **25,** 616-618 (2000).

[15] G. J. Spühler, R. Paschotta, R. Fluck, B. Braun, M. Moser, G. Zhang, E. Gini and U. Keller, "Experimentally confirmed design guidelines for passively Q-switched microchip lasers using semiconductor saturable absorbers," Journal of the Optical Society of America B-Optical Physics **16,** 376-388 (1999).

[16] A. E. Siegman, "Unstable Optical Resonators," Applied Optics **13,** 353-367 (1974).

[17] A. E. Siegman, "Lasers", University Science Books, 1986, p.865

[18] A. E. Siegman, "Lasers", University Science Books, 1986, p.860-861

[19] A. E. Siegman, "Lasers", University Science Books, 1986, p.864

[20] A. E. Siegman, "Lasers", University Science Books, 1986, p.860

[21] A. E. Siegman, "Lasers", University Science Books, 1986, p.880-882

[22] A. E. Siegman, "Lasers", Univerisity Science Books, 1986, p.913-921

Chapter 5
Yb:tungstate Channel Waveguide Lasers

5.1 Introduction

The technique of ultrafast laser inscription (ULI) has been introduced as a method for creating crystalline channel waveguides [1, 2] and an overview of this technique was described in Chapter 1. The experimental set-up used to write the structures was described in Chapter 2, and some results of channel waveguides fabricated in a Quantum Dot doped glass were presented in Chapter 3. The technique has previously been employed to create lasing crystalline channel waveguides in LiF at 707 nm [3] and Nd:YAG [4-6] around 1 μm. In 2008 Raman gain was demonstrated in ULI channel waveguides of undoped KGdW [7], and in 2007 channel waveguides were fabricated in Yb:KYW but the resulting waveguides were not able to support lasing [8]. In this chapter the first examples of lasing in channel waveguides of Yb:KGdW and Yb:KYW are presented [9]. The samples were fabricated by Dr Robert Thomson at Heriot Watt University and the sample analysis and laser experiments were performed by myself at the University of St Andrews.

5.2 Sample Description and Writing Conditions

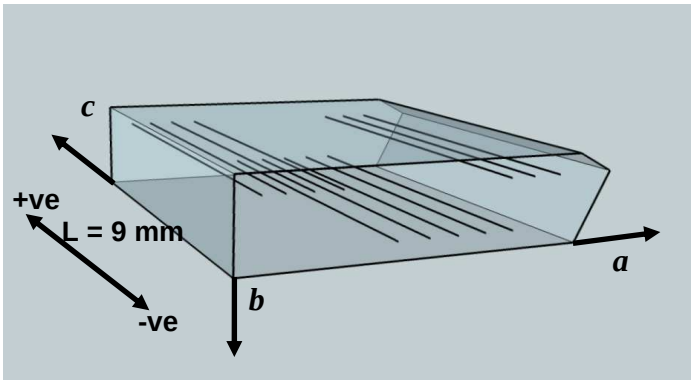

Fig. 5.1. Diagram of Yb:KGdW and Yb:KYW crystal illustrating the crystallographic axes, the positions of the waveguides and the writing directions used.

ULI was used to transversally write waveguides along the ***c*** axis of crystalline Yb(5 at. %):KGdW and Yb(5 at. %):KYW, as shown in fig. 5.1. The samples had dimensions of 2(***b***)×10(***a***)×10(***c***) mm^3 and 1(***b***)×10(***a***)×10(***c***) mm^3 respectively. The inscription set-up was as described in section 2.2 using the Yb:fibre laser as the writing source. When using ULI in crystalline media the written track usually manifests itself as a lower index barrier, and so pairs of modified tracks were inscribed in order to enclose the waveguide in a well-defined region and to create symmetric waveguides. A schematic illustrating the principle of this technique is presented in fig. 5.2. This technique had previously been shown to improve confinement and waveguide performance [8]. Writing was performed to within less than 500 μm of the crystal facets, and the crystals were polished back to reveal the modified region. The final crystal length along the ***c*** axis was 9 mm after polishing.

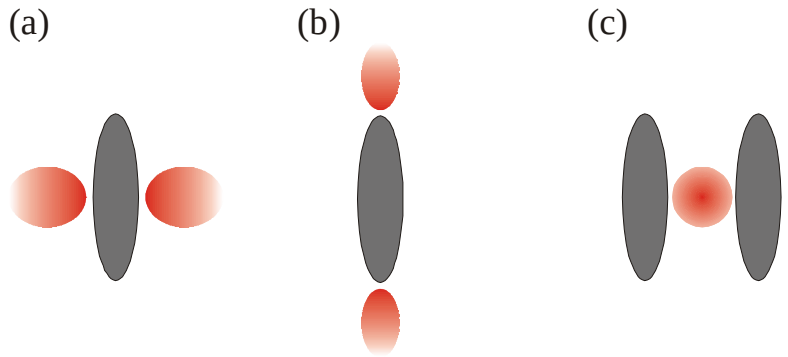

Fig. 5.2. Schematic illustration of typical guiding regions found in ULI crystal waveguides, where written filaments are shown in grey, and guiding regions are shown in red. (a) and (b) show typical guiding areas in a region surrounding the written volume. The exact position of the guiding areas can vary with crystal, writing parameters and guiding polarisation. (c) shows the proposed writing scheme, utilising two parallel tracks to create a symmetric and more confined guiding region. This has previously been demonstrated to improve guiding results [8].

As explained in section 1.7 there are many writing parameters which are known to affect the performance of the waveguides, and thus substantial work is required to optimise the writing conditions. The waveguides reported here were fabricated with a constant writing wavelength of 1064 nm; repetition rate of 500 kHz; 1.3 ps pulse duration; 6 mms^{-1} writing velocity and 20× focusing objective. The varied parameters were the pulse energy, writing polarisation, scan separation, and writing direction. The incident pulse energy was varied from 296 nJ – 558 nJ in Yb:KGdW and 252 nJ –

578 nJ in Yb:KYW in steps of approximately 20 nJ. In the case of Yb:KGdW structures were inscribed 430 μm below the surface using linear polarisation, which was polarised along either the ***a*** or ***c*** axis, with scan separations ranging from 10 μm to 25 μm in 5 μm steps, and also using circular polarisation with scan separations varying from 20 μm to 35 μm. After inscribing the structures in Yb:KGdW it was noted that linear polarisation resulted in catastrophic crystal damage and so in Yb:KYW circular polarisation was used for all structures. Structures were inscribed 360 μm below the crystal's surface.

The effect of writing direction on waveguide performance was also investigated, with pairs of tracks being written by translating the sample in the negative ***c*** axis direction as well as the positive direction for each pulse energy, scan separation and polarisation. At the time the experiments were performed the scan direction had recently been shown to affect the waveguide quality, but the reason for this was not known. This effect has now been attributed to wavefront tilt [10]. Unfortunately, as this was not the known cause at the time, the wavefront tilt during writing was not recorded. Therefore, although a difference in performance is evident between the two writing conditions, a quantitative measure of the cause of this is not. A total of 176 structures were written in the Yb:KYW crystal, and 168 structures in Yb:KGdW. The writing conditions used for each of these structures are presented in a table in Appendix A. In the following sections of this chapter the waveguiding behaviour is presented, together with results from lasing structures and selected non-lasing structures.

5.3 Experimental Procedures

5.3.1 Identifying Crystal Modification and Guiding Regions

The first task was to determine the positions of the structures and the energies needed to modify the crystal. This was simply done by imaging the crystal's end facets with a CCD camera and 50× objective under incoherent white light illumination from a tungsten lightbulb.

Guiding regions were then identified using the 980 nm InGaAs laser diode described in section 2.3. Although this wavelength corresponds to an absorption peak of the crystals, the power available from the diode was sufficient to saturate the crystal absorption and so guiding structures were easily identifiable. For a given crystal and guiding polarisation the guided mode sizes for structures written under different conditions were similar. Therefore, by using this technique, it was also possible to identify the most promising guiding regions by observing the point of absorption saturation. For lower propagation loss the absorption became saturated at lower pump powers. Once saturation was reached the structures with lower propagation losses also gave a higher gradient of transmitted power to incident power. These two characteristics of the curve gave a clear qualitative indication of the waveguide's quality. An example of this behaviour is shown in section 5.4.2.2.

5.3.2 Laser Cavity

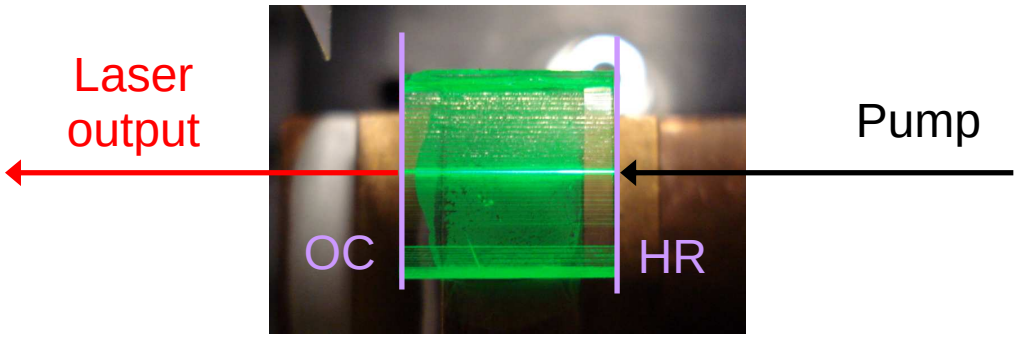

Fig. 5.3. Photograph showing a waveguide in the Yb:KGdW crystal under pumping at 980 nm. The high reflector (HR) and output coupler (OC) have been drawn in to illustrate the laser cavity that was formed.

Attempts were made to obtain lasing in all of the identified waveguides using a compact laser cavity as described in section 2.3.3. A photo of the set-up is shown in fig. 5.3, where the end mirrors and beams have been drawn in for clarity. Various objectives were used to deliver the pump light to the channel waveguide in order to establish the optimum coupling. The best results were obtained when using a 30× microscope objective to collimate the pump light and a 10× objective to focus the light into the waveguide. This gave a spot size of approximately 18 μm e^{-2} diameter and the numerical aperture of the incoming beam was 0.035. By slightly adjusting the

positions of the 30× objective then the incoming spot size and numerical aperture could also be varied slightly. For each waveguide this was done to ensure maximum coupling, and the exact pumping spot size used for each crystal and polarisation are included in the relevant results description.

A 1 % output coupler was used for the initial attempts at lasing in all structures. For the most promising waveguides the performance was more fully characterised by additionally using 3 % and 5 % output couplers. The absorbed pump power was estimated using the method described in section 2.3.4.

5.3.3 Loss Measurements

The final step in the waveguide characterisation was determination of the losses. The simplest way to estimate losses was by using the set-up described in section 2.4.1. This was done using an Nd:YVO_4 laser, which operated at 1064 nm. As this wavelength is close to both the pumping and lasing wavelengths of these crystals it is a suitable source to use for propagation loss measurements around these wavelengths. Furthermore, at this wavelength there is negligible absorption in the samples and so an estimate of the propagation loss was easily obtained. The output from the laser was already collimated and so only one lens was needed to couple into the waveguide. In the Yb:KYW waveguides the best coupling was achieved with a 32 mm lens, giving a 12.4 μm diameter spot. In the Yb:KGdW crystal optimum coupling was obtained with a 50 mm lens, giving a 19 μm spot size. A 20× objective collected the waveguide output, and a pinhole was used to minimise any light which had not travelled along the waveguide from reaching the detector. As this method includes coupling loss then the propagation loss quoted using this method is an upper limit; however this coupling loss was assumed to be minimal, and this conjecture is supported by the close agreement of the losses measured by the luminescence method.

The luminescence method described in section 2.4.2 was also used to measure the propagation losses of selected waveguides. The wavelength resolution of the optical spectrum analyser (OSA) was set at 2 nm with a 5.52 s sweep time, and averaging was performed over 10 readings. The focus of the pump was translated along the

waveguide in steps of 0.4 mm for each set of measurements over 8 mm of crystal length. The close agreement of the results obtained using this technique with results measured by simple transmission gave confidence in the assumption of low coupling loss for the transmission technique.

5.4 Channel Waveguide Results

5.4.1 Yb:KGdW

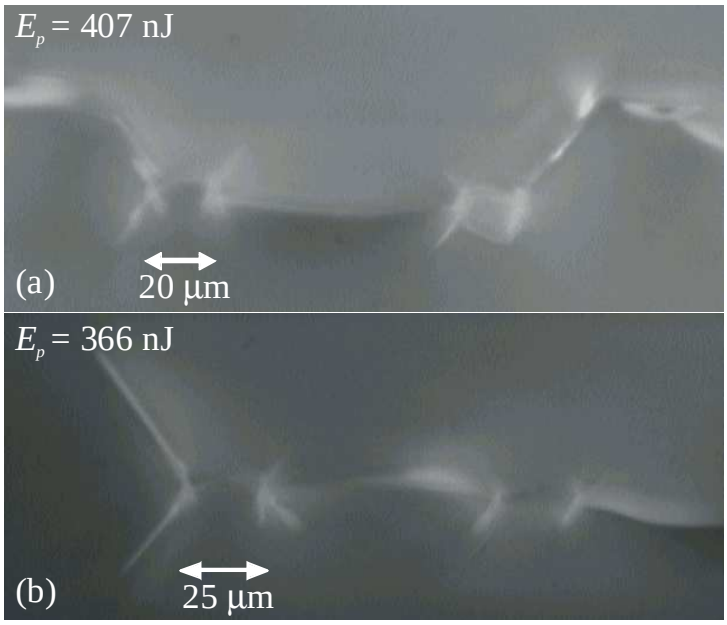

Fig. 5.4. (a) and (b) Images of structures fabricated in Yb:KGdW using linear polarisation. At pulse energies ≤ 330 nJ no modification to the crystal could be observed, whilst at energies greater than 366 nJ there was catastrophic crystal damage, with characteristic cracks along the crystallographic ***a*** axis or at angles of ~45°-50° with respect to the ***a*** axis.

It was observed that in Yb:KGdW linear polarisation gave rise to catastrophic crystal damage at all pulse energies greater than 366 nJ but no modification at pulse energies of 330 nJ or lower. Crystal cracking occurred horizontally between two tracks within a structure. Between two separate structures there was also often a horizontal crack with additional cracks at characteristic angles of ~45°-50° with respect to the horizontal. Examples of the written filaments and cracked regions are shown in fig. 5.4.

Using circular polarisation the threshold pulse energy for visible crystal modification was 350 nJ. Further damage was evident at pulse energies exceeding 369 nJ where, with a 20 μm scan separation, a crack became visible between the two written tracks. However cracking between tracks with larger separation was only apparent at pulse energies of 431 nJ or greater. At this writing energy cracking was not only present between pairs of tracks separated by up to 35 μm but continuous cracking occurred between adjacent structures which were separated by around 80 μm. These scenarios are depicted in fig. 5.5. Other interesting features are the angles of the damaged regions. The vertical line corresponds to the filament formed by the laser pulse, whilst the horizontal crack is believed to be formed along the weakest point as a result of stress induced in the crystal. Angled cracks are also evident however, and these are consistently at angles of ~45°-50°.

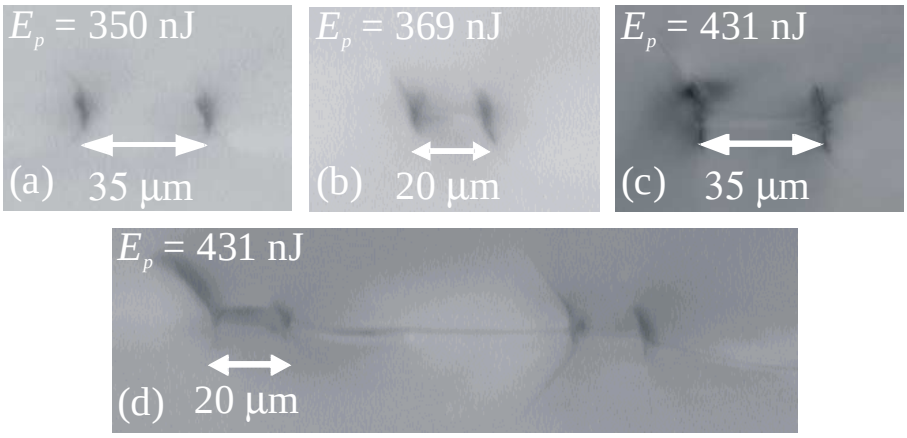

Fig. 5.5. Images of Yb:KGdW crystal modification under circularly polarised writing conditions. At 350 nJ no cracking was evident (a), whilst at only 369 nJ writing pulse energy cracking was visible between two modified regions in a structure written with 20 μm scan separation (b). At pulse energies of 431 nJ cracking can be seen in structures written with a 35 μm scan separation (c), but also between adjacent structures (d).

5.4.1.1 Guiding, Lasing and Losses in Yb:KGdW with *E*||*a*

As described in section 5.3, at higher pulse energies cracking was clearly evident between filaments. When guiding light polarised along the crystallographic ***a*** axis this cracking was not detrimental to guiding, as had been anticipated, but was found to enhance guiding performance. The waveguides were observed above and below the

cracked region, with better performance in the lower area (the side closest to the crystal edge). In structures written at lower powers, where cracking did not occur, the guiding still took place in the same regions, but the guiding was not nearly as well confined. This is evident in the images shown in fig. 5.6.

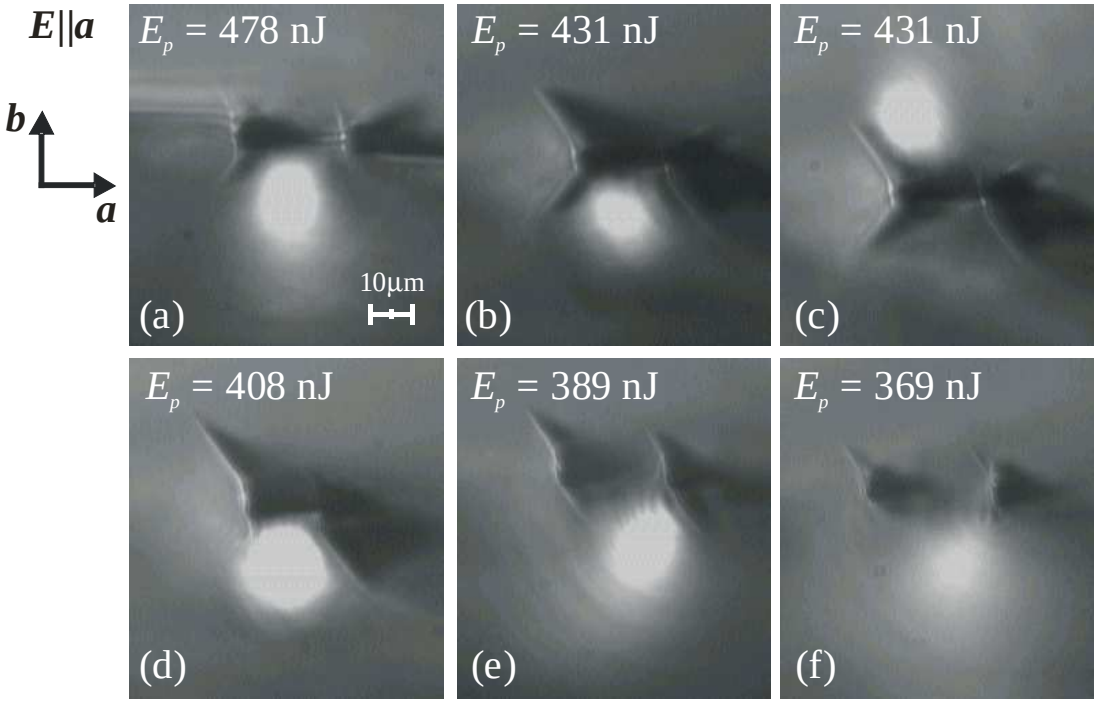

Fig. 5.6. Examples of guiding regions in Yb:KGdW with ***E*||*a***, for the pulse energies shown in the figures. (a) and (e) show a 30 μm scan separation, (b) and (c) a 25 μm scan separation, (d) a 20 μm scan separation and (f) shows a 35 μm scan separation.

Two guiding regions were found to support lasing for the available pump power. One of these regions is that illustrated in fig. 5.6 (b). This was a structure where cracking was visible between the two tracks, and the lasing waveguide was located below this cracked region, enclosed by the cracked region to the top and partially by the two filaments on either side. This structure was written in the "positive" direction with 431 nJ of pulse energy and a 25 μm scan spacing. The e^{-2} diameter of the guided mode was determined to be 25 μm (***a*** axis) by 26 μm (***b*** axis). The lasing threshold was around 170 mW absorbed pump power and the maximum power obtained with a 1 % output coupler was 4.1 mW at 1021 nm producing a 3 % slope efficiency. These results are shown in fig. 5.7.

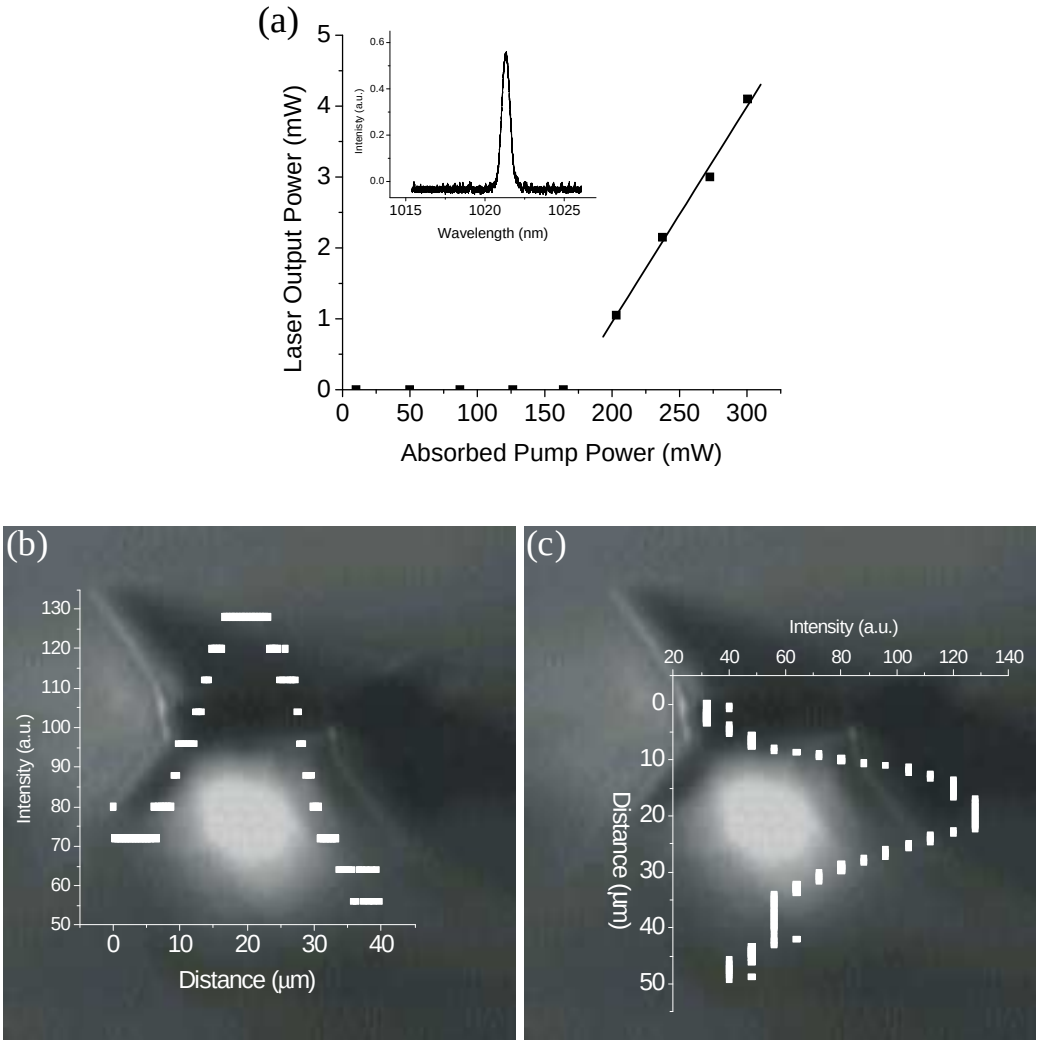

Fig. 5.7. (a) Lasing performance of a waveguide in the vicinity of the structure written with 431 nJ pulse energy in the "positive" direction with a 25 μm scan separation. The result is for 1 % output coupling. The inset shows the lasing wavelength. (b) and (c) show the profile of the guided mode.

The best performance of all inscribed waveguides was observed surrounding the structure written with 408 nJ of pulse energy and a 20 μm scan separation. As before, although there were two ***a*** polarised guiding regions surrounding the structure, above and below the cracked region as illustrated in fig. 5.5 (c) and (d), only the lower waveguide produced lasing. This waveguide gave 9 mW output power using a 1 % output coupler, with a threshold of 100 mW, corresponding to a 4.3 % slope efficiency. Using a 3 % output coupler 15 mW was obtained with a 7.8 % slope efficiency. The maximum output power was 18.6 mW with a 9.3 % slope efficiency, obtained with a 5 % output coupler. The lasing wavelength for all output couplers was around 1023 nm. The e^{-2} diameter of the guided lasing mode was 27 μm (***a*** axis) by

30 μm (***b*** axis). These results are all shown in fig. 5.8. The M^2 of the beam was found to be 1.5 and 1.2 in the ***a*** and ***b*** axes respectively, indicating the predominant mode to be that of the fundamental Gaussian. Based on these measurements the average refractive index step from the bulk to waveguide region was estimated to be 0.8×10^{-3} and 1.3×10^{-3} in the ***a*** and ***b*** axes respectively at 1020 nm.

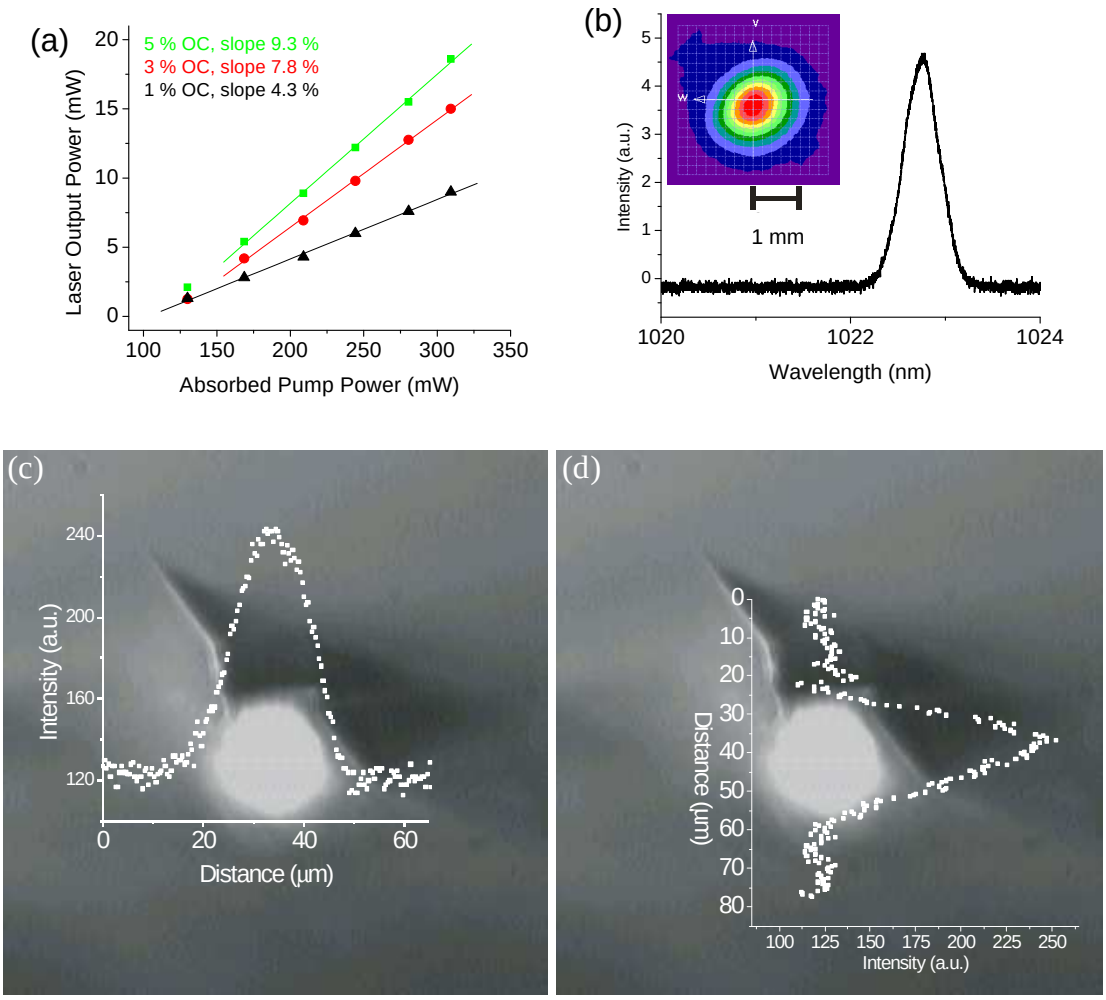

Fig. 5.8. (a) Output power performance of the waveguide laser fabricated using 408 nJ pulse energy. (b) Lasing wavelength with inset showing far field beam profile. (c) and (d) show the profile of the guided mode as it exits the waveguide.

Losses were estimated for this waveguide using the luminescence method and by transmission at 1064 nm. The transmission results are shown in fig. 5.9 where Fresnel losses have been accounted for. From these measurements an upper limit on the propagation loss was estimated at 1.9 $dBcm^{-1}$.

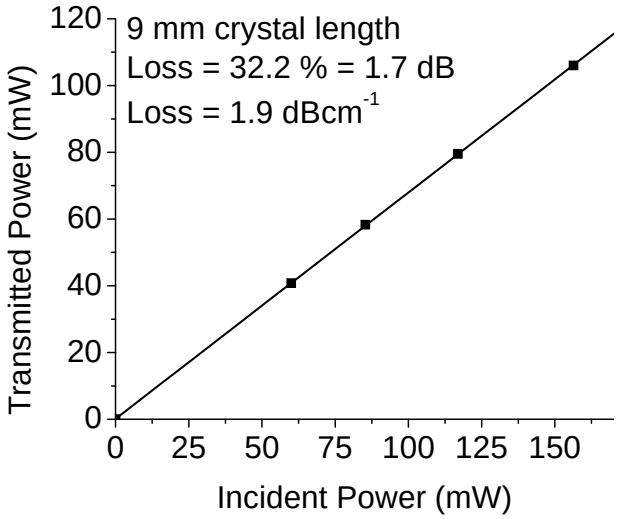

Fig. 5.9. Transmitted power at 1064 nm for various incident powers. This allows an upper limit for the propagation loss to be estimated at 1.9 dBcm^{-1}.

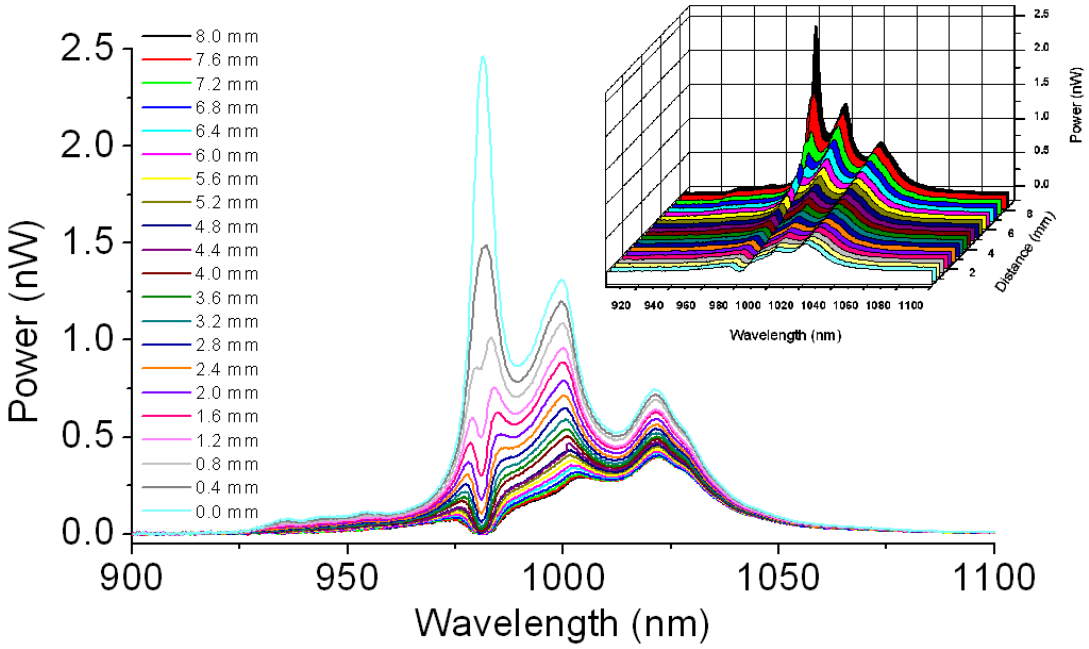

Fig. 5.10. Plots of the luminescence recorded at one end of the waveguide for various points of excitation within the waveguide. This shows the decay in luminescence as a function of propagation length in the waveguide. These measurements correspond to the waveguide close to the structure written with 408 nJ pulse energy and a 20 μm scan separation, as described in the above section.

The recorded decay in luminescence as a function of propagation length can be seen in fig. 5.10. Using this graph the loss at various wavelengths could be estimated by fitting an exponential decay, and these values are shown in table 5.1. The losses are

clearly high at 980 nm, as a result of the absorption peak at this wavelength; whilst at 1050 nm there is negligible absorption and therefore propagation loss can be estimated at 2.1 $dBcm^{-1}$, in close agreement with the losses estimated from the transmission measurement. The losses at the lasing wavelength were found to be 3.6 $dBcm^{-1}$. The close proximity of 1020 nm and 1050 nm means that the propagation loss at 1020 nm can also be estimated at 2.1 $dBcm^{-1}$. As the total loss at this wavelength was 3.6 $dBcm^{-1}$ then the reabsorption loss was estimated to be 1.5 $dBcm^{-1}$ by simply subtracting the propagation loss.

Wavelength (nm)	**Loss over crystal (%)**	**Loss over crystal (dB)**	**Loss per cm ($dBcm^{-1}$)**
981	99.999	51.8	57.5
1000	87.09	8.9	9.9
1021	52.36	3.2	3.6
1050	34.68	1.9	2.1

Table 5.1. Loss measured by fitting exponential decays to the results from fig. 5.10. At 980 nm the loss is dominated by absorption loss, whilst at 1050 nm the absorption loss is negligible.

Transmission loss measurements were also taken for many non-lasing structures, and the losses are summarised in table 5.2. From this it is clear that a propagation loss 2.4 $dBcm^{-1}$ or below is required in Yb:KGdW to obtain lasing with the available pump power for polarisation along the ***a*** axis.

Writing Pulse Energy (nJ)	**Scan separation (μm)**	**Guiding Region**	**Propagation and coupling loss over crystal length (%)**	**Propagation and coupling loss over crystal length (dB)**	**Maximum propagation loss ($dBcm^{-1}$)**
408	**20**	**lower**	**32.2**	**1.7**	**1.9**
408	20	upper	40.6	2.3	2.5
431	**25**	**lower**	**39.5**	**2.2**	**2.4**
431	25	upper	44.9	2.6	2.9
453	25	lower	60.7	4.1	4.5
478	35	lower	62	4.2	4.7

Table 5.2. Propagation loss measured for various waveguides using the transmission method. All structures were written in the positive direction. The two lasing structures are illustrated in bold.

5.4.1.2 Guiding, Lasing and Losses in Yb:KGdW with *E*||*b*

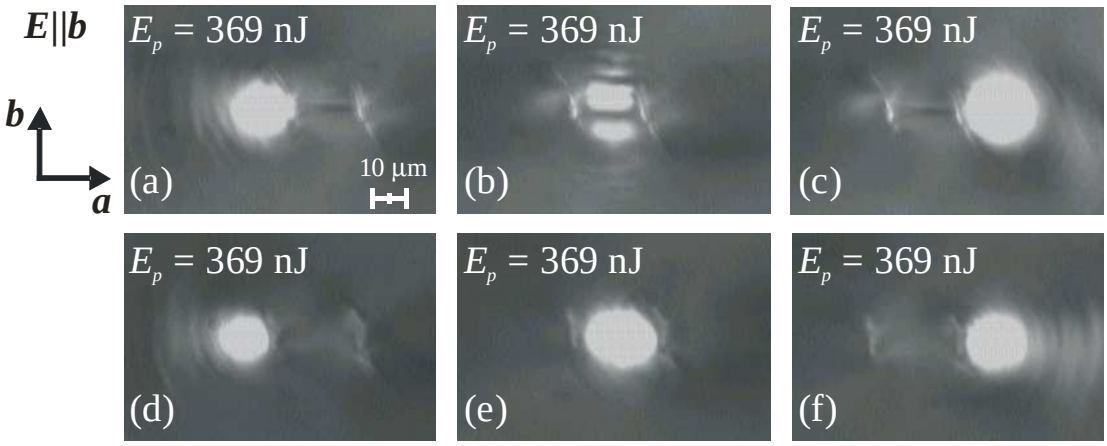

Fig. 5.11. ***E*||*b*** guiding regions in Yb:KGdW in structures inscribed using a writing pulse energy of 369 nJ, and a scan separation of (a, b, c) 20 µm or (d, e, f) 25 µm.

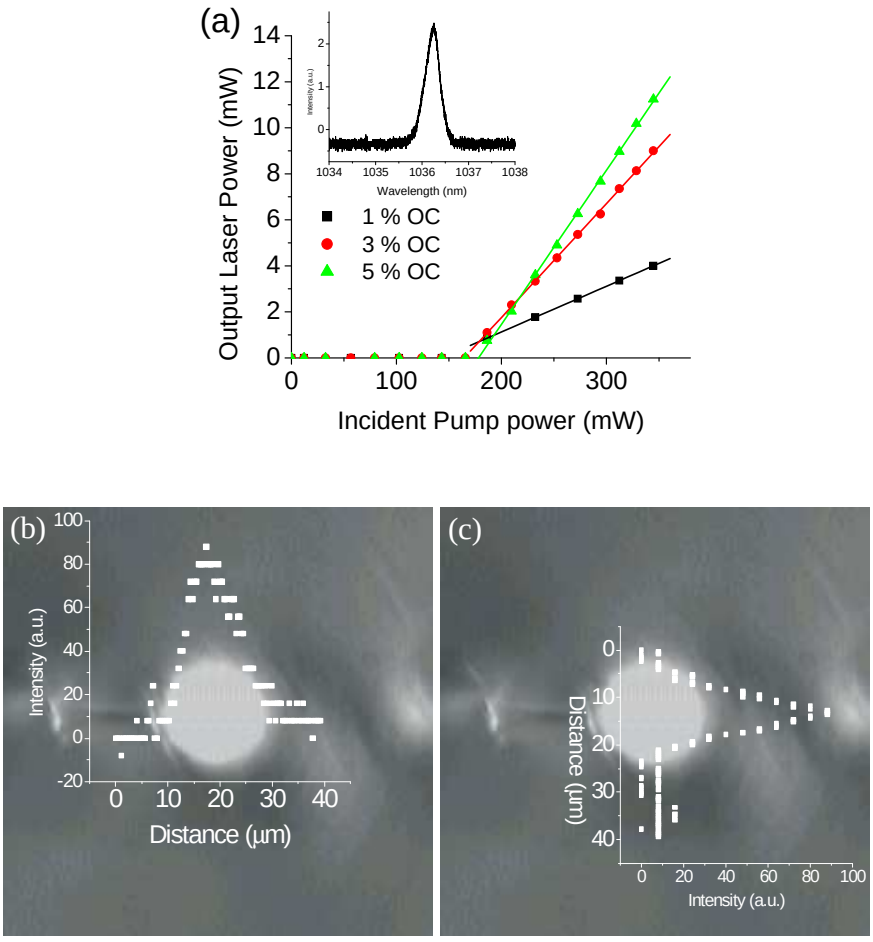

Fig. 5.12. (a) ***E*||*b*** output power performance for the waveguide laser written with 369 nJ pulse energy and a 20 µm scan separation. Inset shows the lasing wavelength. (b) and (c) show the guided mode profiles.

With polarisation along the crystallographic ***b*** axis guiding was found to occur along the central region and also to the left and right of the modified tracks. The threshold writing energy for guiding was slightly higher, with pulse energies of 369 nJ or greater required. In structures where cracking had occurred down the centre of the two tracks guiding was of course hindered (fig. 5.11 (b)), but guiding was still observed in left and right hand regions (fig. 5.11 (a) and (c)). In structures where there was no cracking in the central region (d, e, f) a smooth central guiding region could be observed (e). For waveguides written in the positive direction right hand regions gave a smoother profile, as is clear from the images in the figure. The guided modes were smaller than those observed in Yb:KGdW for polarisation along the ***a*** axis with e^{-2} diameters of around 18 μm as shown in fig. 5.12 (b, c).

Lasing was observed in two waveguides. These were the right-hand guiding regions for structures with a 20 μm scan separation written with 369 nJ and 389 nJ of pulse energy. They gave very similar lasing performance with output powers of around 4 mW using a 1 % output coupler. The lasing threshold was around 170 mW incident pump power for the 369 nJ written waveguide, and 180 mW for the waveguide written with 389 nJ pump power. Fuller characterisation of the structure written at 369 nJ was performed using 3 % and 5 % output powers, giving a maximum output power of 11.2 mW using the 5 % output coupler. These results are shown in fig. 5.12 (a). The lasing wavelength was around 1036 nm, as presented in the inset. The divergence (half-angle) was measured to be 28 mrad and 29 mrad along the ***a*** and ***b*** axis respectively.

Using the transmission loss method losses were measured to be 2.9 $dBcm^{-1}$ in both of the lasing waveguides. The losses of the two lasing structures and a selection of the non-lasing structures are presented in table 5.3.

Writing Pulse Energy (nJ)	Scan separation (μm)	Guiding Region	Propagation and coupling loss over crystal length (%)	Propagation and coupling loss over crystal length (dB)	Maximum propagation loss ($dBcm^{-1}$)
408	20	right	48.6	2.9	3.2
408	20	centre	80.7	7.1	7.9
408	20	left	68.9	5.1	5.6
408*	35	centre	47.9	2.8	3.2
389	**20**	**right**	**45.6**	**2.6**	**2.9**
389	20	centre	77.7	6.5	7.2
389	20	left	57.3	3.7	4.1
389	30	right	52.1	3.2	3.6
389	30	centre	49.4	3.0	3.3
389	30	left	54.6	3.4	3.8
389	35	right	50.4	3.1	3.4
389	35	centre	46.9	2.8	3.1
389	35	left	55.1	3.5	3.9
369	**20**	**right**	**44.8**	**2.6**	**2.9**
369	20	centre	69.6	5.2	5.8
369	20	left	50.2	3.0	3.4
369*	20	right	52.3	3.2	3.6
369*	20	centre	80.4	7.1	7.9
369*	20	left	52.2	3.2	3.6
369	25	right	52.3	3.2	3.6
369	25	centre	59	3.9	4.3
369	25	left	52.6	3.2	3.6
369*	25	centre	75.7	6.1	6.8
369	30	right	57.5	3.7	4.1
369	30	centre	50	3.0	3.3
369	30	left	57.5	3.7	4.1
369*	30	centre	45.6	2.6	2.9
369	35	centre	48.5	2.9	3.2
369*	35	centre	53.1	3.3	3.7

Table 5.3. Propagation loss measured for various waveguides using the transmission method. Structures written in the negative direction are identified by an asterisk. Lasing structures are illustrated in bold.

5.4.2 Yb:KYW

In the Yb:KYW crystal structural modification was evident in the written volume at pulse energies of 339 nJ and greater. However, even at the highest writing energy of 578 nJ there was no evidence of further cracking or damage outside of this region when imaging the end facet (fig. 5.13), as had been the case for Yb:KGdW.

Fig. 5.13. Image of Yb:KYW end facet, showing the laser induced structural modification.

5.4.2.1 Guiding, Lasing and Losses in Yb:KYW with *E*||*a*

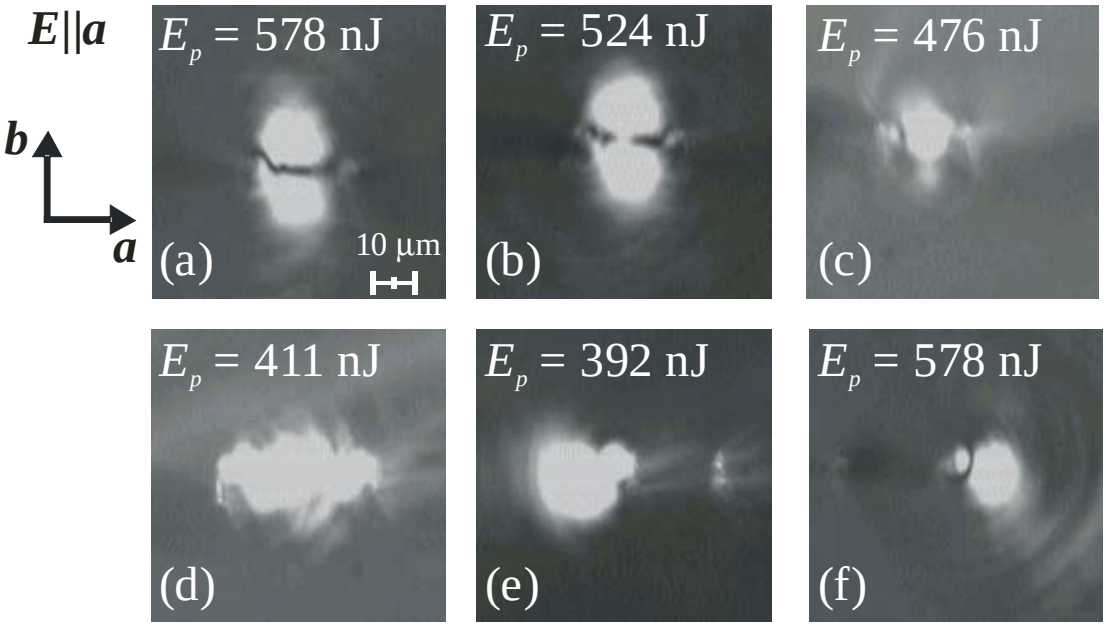

Fig. 5.14. ***E*||*a*** guiding regions surrounding structures written in Yb:KYW at the pulse energies shown and with scan separations of: (a) 25 μm, (b) 25 μm, (c) 20 μm, (d) 35 μm, (e) 20 μm, (f) 25 μm.

Initially guiding was investigated for polarisation along the crystallographic ***a*** axis which, as was discussed in Chapter 1, is the polarisation with largest absorption and

emission cross sections. Guiding regions were identified in many structures, but of rather poor quality. In structures written with energies between 339 nJ – 432 nJ the central guiding region did not have a smooth intensity shape (fig. 5.14 (d)). At larger pulse energies a region resembling a TEM_{01} mode was visible (a, b). This may be a result of some subtle cracking, similar to that observed in Yb:KGdW but not so pronounced so as to be visible under examination of the end facet as was the case in Yb:KGdW. To the left and right of the modified tracks circular guiding regions with additional, slightly offset, small circular spots were observed. Examples of these guiding patterns are shown in fig. 5.14 (e, f).

As could be expected given the poor beam quality of the guided modes in Yb:KYW for polarisation along the ***a*** axis, no lasing was obtained from these structures. Propagation losses for all guiding regions were estimated to exceed 4.5 $dBcm^{-1}$ at 1060 nm using the transmission loss method. The losses of a few structures are quoted in table 5.4.

Writing Pulse Energy (nJ)	**Scan separation (μm)**	**Guiding Region**	**Propagation and coupling loss over crystal length (%)**	**Propagation and coupling loss over crystal length (dB)**	**Maximum propagation loss ($dBcm^{-1}$)**
411	20	left	72.8	5.7	6.3
411	20	centre	67.7	4.9	5.5
411*	20	right	73	5.7	6.3
392	20	centre	60.4	4.0	4.5
392*	20	centre	79.3	6.8	7.6
373	20	centre	69.8	5.2	5.8
355	20	centre	70.5	5.3	5.9

Table 5.4. Propagation loss measured for various waveguides in Yb:KYW with ***E*||*a*** using the transmission method. Structures fabricated in the negative direction are identified by an asterisk.

5.4.2.2 Guiding, Lasing and Losses in Yb:KYW with *E*||*b*

With the InGaAs laser polarised along the crystallographic ***b*** axis Gaussian guiding profiles were observed in the central region and also in both side regions of each pair

of tracks, as illustrated in fig. 5.15. The waveguides all had radii (e^{-2}) of around 6 μm along the ***a*** axis and approximately 7 μm to 8 μm along the ***b*** axis. Examples of the waveguide profiles are shown in fig. 5.15 (a and b). It is interesting to note that only the central guiding region is symmetric along the ***a*** axis, whilst the side region has a steeper edge to the side where the filament lies. This was expected and is attributed to the sudden lower index barrier which is formed at the focal volume in contrast to the gradual decline in the refractive index profile due to the diminishing stress on the opposite side of the waveguide.

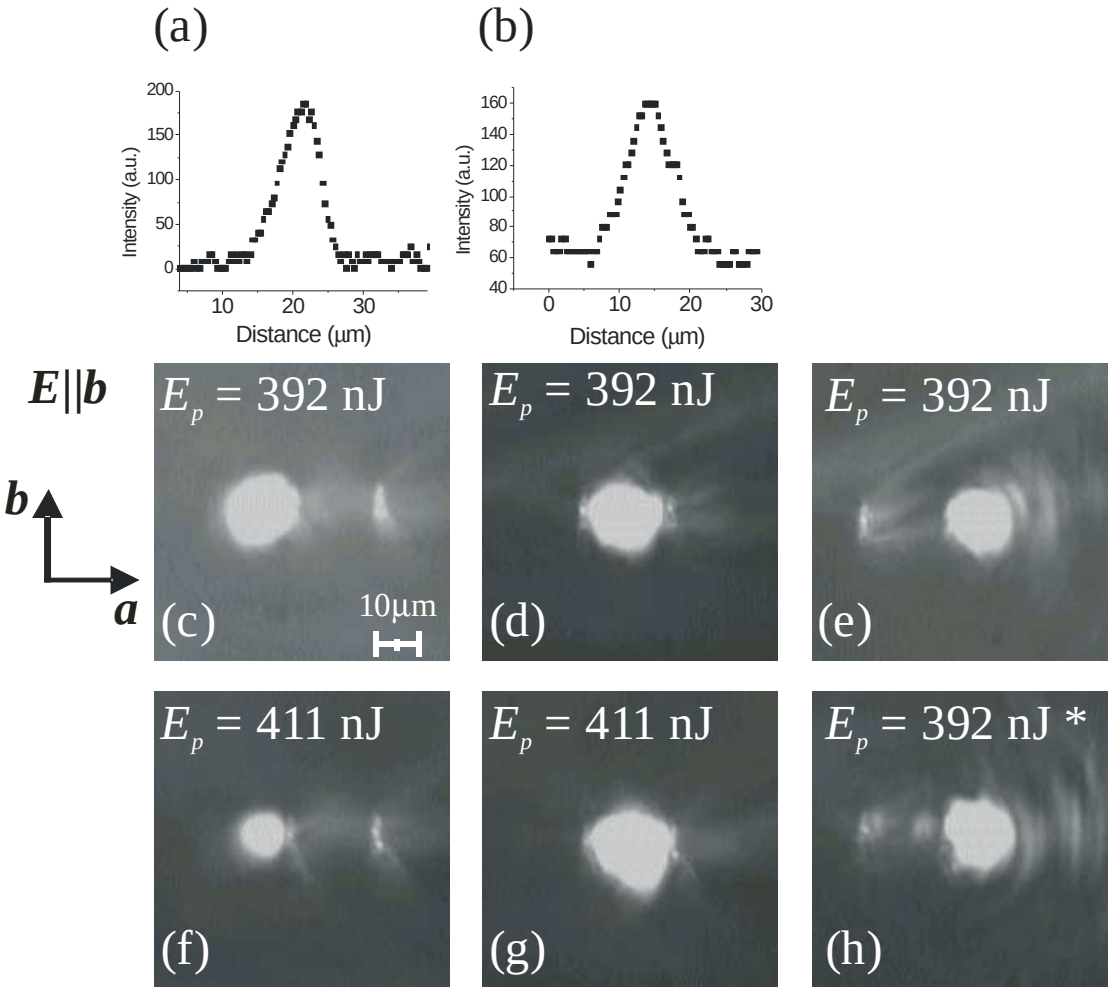

Fig. 5.15. ***E*||*b*** guiding profiles and regions in Yb:KYW for structures written with a 20 μm scan separation, and pulse energies as shown in the images. The asterisk denotes a structure written in the negative direction, whilst all other structures were written in the positive direction. (a) is the profile of the image shown in (c), with a diameter of 11.2 μm, and (b) is the profile of the image shown in (d) with a diameter of 12.5 μm.

As stated in section 5.3.1 the relative quality of the waveguides could be estimated by recording the transmitted pump power, as waveguides of a higher quality reach absorption saturation at lower pump powers and will transmit more power at maximum pumping. The is clearly illustrated in fig. 5.16 where the waveguides which showed the highest transmittance at maximum pump power were also found to be those structures which were able to lase. For clarity the figure only shows structures written with a 20 μm scan spacing, but those waveguides formed using larger scan spacings gave results that followed the same pattern.

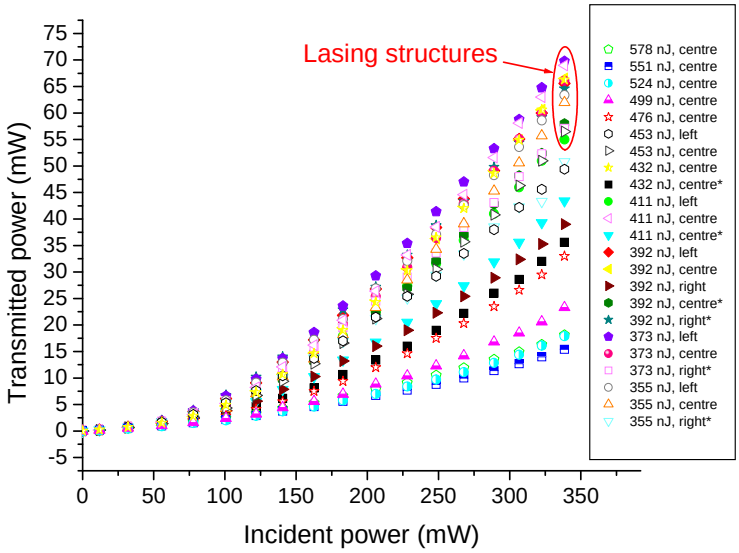

Fig. 5.16. Transmitted power as a function of incident power at 980 nm through various guiding regions. The regions shown are all for structures written with a 20 μm scan separation, and energies as labelled in the key. Structures fabricated by writing in the negative direction are identified by an asterisk. This graph was used to identify the most promising waveguides, as the lowest loss waveguides show highest transmittance at maximum incident power. This was later confirmed in lasing experiments, as the structures circled in the graph were those which lased.

Consistent lasing performance was observed in Yb:KYW where 16 waveguides, written at pulse energies ranging from 355 nJ – 453 nJ, were found to lase. Clear patterns in the writing conditions which produced lasing were evident. All left and central guiding regions written in the "positive" direction with a 20 μm scan separation at pulse energies from 355 nJ – 432 nJ were found to lase. It was found that left hand regions gave lower thresholds than their central counterparts, implying a lower propagation loss. Thus, although writing two tracks for a given structure gave a more symmetric central waveguide, this did not serve to enhance the lasing

performance as it led to an increased loss, presumably as a result of increased scattering due to greater interaction of the guided mode with the damaged region. Duplicates of some structures, with pulse energies between 339 nJ and 392 nJ, were inscribed (see Appendix A for details). In the second set only the structure written at 392 nJ of pulse energy with a 20 μm spacing gave lasing regions, but with higher threshold. The structures written at 355 nJ and 373 nJ were surprisingly unable to lase. The reason for this was investigated further and it was found that these duplicate structures had been written at a slightly lower depth – 370 μm below the surface compared to 360 μm for the first set – and this accounts for the poorer performance. The effect of depth of focus and the focusing geometry was not investigated in this study, but it clearly has an effect and is an area for future work.

For structures written in the "negative" direction, lasing was observed only in right hand regions, in structures written with 411 nJ and 392 nJ pulse energy. The writing direction is therefore shown to effect whether guiding occurs in left, central or right hand regions. Writing direction has previously been highlighted as a factor in determining the waveguide performance. It has been attributed to wavefront tilt and has been dubbed the "quill effect" [10]. Under conditions of such tight focusing and the formation of electron plasma at the focus, even a small amount of anisotropy in the frequency distribution of the incident beam creates substantial wavefront tilt at the written volume. This leads to a intensity gradient, which applies a ponderomotive force to the free electrons generated during the writing process [11]. The guiding results shows that this is a significant effect in the set-up used at Heriot Watt, influencing the losses of the waveguides. Further work is needed to investigate and optimise this effect.

Another interesting point is the effect of scan separation. For structures written in the "positive" direction, only those with a 20 μm scan separation produced lasing regions, whilst lasing was observed in structures with 20 μm or 25 μm scan separation for writing along the "negative" direction. Although the scan separation was expected to influence the behaviour and performance of the central guiding region, it was not expected to have such an effect on the side regions. It had been assumed that the side guiding region would only depend on the particular parameters of the directly adjacent filament. Thus, for a given pulse energy, the same performance had been

expected in the 20 μm separation structure as for the 35 μm separation structure. Clearly this was not the case, and it can be concluded that the structures outside the vicinity of the waveguide also play an important role in determining the waveguide quality; suggesting that the induced stress extends further than the filament's immediate locality.

Writing Pulse Energy (nJ)	**Scan separation (μm)**	**Guiding Region**	**Lasing results (1% output coupler)**	
			Threshold – incident power (mW)	**Maximum power (mW)**
453	20	centre	201	2.1
432	20	left	236	Lasing
432	20	centre	265	Lasing
411	20	left	116	2.2
411	20	centre	124	2.2
411*	20	right	322	Lasing
392	20	left	128	2.2
392	20	centre	143	2.0
392*	20	right	182	2.2
392*	25	right	205	2.0
392^{dupl}	20	left	201	Lasing
392^{dupl}	20	centre	170	Lasing
373	20	left	166	2.1
373	20	centre	196	1.9
355	20	left	245	1.9
355	20	centre	182	Lasing

Table 5.5. Summary of incident power threshold for all identified lasing waveguide in Yb:KYW with ***E*||*b***. Structures fabricated in the negative direction are represented by an asterisk, dupl. indicates duplicated structures, which were written 10 μm deeper in the sample, explaining the higher thresholds.

The 16 waveguides previously described all lased around 1037 nm with thresholds as low as 70 mW and output powers as high as 2.2 mW with a 1 % output coupler. A summary of the lasing results for all of these structures is presented in table 5.5. By considering the lasing threshold, a writing pulse energy of 392 nJ – 411 nJ with 20 μm scan separation can clearly be considered to be optimum. Lasing performance for the structure written with 411 nJ pulse energy was therefore also characterised using a

3 % and 5 % output coupler. The maximum output power with the 5 % output coupler was 8.2 mW, as illustrated in fig. 5.17.

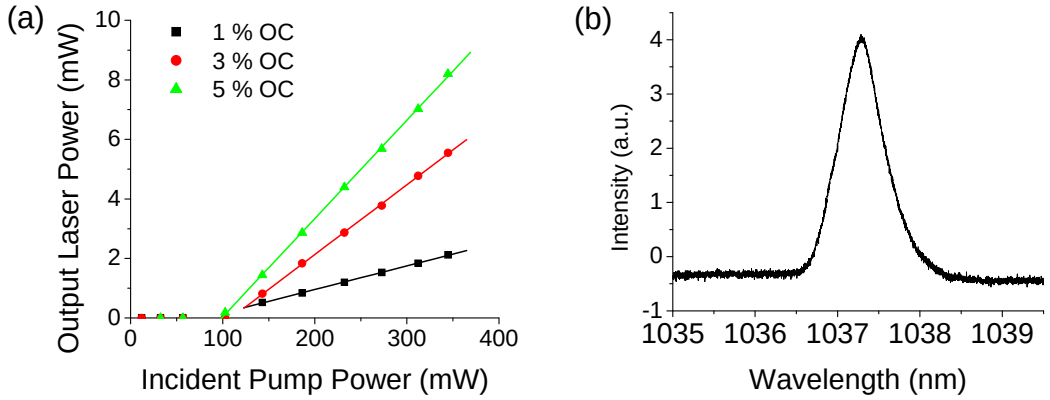

Fig. 5.17. (a) Laser performance for the left hand guiding region of the structure written with 411 nJ pulse energy and a 20 μm scan separation in the positive writing direction. (b) Lasing wavelength.

Writing Pulse Energy (nJ)	**Scan separation (μm)**	**Guiding Region**	**Propagation and coupling loss over crystal length (%)**	**Propagation and coupling loss over crystal length (dB)**	**Maximum propagation loss ($dBcm^{-1}$)**
411	**20**	**centre**	**53.1**	**3.3**	**3.7**
411	**20**	**left**	**55.8**	**3.5**	**3.9**
411*	**20**	**right**	**62.8**	**4.3**	**4.8**
411*	25	right	63.8	4.4	4.9
392	**20**	**centre**	**55**	**3.5**	**3.8**
392	**20**	**left**	**55.8**	**3.6**	**3.9**
392*	**20**	**right**	**60.3**	**4.0**	**4.5**
392*	20	centre	67.1	4.8	5.4
392*	**25**	**right**	**60.1**	**4.0**	**4.4**
373	**20**	**centre**	**54.3**	**3.4**	**3.8**
373	**20**	**left**	**56.7**	**3.6**	**4.0**
355	**20**	**centre**	**58**	**3.8**	**4.2**
355	**20**	**left**	**59.4**	**3.9**	**4.4**
339	20	right	81.9	7.4	8.3
339	20	centre	68.3	5.0	5.5

Table 5.6. Propagation loss measurements using the transmission method for various waveguides in Yb:KYW with ***E*||*b***. Structures written in the negative direction are identified by an asterisk whilst lasing waveguides are illustrated in bold.

Using the transmission loss method, the propagation losses at 1060 nm were measured to be between 3.7 dBcm^{-1} and 4.8 dBcm^{-1} in all lasing structures, but 4.9 dBcm^{-1} or greater in non-lasing structures, as summarised in table 5.6. The central regions were determined to have slightly lower losses than their side region counterparts, even though lasing performance was better in the side regions. This could be a result of improved coupling to the central symmetric region when compared to the side region during the transmission loss measurements, giving lower coupling losses and thus a more accurate measurement of propagation loss in the central regions, but a slightly high value in the side regions. In each case it is interesting to note the left hand region's loss is always measured to be 0.1 dB or 0.2 dB higher than the central region's, strengthening the argument of increased coupling loss in the side region.

Pulse energy (nJ)	Wavelength (nm)	Loss over crystal (%)	Loss over crystal (dB)	Propagation loss (dBcm^{-1})
411	980.9	99.87	28.7	31.9
	999.9	80.61	7.1	7.9
	1037.1	63.38	4.4	4.8
	1060	54.63	3.4	3.8
392	980.9	99.66	24.7	27.5
	999.9	80.95	7.2	8
	1037.1	63.19	4.3	4.8
	1060	51.13	3.1	3.5
392*	980.9	99.86	29.8	33.1
	999.9	86.32	8.6	9.6
	1037.1	79.68	6.9	7.7
	1060	69.17	5.1	5.7

Table 5.7. Luminescence loss measurements using ***E*||*b*** polarisation for waveguides located in central regions of the structures fabricated at the shown energy and with a 20 μm scan separation. Structures written in the negative direction are identified by an asterisk. The measurements at 1060 nm are in close agreement with those recorded using the transmission loss method, as summarised in table 5.6.

The luminescence decay method was also used on three waveguides, and the results are summarised in table 5.7. Good agreement is seen between results from the luminescence method and the transmission method, with a discrepancy of between 0.1 dBcm^{-1} and 0.3 dBcm^{-1}.

5.5 Conclusions and Future Work

In this chapter the fabrication of channel waveguides in crystalline Yb:KGdW and Yb:KYW by ultrafast laser inscription have been presented. The guiding properties of the resulting structures were investigated and it was found that the resulting guiding regions were polarisation dependent. In all cases circular polarisation and 20 μm scan separations gave the best results with the production of the lowest loss waveguides. In Yb:KGdW it was observed that 330 nJ of pulse energy was necessary in order to create filaments at the beam's focus, but that cracks were formed between the two written filaments when using writing pulse energies of 366 nJ. In Yb:KYW pulse energies of 339 nJ or greater were necessary for crystal modification, but even at the highest writing pulse energy of 578 nJ no cracking was evident between the filaments.

For the first time lasing was demonstrated in ULI channel waveguides of these materials, with output powers as high as 18.6 mW in Yb:KGdW for $\boldsymbol{E||a}$ polarisation. This was realised in a region below the crack and between filaments in a structure written with 408 nJ of pulse energy. With polarisation along the $\boldsymbol{b}$ axis optimal guiding was obtained in a side region and writing pulse energies of 369 nJ and 389 nJ produced lasing waveguides. In Yb:KYW lasing was consistently found in the central and left side regions of structures written with pulse energies in the region of 355 nJ – 432 nJ, where the optimal results were found in the side guiding region at pulse energies of 392 nJ or 411 nJ. Even although the output power and slope efficiencies demonstrated are significantly lower than those of bulk or LPE planar waveguide lasers based on these materials, the excellent beam quality together with the compact cavity illustrate the advantages of the channel waveguide. Future work in this area will therefore focus on the improvement of waveguides fabricated by ULI by exploring further writing parameters, such as wavefront tilt, but also by seeking to understand further the modifications within the crystal which have taken place. The fabrication of Yb:KGdW and Yb:KYW channel waveguides using other techniques is also an interesting area which needs to be explored further. As fabrication techniques improve the full potential of Yb:tungstate channel waveguides is expected to be realised.

5.6 References

[1] T. Gorelik, M. Will, S. Nolte, A. Tuennermann and U. Glatzel, "Transmission electron microscopy studies of femtosecond laser induced modifications in quartz," Applied Physics A-Materials Science & Processing **76,** 309-311 (2003).

[2] V. Apostolopoulos, L. Laversenne, T. Colomb, C. Depeursinge, R. P. Salathé, M. Pollnau, R. Osellame, G. Cerullo and P. Laporta, "Femtosecond-irradiation-induced refractive-index changes and channel waveguiding in bulk Ti^{3+}:Sapphire," Applied Physics Letters **85,** 1122-1124 (2004).

[3] K. Kawamura, M. Hirano, T. Kurobori, D. Takamizu, T. Kamiya and H. Hosono, "Femtosecond-laser-encoded distributed-feedback color center laser in lithium fluoride single crystals," Applied Physics Letters **84,** 311-313 (2004).

[4] A. G. Okhrimchuk, A. V. Shestakov, I. Khrushchev and J. Mitchell, "Depressed cladding, buried waveguide laser formed in a YAG:Nd^{3+} crystal by femtosecond laser writing," Optics Letters **30,** 2248-2250 (2005).

[5] G. A. Torchia, A. Rodenas, A. Benayas, E. Cantelar, L. Roso and D. Jaque, "Highly efficient laser action in femtosecond-written Nd : yttrium aluminum garnet ceramic waveguides," Applied Physics Letters **92,** 111103-111105 (2008).

[6] J. Siebenmorgen, T. Calmano, K. Petermann and G. Huber, "Fabrication of a Stress-Induced Nd:YAG Channel Waveguide Laser using fs-Laser Pulses," Talk MB29 presented at Advanced Solid-State Photonics in Denver, Colarado (2009).

[7] S. M. Eaton, C. A. Merchant, R. Iyer, A. J. Zilkie, A. S. Helmy, J. S. Aitchison, P. R. Herman, D. Kraemer, R. J. D. Miller, C. Hnatovsky and R. S. Taylor, "Raman gain from waveguides inscribed in $KGd(WO_4)_2$ by high repetition rate femtosecond laser," Applied Physics Letters **92,** 81105-81107 (2008).

[8] C. N. Borca, V. Apostolopoulos, F. Gardillou, H. G. Limberger, M. Pollnau and R. P. Salathé, "Buried channel waveguides in Yb-doped $KY(WO_4)_2$

fabricated by femtosecond laser irradiation," Applied Surface Science **253,** 8300-8303 (2007).

[9] F. M. Bain, A. A. Lagatsky, R. R. Thomson, N. D. Psaila, N. V. Kuleshov, A. K. Kar, W. Sibbett and C. T. A. Brown, "Ultrafast laser inscribed Yb:$KGd(WO_4)_2$ and Yb:$KY(WO_4)_2$ channel waveguide lasers," Optics Express **17,** 22417-22422 (2009).

[10] P. G. Kazansky, W. J. Yang, E. Bricchi, J. Bovatsek, A. Arai, Y. Shimotsuma, K. Miura and K. Hirao, ""Quill" writing with ultrashort light pulses in transparent materials," Applied Physics Letters **90,** 151120-151122 (2007).

[11] W. L. Kruer, "The Physics of Laser Plasma Interactions", Addison-Wesley, 1988, vol. 73, p.60

Chapter 6
Micro-spectroscopy of Channel Waveguides

6.1 Introduction

Although ULI has been used to fabricate waveguides in a wide variety of optical materials, the physical changes responsible for the creation of the waveguides are still not well understood. Waveguide imaging has previously been performed by secondary ion mass spectroscopy (SIMS) which can provide sub-micron analysis of the waveguide's chemical composition, but only in the vicinity of the waveguide surface [1]. Methods combining chemical etching and atomic force microscopy (AFM) have also been demonstrated but require destruction of the waveguide [2]. Transmission Electron Microscopy (TEM) is a valuable technique which has successfully been used to study the structural changes caused by femtosecond laser pulses in crystals and glasses [3], but this requires substantial sample preparation to cut thin slices of the irradiated material, and again this results in the destruction of parts of the sample. Two non-destructive techniques which have recently been employed to analyse waveguide spectroscopy on a micro-scale are confocal micro-luminescence [4] and confocal micro-Raman [5]. These techniques offer the possibility of 3D mapping of the waveguide and provide detailed information not only on the damaged filament, but also of the surrounding regions.

In this chapter confocal micro-luminescence and micro-Raman measurements of channel waveguides fabricated in Yb:KGdW and Yb:KYW by ULI are presented. These waveguides are some of those which were described in the previous chapter (Chapter 5). I performed these measurements together with Wagner Silva[1] using a set-up at the Universidad Autónoma de Madrid in Spain through a collaboration with Dr Daniel Jaque[2].

[1] W. F. Silva, Instituto de Física, Universidade Federal de Alagoas, 57072-907 Maceió, AL, Brazil
[2] D. Jaque, Departmento de Física de Materiales C-IV, Universidad Autónoma de Madrid, 28049 Madrid, Spain

6.2 Experimental Set-up

Experiments were carried out using a BX-41 fibre coupled confocal microscope, where a ×50 IR objective with an N.A. of 0.55 was used to focus on to and collect the light from the crystal in micro-luminescence measurements, and a ×50 objective with an N.A. of 0.75 was used for micro-Raman measurements. Various laser sources were available to use for excitation of the crystal. For the micro-luminescence experiments reported here a Ti:sapphire laser tuned to 940 nm was used. This corresponds to an absorption peak of the crystals (see Chapter 1, fig. 1.6). An Argon ion laser at 488 nm was used to excite the crystal when measuring Raman shift. This wavelength is shorter than that of the Ti:sapphire laser and so provides increased resolution. The emission was collected with the ×50 objective, passed through the confocal microscope, and was then detected by a CCD attached to a fibre-coupled spectrometer (SPEX 500M). A notch filter was used when performing Raman measurements to block the excitation wavelength. This set-up is illustrated in fig. 6.1.

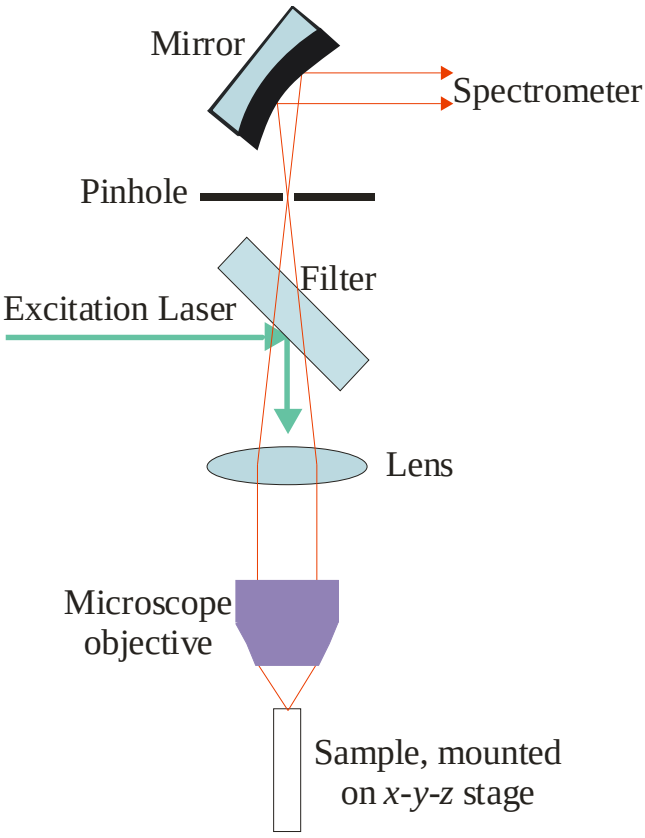

Fig. 6.1. Schematic of confocal micro-spectroscopy set-up.

The sample under investigation was mounted on a microscope slide, which was attached to a motorised *x*-*y* stage and a high precision manually controlled *z* stage. A beam splitter, mounted together with a second CCD camera, could be inserted into the beam path to view the crystal under white light illumination. This was used to align the position of the crystal and to ensure that mapped structures could be identified. The surface of the waveguide was aligned to the focal plane and then subsequently translated upwards by 5 μm such that a point slightly below the crystal facet was recorded. *LabSpec 5* software was used to set the data acquisition parameters and to collect and analyse the data. 2D maps were recorded, with a measurement of the emitted spectrum being taken every one micron over an area which was typically around 80×80 μm^2. *LabSpec 5* would then fit one or more peaks to the recorded spectrum and map how that peak varied over the scanned area. The peak could vary in three key manners: the intensity of the emitted peak could drop or increase; the peak of the emission could shift; and the width of the emitted peak could vary. Once the shifts in these three areas had been extracted using *LabSpec 5*, the maps were plotted in WS×M© [6].

6.3 Double Tungstate Raman Spectroscopy

In order to interpret the results from the micro-Raman experiments it is vital to be familiar with Yb:KGdW and Yb:KYW crystal structure, and the Raman modes associated with various vibrations. Their crystal structure is briefly described in Chapter 1, and fuller descriptions together with observed Raman spectra are available in the literature [7-10]. Of particular importance here are the bonds responsible for the observed Raman modes. Both crystals belong to the C2/c space group and comprise of WO_6 octahedra joined by bridged WO_2W double bonds and WOW single bonds. These bonds can be characterised by several in-plane and out-of-plane vibrations, as illustrated in fig. 6.2. These vibrations have been attributed to various Raman modes, and table 6.1 summarises the key Raman modes associated with each vibrating bond. As the two crystals under investigation – Yb:KGdW and Yb:KYW – form very similar structures they have similar Raman lines, arising from the same molecular vibrations.

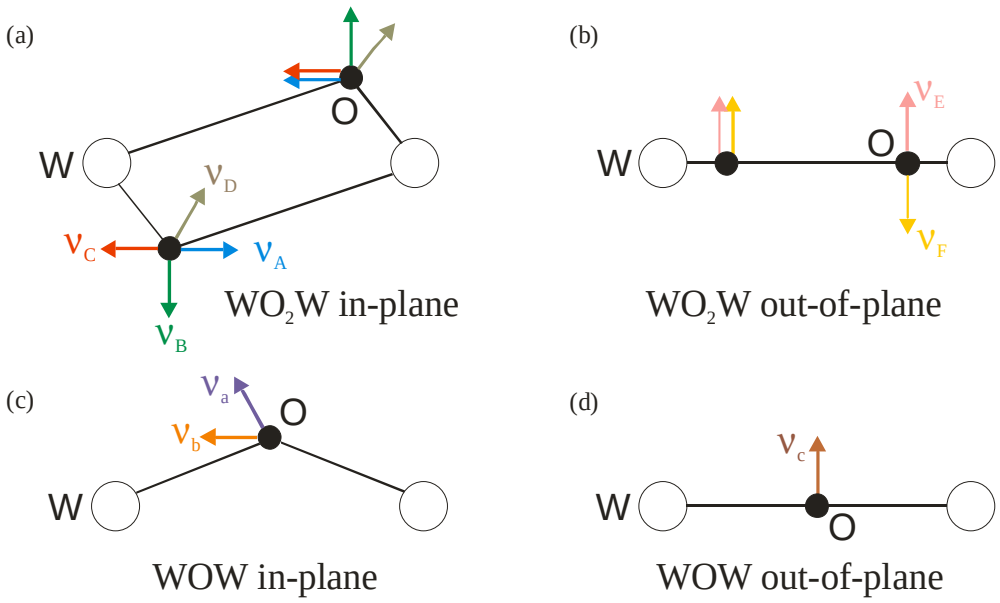

Fig. 6.2. Schematics of the vibrations associated with the (a) in-plane WO_2W bonds, (b) out-of-plane WO_2W bonds, (c) in-plane WOW bonds and (d) out-of-plane WOW bonds.

Raman Shift (cm^{-1}) of KGdW [9]	**Variation in Raman shift (cm^{-1}) for all lanthanides, KLnW, where Ln = Sm – Lu, Y [9]**	**Assignment of Raman Mode [7]**
900	9	WO_2W in-plane vibration, ν_A
805	8	WOW in-plane vibration, ν_a
768	14	WO_2W in-plane vibration, ν_B
682	9	WO_2W in-plane vibration, ν_C
527	8	WOW in-plane vibration, ν_b
498	8	WO_2W out-of-plane vibration, ν_E
437	16	WO_2W in-plane vibration, ν_D
293	8	WO_2W out-of-plane vibration, ν_F
235	4	WOW out-of-plane vibration, ν_c

Table 6.1. Raman shift recorded in KGdW and the variation in this shift recorded for crystals with other lanthanides in place of Gd [9] together with the associated bond vibration [7].

6.4 Yb:KGdW Micro-spectroscopy

6.4.1 Analysed Structures

Two different Yb:KGdW structures were chosen to be mapped. The first of these was the structure written with 408 nJ pulse energy in the positive direction with a 20 μm scan separation. As described in section 5.4.1.2, this structure resulted in two guiding regions for polarisation ***E*||*a*** – between the filaments but above and below the cracked region, where the best lasing was from the waveguide illustrated in fig. 6.3 (a). Figure 6 is flipped vertically when compared to the same image shown in fig. 5.6 (d), to correspond to the orientation of the results presented later in this chapter. With polarisation along the crystallographic ***b*** axis guiding occurred to the left and right side (fig. 6.3 (b, d)) of the structure, and also somewhat down the central region, but this was of course hindered by the cracked region (fig. 6.3 (c)). These waveguides were not able to lase with the available pump power using ***E*||*b***.

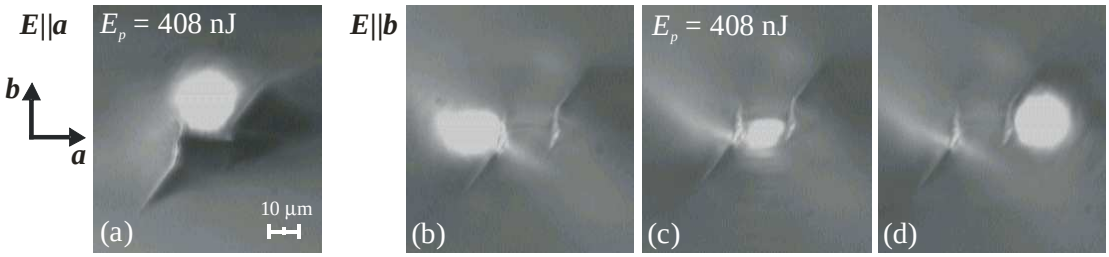

Fig. 6.3. Guiding images in Yb:KGdW, for the structure written with 408 nJ pulse energy and with a 20 μm scan separation. Polarisation along the ***a*** axis gave guiding above the cracked region, while polarisation along the ***b*** axis gave guiding to the left, right and in the central region of the filaments.

The second mapped structure was that written with 369 nJ pulse energy in the positive direction, again with a 20 μm scan separation. This structure gave better performance with ***E*||*b***, creating three waveguides to the left, centre and right of the filaments as shown in fig. 6.4 (a, b, c). Again, the images have been flipped vertically compared to Chapter 5 fig. 5.11 (a, b, c). For the orientation shown in this chapter the right hand waveguide (fig. 6.4 (c)) was found to give the best performance and was able to lase. With polarisation along the crystallographic ***a*** axis only very weak guiding was apparent in upper and lower central regions and no lasing was obtained. The

structures written with pulse energies of 408 nJ and 369 nJ thus present an interesting comparison, as they gave rise to optimum guiding for polarisation along different crystallographic axes.

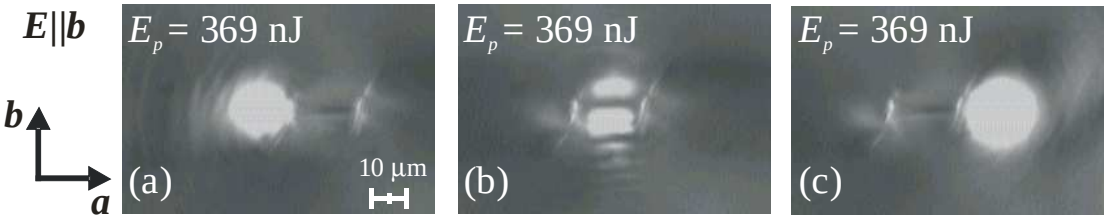

Fig. 6.4. Guiding images in Yb:KGdW, for the structure written with 369 nJ pulse energy and with a 20 µm scan separation. Polarisation along the ***b*** axis gave guiding to the (a) left, (c) right and (b) in the central region of the filaments, where the best performance was observed in the right hand region.

6.4.2 Micro-luminescence Results

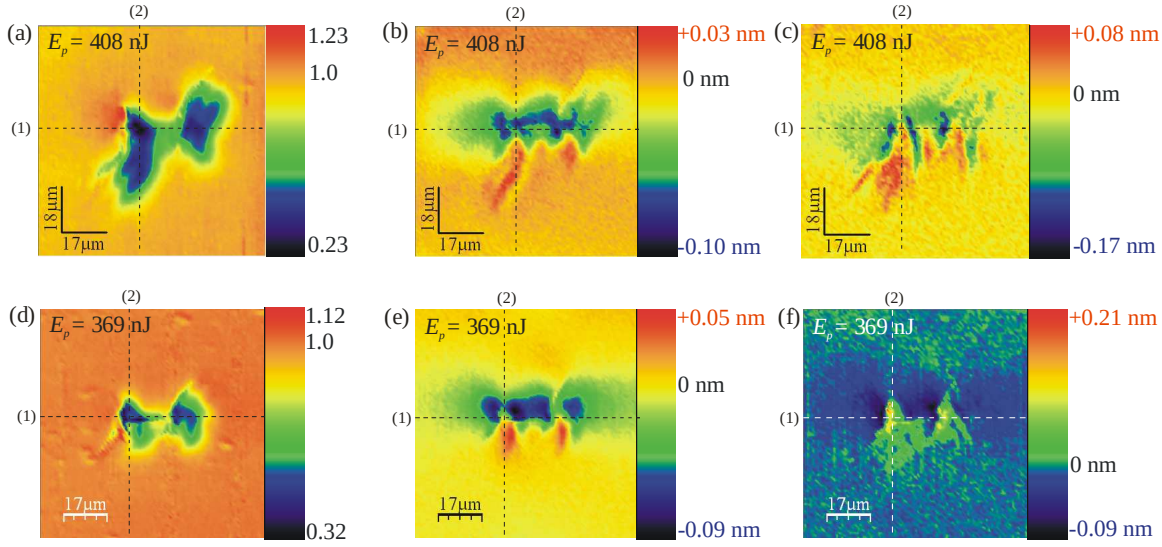

Fig. 6.5. Micro-luminescence maps of the relative change in intensity (a, d), the wavelength shift of the emission peak (b, e) and the change in the peak's width (c, f) for ULI structures written in Yb:KYW with (a, b, c) 408 nJ and (d, e, f) 369 nJ of pulse energy. (1) and (2) correspond to the line scans in fig. 6.6 and 6.7.

The resulting 2D maps for the two KGdW structures are shown in fig. 6.5. There is clearly a drop in intensity at the filaments and also a drop in intensity in the central region, where cracking was shown to have taken place. A blue shift in the emitted peak is evident in regions to the side of each filament, which largely recovers in the

filament itself, and a red shift can be seen in part of the filament. The relationship between stress and shifts in the emission peak of Yb:KGdW are not currently reported in the literature, however, the observed shifts suggest a change in the crystal field which affects the ytterbium ions, and this is a result of distortion of the interatomic lattice spacings. The width of the emitted peak is shown to increase in the filament, and this is a sign of increased disorder of the crystal in these regions [11]. A surprising and interesting observation is that in the surrounding localities the linewidth narrows.

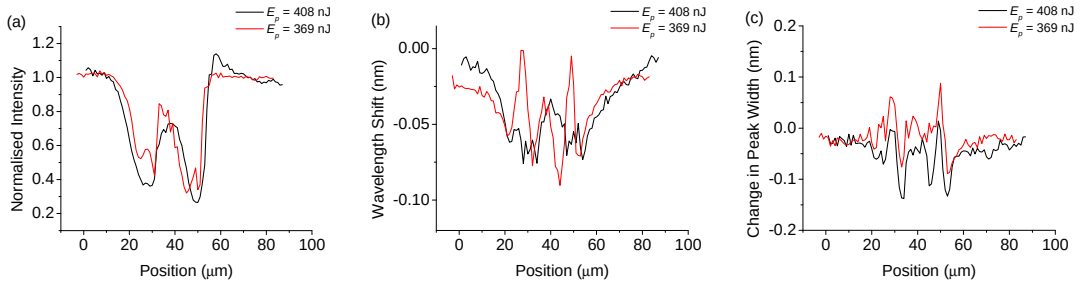

Fig. 6.6. Line scans of intensity variation, peak wavelength shift and peak width variation for line scan 1.

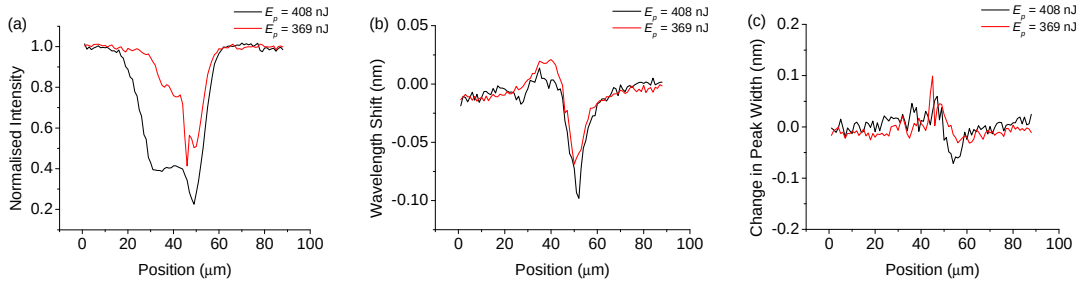

Fig. 6.7. Line scans of intensity variation, peak wavelength shift and peak width variation for line scan 2.

To allow easier comparison between the two structures, line scans are plotted of the lines marked (1) and (2) in fig. 6.5, and these graphs are shown in fig. 6.6 and fig. 6.7. Whilst the shift in the peak's position and width is similar for the two structures, the intensity drop is clearly greater in the structures written with greater energy (408 nJ) and in the vertical direction extends over a greater distance, showing increased structural change in the form of broken bonds, as was also evident from the cracking in these regions.

6.4.3 Micro-Raman Results

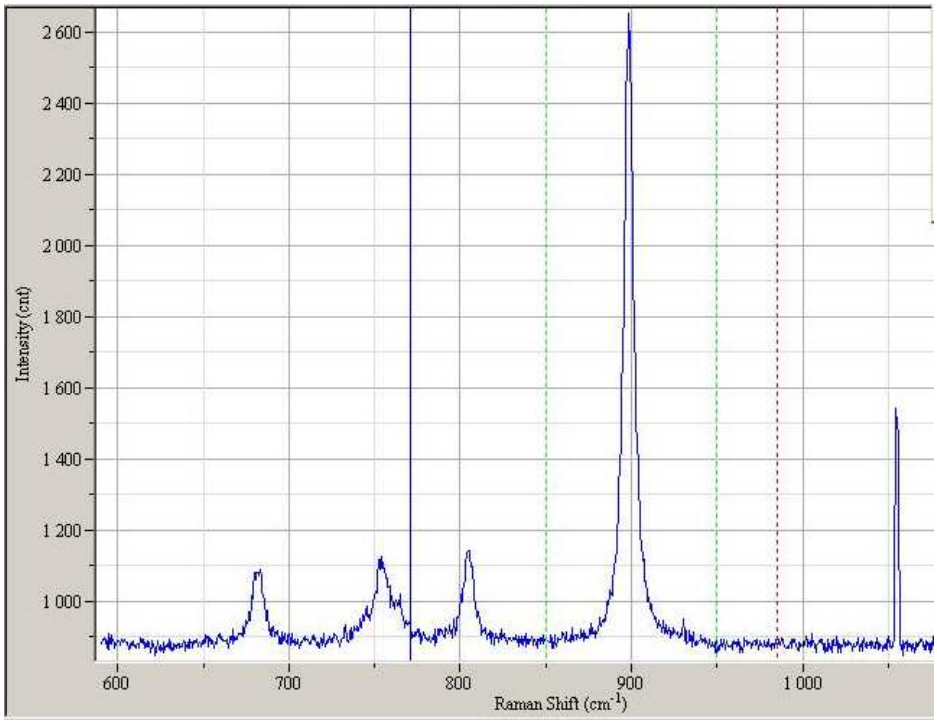

Fig. 6.8. Example of a Raman spectrum measured from a point in Yb:KGdW.

Six Raman peaks were detected and mapped in Yb:KGdW using *LabSpec 5*. These were located at frequency shifts of 682 cm^{-1}, 754 cm^{-1}, 764 cm^{-1}, 805 cm^{-1}, 898 cm^{-1} and 1054 cm^{-1} respectively, and an example of the Raman spectrum is shown in fig. 6.8. These peaks agree well with those reported in the literature [9, 10]. Maps of the recorded change in intensity, Raman shift and peak width of four of these lines are shown in figures 6.9-6.12. From fig. 6.8 it is clear the 764 cm^{-1} line is fairly weak and overlaps with the 754 cm^{-1} shift, making it difficult to map, and little modification was seen in the map, and so the results for this line are not included. Although the 1054 cm^{-1} is fairly strong, it is so narrow that it was not possible to accurately place the peak, and thus it was not possible to observe any shift in the peak or width of this line and so again the map of this line is not included below.

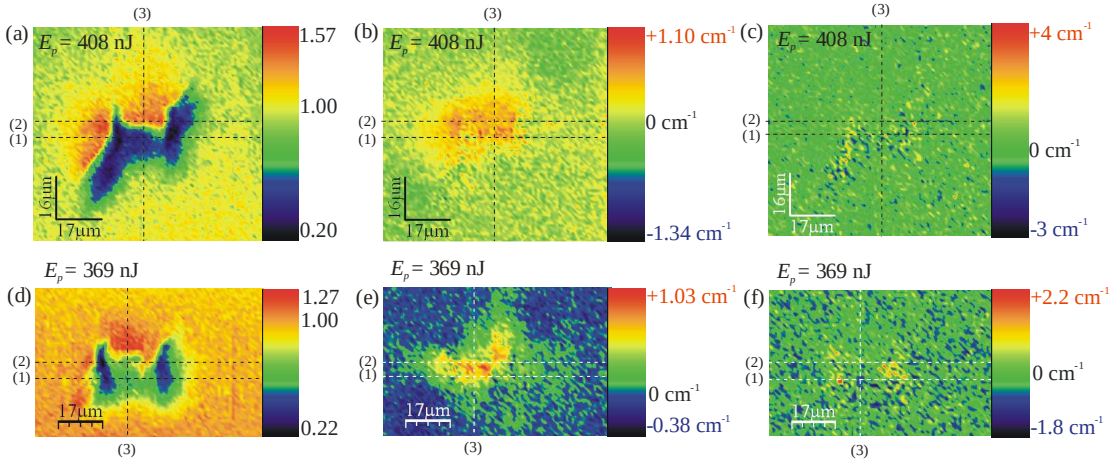

Fig. 6.9. Changes to the 682 cm^{-1} Raman shift peak's intensity (a, d), peak frequency shift (b, e), and peak width (c, f) for structures written at (a, b, c) 408 nJ of pulse energy , (d, e, f) 369 nJ pulse energy.

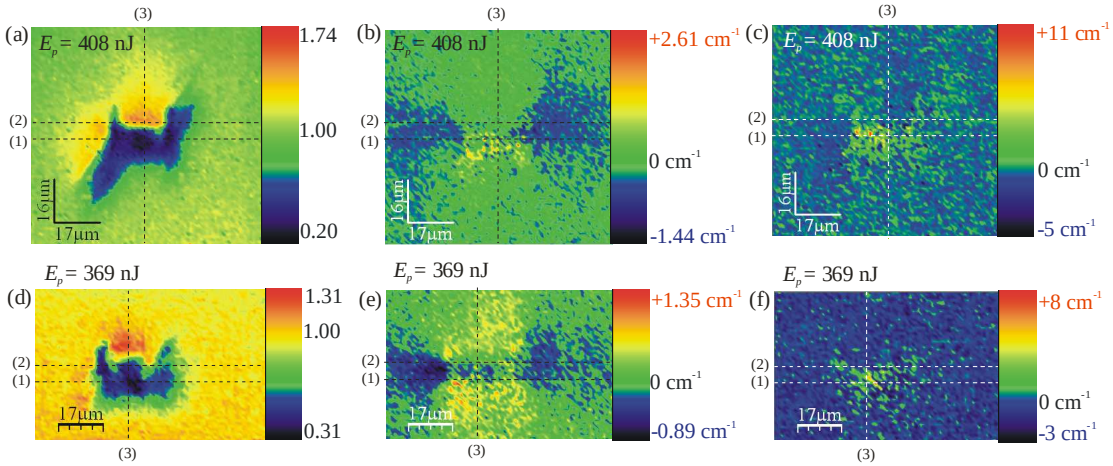

Fig. 6.10. Changes to the 754 cm^{-1} Raman shift peak's intensity (a, d), peak frequency shift (b, e), and peak width (c, f) for structures written at (a, b, c) 408 nJ of pulse energy, (d, e, f) 369 nJ pulse energy.

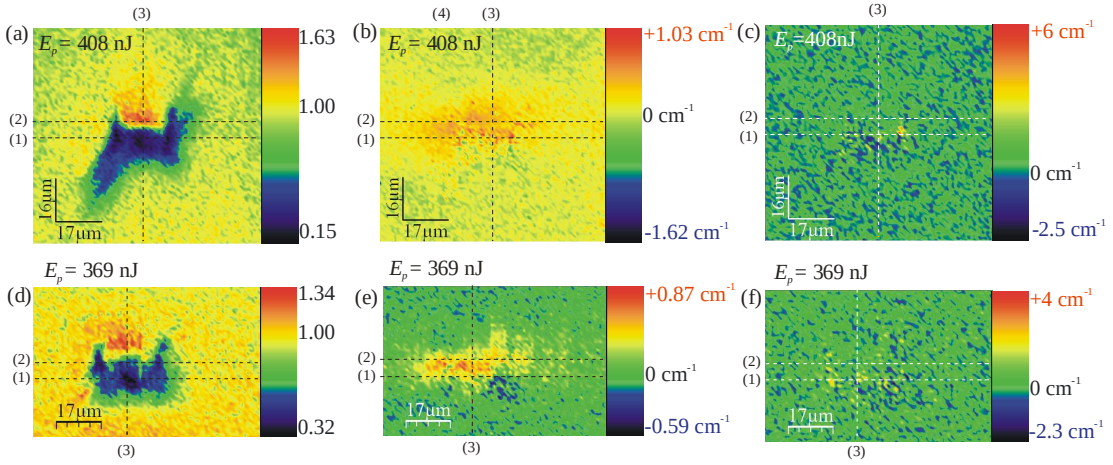

Fig. 6.11. Changes to the 805 cm^{-1} Raman shift peak's intensity (a, d), peak frequency shift (b, e), and peak width (c, f) for structures written at (a, b, c) 408 nJ of pulse energy, (d, e, f) 369 nJ pulse energy.

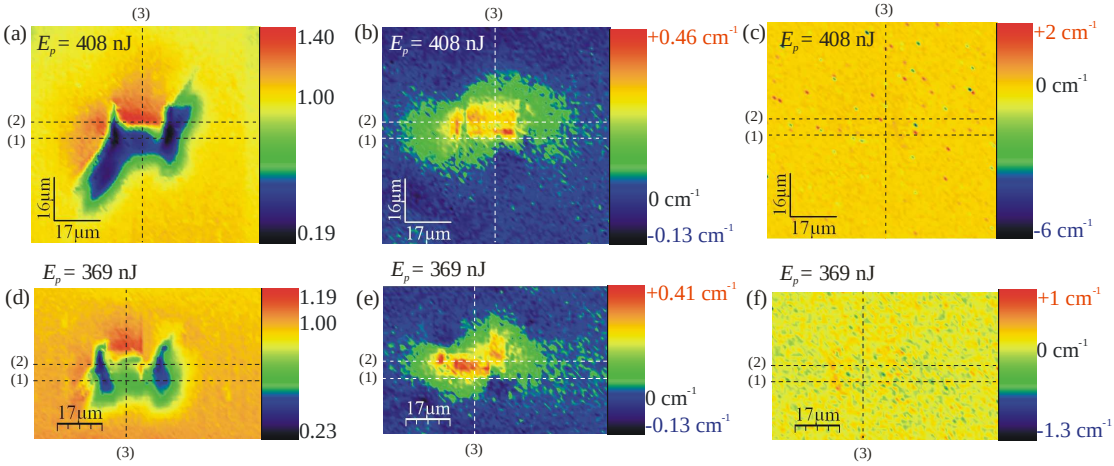

Fig. 6.12. Changes to the 898 cm^{-1} Raman shift peak's intensity (a, d), peak frequency shift (b, e), and peak width (c, f) for structures written at (a, b, c) 408 nJ of pulse energy, (d, e, f) 369 nJ pulse energy.

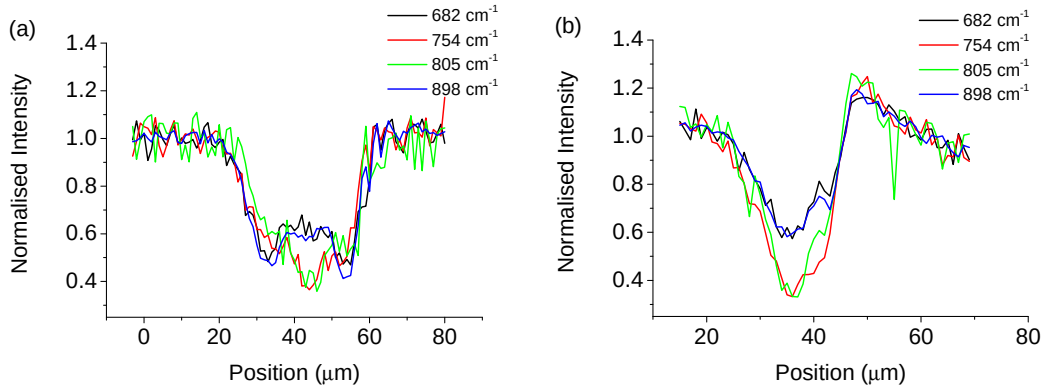

Fig. 6.13. (a) shows the line scan of position (1) for the intensity of various Raman lines, where lines 682 cm^{-1} and 898 cm^{-1} can be coupled together and differentiated from the 754 cm^{-1} and 805 cm^{-1} lines. (b) shows the line scans of the same Raman lines for the position marked (3), emphasising the greater intensity drop experienced in the 754 cm^{-1} and 805 cm^{-1} lines. (a, b) both only show scans for the structure written with a 369 nJ pulse energy.

Whilst the intensity plots of the other peaks appear somewhat similar from the 2D maps, closer inspection at the line scans (shown in fig. 6.13 (a, b)) reveal that the 682 cm^{-1} and 898 cm^{-1} lines show slightly different behaviour to the 754 cm^{-1} and 805 cm^{-1} lines. Even although all peaks show a significant reduction in intensity at the filaments, the 682 cm^{-1} and 898 cm^{-1} peaks show a slight recovery in the space between the two filaments whilst the intensity continues to reduce in the central region for the 754 cm^{-1} and 805 cm^{-1}. This suggests that while all WO_2W vibrations relating to these lines are affected in the filament itself, the mode responsible for the 754 cm^{-1} and 805 cm^{-1} Raman shifts undergo greater damage in the central cracked

region. Comparing the same Raman peak but for structures written at different pulse energies showed the same overall tendency to crack in the filaments and central region, but with greater damage observed in the structure written with higher pulse energy (fig. 6.14).

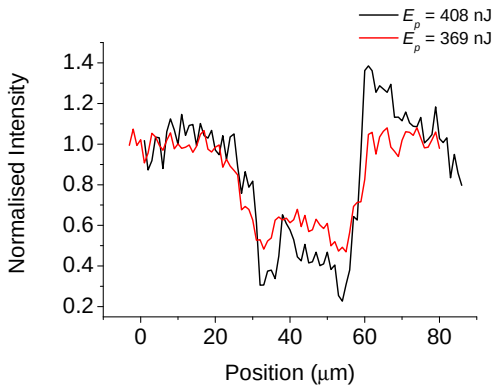

Fig. 6.14. This graph shows a comparison between the structures written at two different pulse energies for the 682 cm^{-1} line. These both show the same curve shape, but with a greater drop in intensity, implying a stronger effect, for the structure written at a higher pulse energy (408 nJ).

By considering the maps of the Raman peak shift ((b) and (e) in figures 6.9-6.12) a pattern can clearly be seen. The 682 cm^{-1} and 898 cm^{-1} lines have a very pronounced shifts towards larger vibration energies in their peaks' position in areas largely to the upper side of the cracked region, overlapping significantly with the guiding region for $\boldsymbol{E||a}$ (fig. 6.3 (a)). Line scans of this shift are presented in fig. 6.15. On the contrary, the 754 cm^{-1} line shows a large shift to higher vibrational energies in the cracked region, but only a very small shift towards higher energies in the regions above and below this, with instead a more pronounced shift to lower energies in the left and right hand regions (fig. 6.10 (b, e)), which correspond to guiding regions for $\boldsymbol{E||b}$ (fig. 6.3 (b, d) and fig. 6.4 (a, c)). Similar shifts in the ~760 cm^{-1} and ~900 cm^{-1} modes were previously reported in KGdW guiding regions for $\boldsymbol{E||N_p}$ and $\boldsymbol{E||N_g}$ polarisations [12]. The map of the 805 cm^{-1} line shows a small increase both above the cracked regions and to the left and right of the filaments but this is not clearly distinguishable from the noise level. These observations imply that the changes to the 682 cm^{-1} and 898 cm^{-1} lines contribute most significantly to $\boldsymbol{E||a}$ guiding, whilst the 754 cm^{-1} Raman shift plays a greater role in $\boldsymbol{E||b}$ guiding regions. At first sight the 754 cm^{-1} lower energy shift seems incongruous with the higher energy shift of the 682 cm^{-1} and 898 cm^{-1}

lines, but elsewhere it is reported that the ~765 cm^{-1} line experiences a shift towards lower energies upon substitution of heavier lanthanides into the KLnW lattice in contrast to the ~900 cm^{-1}, ~805 cm^{-1} and ~685 cm^{-1} lines, which all experience a shift towards higher energies [9]. This explains why a reduced energy shift indicates a densification of the WO_2W matrix, leading to an increased refractive index and a resulting guiding region, in the 754 cm^{-1} line, whilst a larger energy shift is indicative of this in all other lines reported.

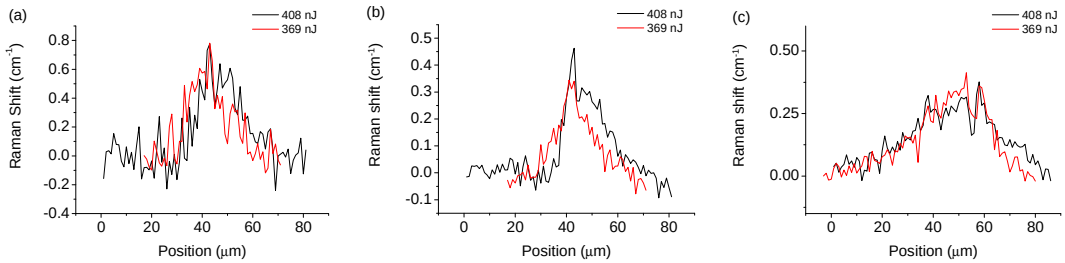

Fig. 6.15. Raman shift for the (a) 682 cm^{-1} and (b) 898 cm^{-1} lines scanned along line (3) as marked in figures 6.9 and 6.12. These show an increased shift in the region above the crack, where optimal guiding for ***E*||*a*** was observed. (c) is a line scan in the horizontal direction for the line marked (2) in fig. 6.12, showing that although the shift in the 898 cm^{-1} peak also continues to the left and right of the filaments it is strongest in the central upper guiding region.

Interestingly, for all Raman lines, very little modification was observed in the width of the line in the filaments. This could imply that, although there is increased damage and increased stress in various regions, there is not a strong increase in the disorder of the crystal, and no amorphisation of the crystal has taken place.

6.5 Yb:KYW Micro-spectroscopy

6.5.1 Analysed Structures

In Yb:KYW it was found that whilst ***E*||*a*** polarisation produced poor guiding, with light polarised along the ***b*** axis there were consistent guiding regions to the left, centre and right of the structure (section 5.4.2) as illustrated in fig. 6.16. The quality of these guiding regions depended strongly on pulse energy where, for a 20 μm scan separation, pulse energies between 355 nJ and 432 nJ resulted in lasing in all left hand

and central guiding regions, with losses between 3.7 dBcm^{-1} and 4.8 dBcm^{-1}. The optimal waveguides were fabricated at pulse energies of 392 nJ or 411 nJ with losses of 3.7 dBcm^{-1} to 3.9 dBcm^{-1}. Therefore the structures which were chosen for mapping were the structure written with 392 nJ pulse energy, giving optimal guiding and lasing results in the left hand region (fig. 6.16 (a)), together with the 20 µm separated scan structure inscribed with 476 nJ of pulse energy, which was written with too much pulse energy to create a low loss waveguide capable of lasing.

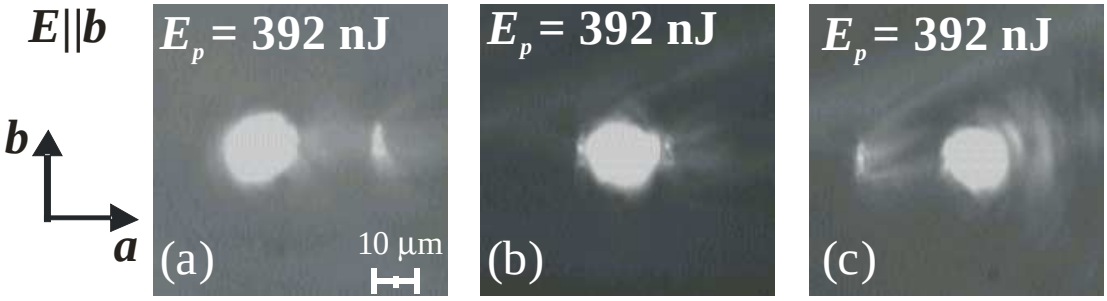

Fig. 6.16. Guiding regions in Yb:KYW with ***E*||*a***.

6.5.2 Micro-luminescence Results

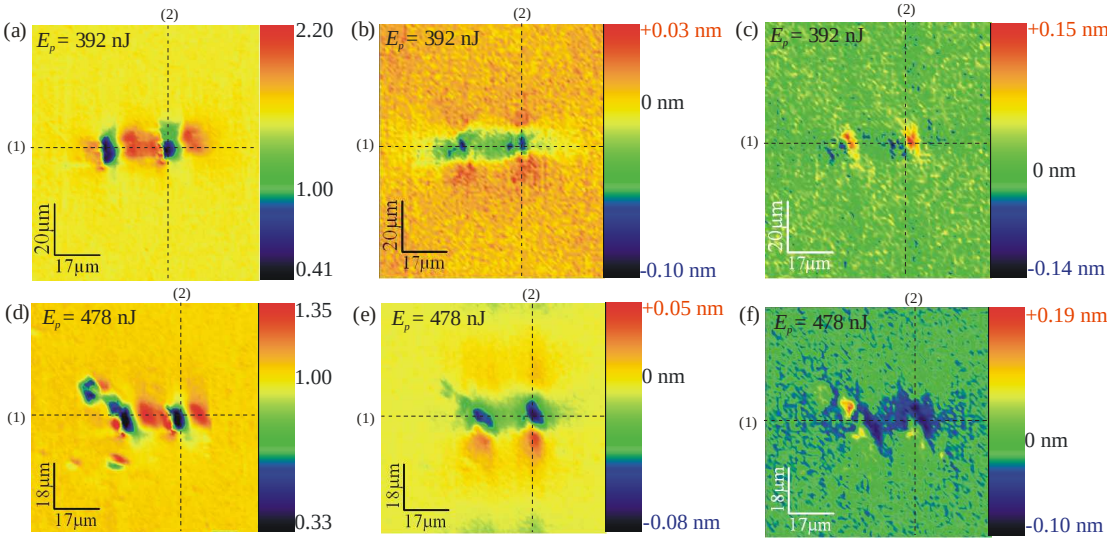

Fig. 6.17. Micro-luminescence maps of the relative change in intensity (a, d), the wavelength shift of the emission peak (b, e) and the change in the peak's width (c, f) for ULI structures in Yb:KYW written with (a, b, c) 392 nJ and (d, e, f) 478 nJ of pulse energy. (1) and (2) correspond to the line scans in figures 6.18 and 6.19.

Maps of the micro-luminescence of the two waveguides are shown in fig. 6.17. The decrease in luminescence intensity at the filaments clearly shows the damage to the crystal in this region, quenching the luminescence and reducing the refractive index with respect to the bulk. In the surrounding region, where guiding occurred, there is an increase in the luminescence. Although this could be explained by an increased Yb^{3+} concentration in this region, leading to a higher refractive index, more probably it is merely an optical effect where the waveguide results in a stronger signal being detected. Horizontal and vertical line scans of the intensity variations of the two structures, corresponding to lines (1) and (2) in the images shown in fig. 6.17, are shown in fig. 6.18. This does not show any difference between the two structures written at different pulse energy, suggesting the extent of the damage is similar in each case.

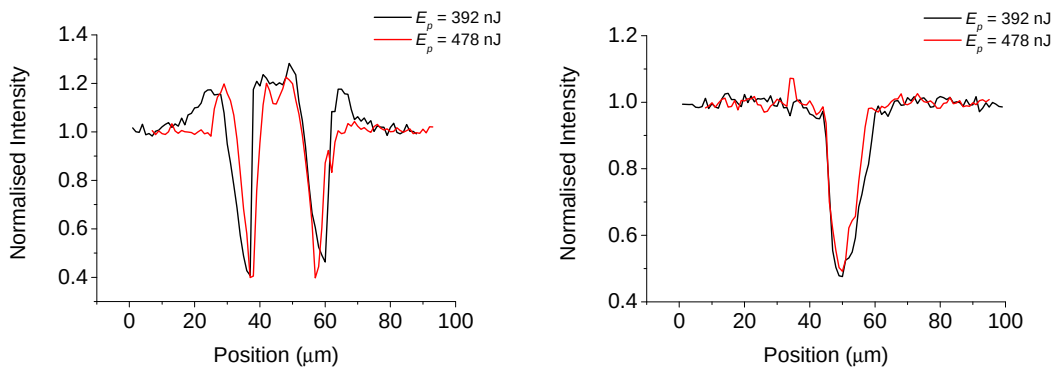

Fig. 6.18. Intensity reduction at the filaments for the (a) horizontal and (b) vertical line scans marked as (1) and (2) in fig. 6.17.

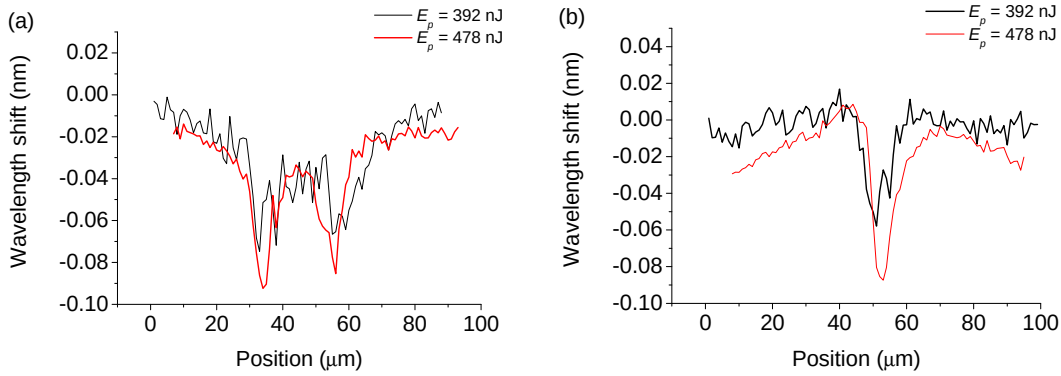

Fig. 6.19. Peak shifts in and around the filaments for the (a) horizontal and (b) vertical line scans marked as (1) and (b) in fig. 6.16. The shift in the filament is greater for the structure inscribed at a higher writing energy (478 nJ).

More information can be gleaned from the shift in the emission peak. In the filaments there is clearly a blue shift in the emission peak, and this peak extends out from the filament and into the guiding regions. As with Yb:KGdW (section 6.4.2), there is currently no literature reporting the relationship between shifts in the emission peaks and stress in Yb:KYW. However, it is possible that this indicates compression of the lattice in the blue-shifted regions, leading to an increased refractive index, explaining why guiding occurs in the central region, and on either side of the two filaments. Guiding cannot occur in the filament itself due to the damage there and the resulting lower refractive index in the voxel. The line scans of the peak shift along line (1) and (2) shown in fig. 6.19 show that both structures give rise to a similar trend, but the blue shift is apparently greater for the structure written with a larger pulse energy (478 nJ). When considering the change to the width of the emission peak it is clear there are modifications in the filaments, but these are not very significant above the background noise.

6.5.3 Micro-Raman Results

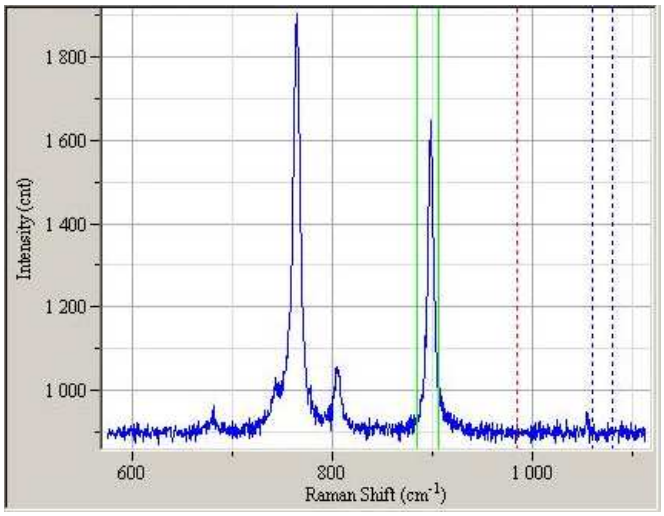

Fig. 6.20. Example of a Raman spectrum measured from a point in Yb:KYW.

Three Raman peaks were detected and mapped in Yb:KYW using *LabSpec 5*, with Stokes shifts of 764 cm^{-1}, 805 cm^{-1}, 898 cm^{-1} respectively as shown in fig. 6.20, corresponding well with those reported in the literature. Maps of the recorded change in intensity, Raman shift and peak width of these lines are shown in figures 6.21-6.23.

The drop in intensity of these peaks is clearly evident in the filament, but does not protrude into the central region, as had been the case in Yb:KGdW. This corresponds to the absence of cracking down the central region in Yb:KYW when compared to Yb:KGdW. The intensity reduction at the filament is similar for all Raman shifts as shown in fig. 6.24 (a), but the structure written with 478 nJ shows a greater drop in intensity when compared to the structure written with 392 nJ pulse energy (fig. 6.24 (b)), corresponding to greater damage in the filament at higher pulse energies.

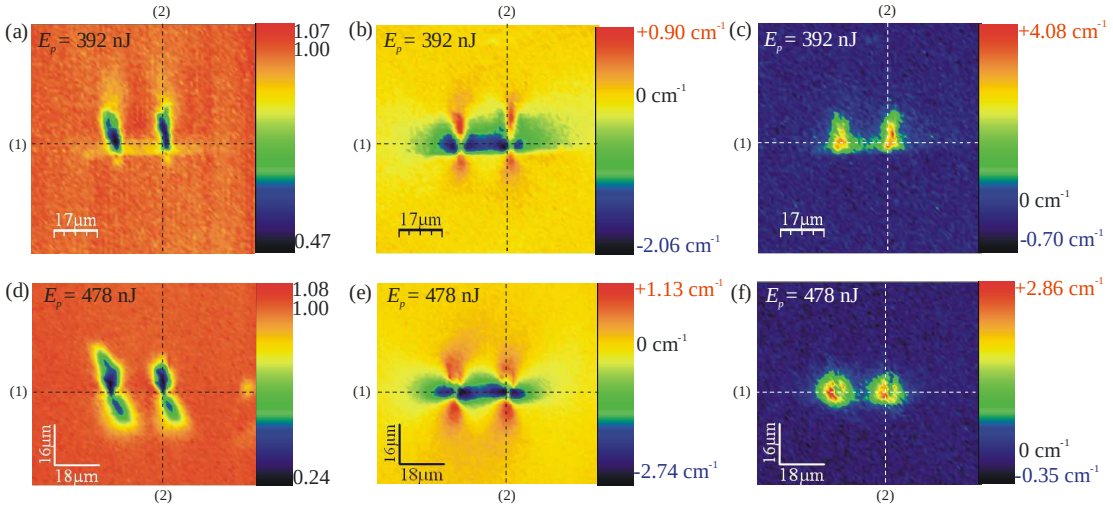

Fig. 6.21. Changes to the 764 cm^{-1} Raman shift peak's intensity (a, d), frequency shift (b, e), and width (c, f) for structures written in Yb:KYW with (a, b, c) 392 nJ of pulse energy or (d, e, f) 478 nJ pulse energy.

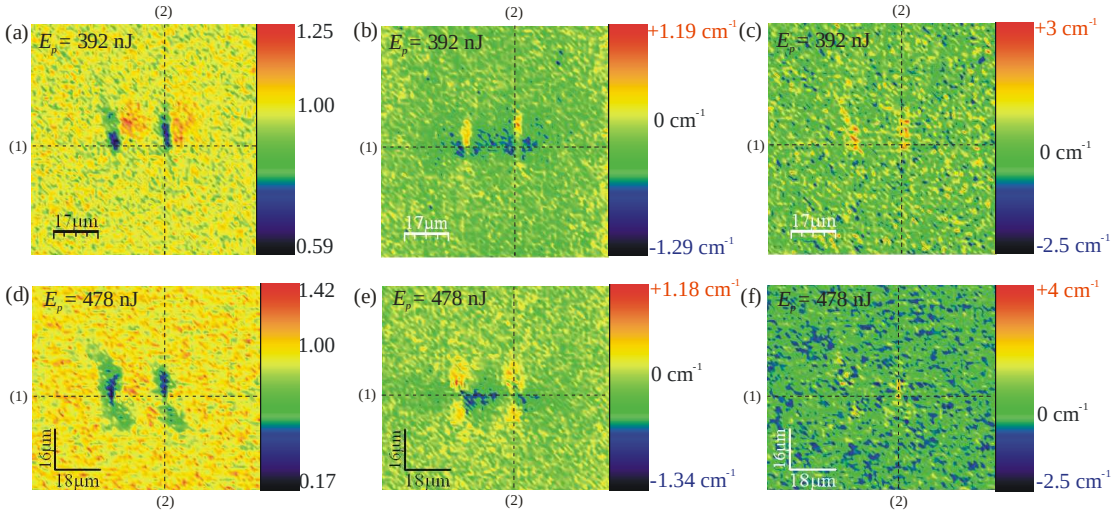

Fig. 6.22. Changes to the 805 cm^{-1} Raman shift peak's intensity (a, d), frequency shift (b, e), and width (c, f) for structures written in Yb:KYW with (a, b, c) 392 nJ of pulse energy or (d, e, f) 478 nJ pulse energy.

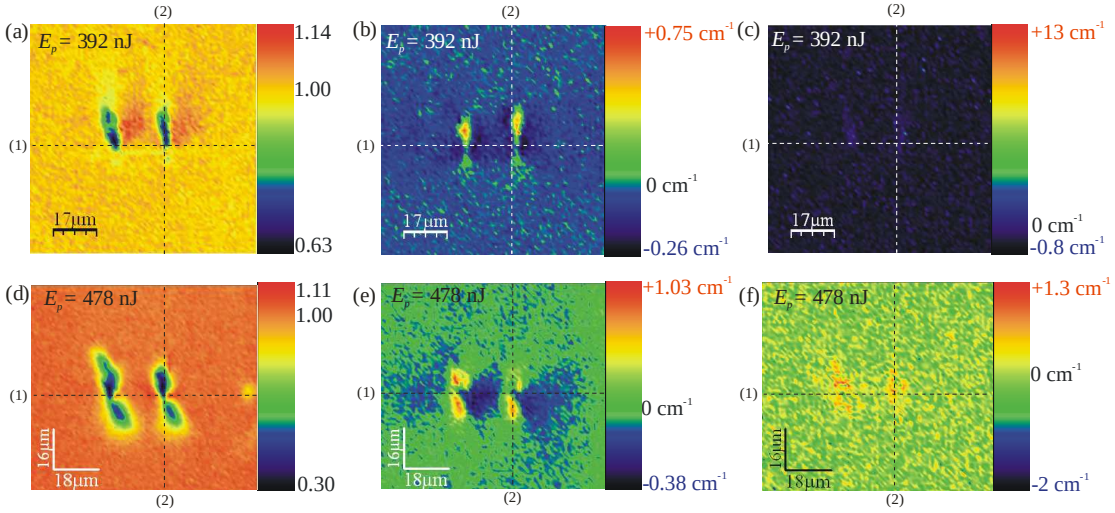

Fig. 6.23. Changes to the 898 cm^{-1} Raman shift peak's intensity (a, d), frequency shift (b, e), and width (c, f) for structures written in Yb:KYW with (a, b, c) 392 nJ of pulse energy or (d, e, f) 478 nJ pulse energy.

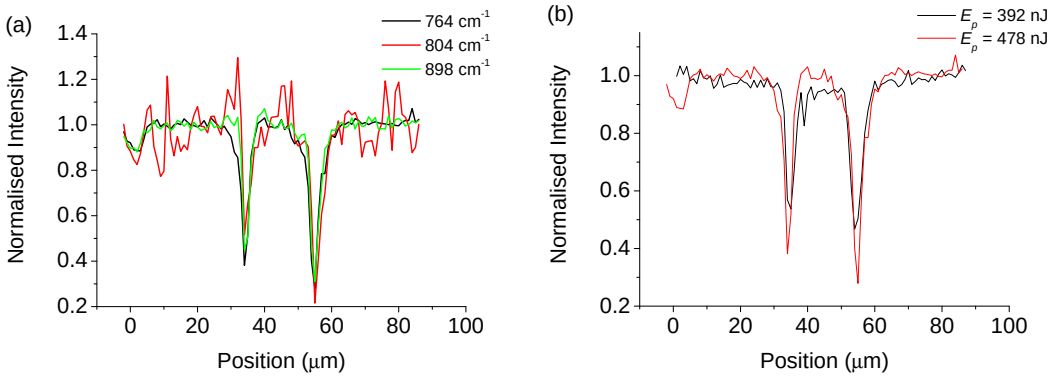

Fig. 6.24. (a) shows the reduction in intensity at the filament in Yb:KYW, where a similar reduction is seen in all Raman lines. (b) shows that the reduction is greater in the structure written with 478 nJ pulse energy, suggesting the structural modification is greater at larger writing energies.

On inspection of the Raman peak shift in and around the structures, whilst all structures show a similar trend, it is clear that the most pronounced shift occurs in the 764 cm^{-1} line (fig. 6.25 (a)). The regions to the sides of the filament show a clear reduced energy shift, which overlap with the ***E*||*b*** guiding regions (fig. 6.16), analogous to the 754 cm^{-1} peak in Yb:KGdW (fig. 6.10). Again this suggests a densification of the WO_2W in-plane lattice leading to an increased refractive index in this region. This shift returns to the bulk Raman line in the centre of the filament, and is seen to experience higher energy shifts in the upper and lower parts of the filament,

indicative of decreased stability of the WO_2W bridge in this region [9]. A line scan of the 764 cm^{-1} Raman shift for the two different structures is shown in fig. 6.25 (b). This shows the peak's shift is greater at higher writing pulse energies, suggesting increased stress for increased writing powers. An interesting feature, however, is that the extent of the shift is similar for both pulse energies. This agrees with the observation that, whilst the loss depended on the writing energy, the mode size was independent from the writing energy with guiding mode diameters consistently found to be around 12 μm (see section 5.4.2.2).

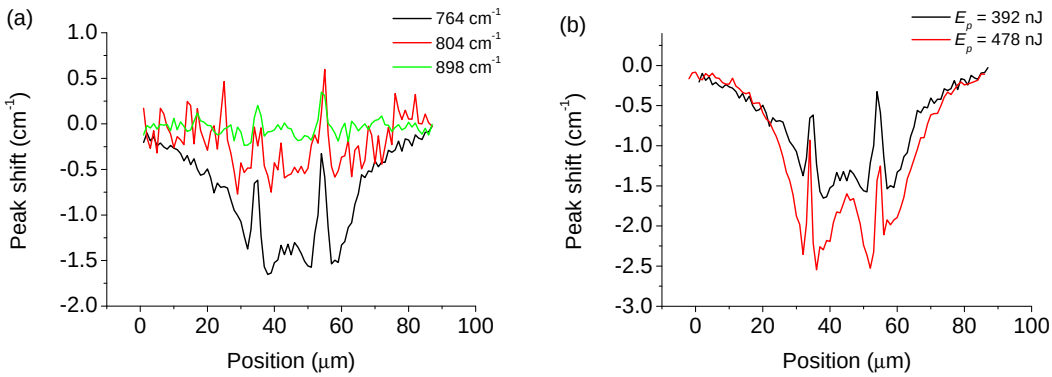

Fig. 6.25. (a) Peak shift for various Raman lines in Yb:KYW, where 764 cm^{-1} clearly shows the greatest energy shift. (b) Peak shift of the 764 cm^{-1} Raman line in Yb:KYW for structures written with pulse energies of 392 nJ and 478 nJ. The peak shift is clearly stronger for higher pulse energies, but extends the same distance from the filaments regardless of pulse energy.

The width of the Raman mode peak clearly increases in the filament for all Raman modes but again is more pronounced for the 764 cm^{-1} line. This increased line width is indicative of increased disorder in the voxel. For both pulse writing energies the disorder extends outside the filament and encroaches upon the guiding region. This extends slightly further into the side regions for the higher pulse energy, and this could be detrimental to the guiding regions, accounting, together with the variations in peak shift, for the increased loss in structures written at higher energies.

6.6 Conclusions and Future Outlook

In this chapter the micro-scale modifications to the crystal's lattice have been investigated by micro-luminescence and micro-Raman experiments. In all

measurements the intensity of the luminescence or Raman shifts were found to decrease in the filament, and the linewidth of the peak also typically increased. These observations are indicative of the increased damage and disorder in these regions, forming the voxel with a lower density and refractive index compared to the bulk. This leads to the filaments forming lower refractive index barriers to the resulting waveguides. The increased energy shifts in the 898 cm^{-1} and 682 cm^{-1} Raman lines in Yb:KGdW have been attributed to a densification of the WO_2W bridge, which suggests an increased refractive index leading to the observed ***E*||*a*** guiding region. Conversely, the reduced energy shifts observed in the 754 cm^{-1} and 764 cm^{-1} lines in Yb:KYW and Yb:KGdW can also be attributed to a densification in the WO_2W bridge, which has resulted in an increased refractive index which is responsible for the ***E*||*b*** guiding regions. Currently there has been no investigation of the relationship between stress and shifts in Raman and luminescence peaks in Yb:tungstates, and so it has not been possible to quantify the value of induced stress. This would therefore present interesting future work, and could allow the refractive index profiles of these waveguides to mapped using micro-spectroscopy. It is envisioned that this technique could be used to great effect in characterising channel waveguides formed by ULI. The technique could also provide a means for feedback to improve writing techniques by ascertaining the conditions required to create the induced stress necessary for guiding, whilst limiting the resulting damaged regions which are undoubtedly a high source of waveguide loss through scattering.

6.7 References

[1] F. Caccavale, C. Sada, F. Segato and F. Cavuoti, "Secondary ion mass spectrometry and optical characterization of Ti : $LiNbO_3$ optical waveguides," Applied Surface Science **150,** 195-201 (1999).

[2] R. S. Taylor, C. Hnatovsky, E. Simova, D. M. Rayner, M. Mehandale, V. R. Bhardwaj and P. B. Corkum, "Ultra-high resolution index of refraction profiles of femtosecond laser modified silica structures," Optics Express **11,** 775-781 (2003).

[3] T. Gorelik, M. Will, S. Nolte, A. Tuennermann and U. Glatzel, "Transmission electron microscopy studies of femtosecond laser induced modifications in quartz," Applied Physics A-Materials Science & Processing **76,** 309-311 (2003).

[4] V. Dierolf and C. Sandmann, "Confocal two photon emission microscopy: A new approach to waveguide imaging," Journal of Luminescence **102,** 201-205 (2003).

[5] Y. Zhang, L. Guilbert and P. Bourson, "Characterization of Ti : $LiNbO_3$ waveguides by micro-Raman and luminescence spectroscopy," Applied Physics B-Lasers and Optics **78,** 355-361 (2004).

[6] I. Horcas, R. Fernández, J. M. Gómez-Rodríguez, J. Colchero, J. Gómez-Herrero and A. M. Baro, "WSXM: A software for scanning probe microscopy and a tool for nanotechnology," Review of Scientific Instruments **78,** 013705 (2007).

[7] L. Macalik, J. Hanuza and A. A. Kaminskii, "Polarized Raman spectra of the oriented $NaY(WO_4)_2$ and $KY(WO_4)_2$ single crystals," Journal of Molecular Structure **555,** 289-297 (2000).

[8] M. C. Pujol, R. Solé, J. Massons, J. Gavaldà, X. Solans, C. Zaldo, F. Díaz and M. Aguiló, "Structural study of monoclinic $KGd(WO_4)_2$ and effects of lanthanide substitution," Journal of Applied Crystallography **34,** 1-6 (2001).

[9] J. Hanuza and L. Macalik, "Polarized Infra-red and Raman Spectra of Monoclinic α-$KLn(WO_4)_2$ Single Crystals (Ln = Sm-Lu, Y)," Spectrochimica Acta Part A-Molecular and Biomolecular Spectroscopy **43,** 361-373 (1987).

[10] M. C. Pujol, M. A. Bursukova, F. Güell, X. Mateos, R. Solé, J. Gavaldà, M. Aguiló, J. Massons, F. Díaz, P. Klopp, U. Griebner and V. Petrov, "Growth, optical characterization, and laser operation of a stoichiometric crystal $KYb(WO_4)_2$," Physical Review B **65,** 165121 (2002).

[11] A. Ródenas, G. A. Torchia, G. Lifante, E. Cantelar, J. Lamela, F. Jaque, L. Roso and D. Jaque, "Refractive index change mechanisms in femtosecond laser written ceramic Nd:YAG waveguides: micro-spectroscopy experiments and beam propagation calculations," Applied Physics B-Lasers and Optics **95,** 85-96 (2009).

[12] S. M. Eaton, C. A. Merchant, R. Iyer, A. J. Zilkie, A. S. Helmy, J. S. Aitchison, P. R. Herman, D. Kraemer, R. J. D. Miller, C. Hnatovsky and R. S. Taylor, "Raman gain from waveguides inscribed in $KGd(WO_4)_2$ by high repetition rate femtosecond laser," Applied Physics Letters **92,** 81105-81107 (2008).

Chapter 7
Conclusions

7.1 Thesis Summary

This thesis has reported the development of monolithic waveguide lasers around 1 μm based on Yb:tungstate crystals. These crystals were chosen due to their excellent spectroscopic properties which include [1]:

- high absorption and emission cross-sections, suitable for short crystal lengths
- strong absorption at 980 nm, making the crystals suitable for diode pumping
- simple two-level electronic structure of the ytterbium ion which reduces detrimental processes such as excited state absorption, up-conversion, cross relaxation and concentration quenching
- a small Stokes shift resulting in high laser slope efficiencies
- broad emission bandwidths suitable for ultrashort pulse generation.

As a precursor to the waveguide theme a novel QD-SESAM was investigated in a bulk cavity configuration for its suitability as a mode-locking element in Yb:tungstate lasers. It was found to be a highly suitable device, as pulses as short as 114 fs at 0.5 W were demonstrated in an Yb:KYW cavity, and a higher average output power of 1.15 W was observed with 200 fs pulses. The excellent performance was attributed to low non-saturable losses of 0.2 % and low saturation fluence of 25 μJcm^{-2}, together with very fast relaxation times, surpassing the performance of QW-SESAMs [2]. This highlighted the advantages of using QD materials as saturable absorbers and led onto the inscription of channel waveguides in a QD-doped glass using ULI [3]. The losses at 1.5 μm were determined to be 2.9 $dBcm^{-1}$, and the absorption in the waveguide region was found to be reduced compared to the bulk, indicative of modification to the QDs within the written volume. The exact nature of this modification requires further investigation. Nevertheless this has been an important first step towards the

creation of waveguide saturable absorbers for future integration with channel waveguide lasers to form fully integrated ultrafast waveguide-based devices.

A planar waveguide with an active Yb:KYW guiding layer was grown by LPE with losses of less than 0.1 $dBcm^{-1}$. This waveguide was the first demonstration of lasing from Yb:KYW in a monolithic cavity configuration [4]. Using surface tension provided by fluorinert liquid, a mirror and output coupler were held against the crystal end-facets. Using a 4.1 % output coupler a maximum output power of 148 mW was observed with 62 % slope efficiency at 1039 nm. A higher output power of 190 mW with a 76 % slope efficiency was obtained with a bulk 10% output coupler, held to the crystal facet using a mirror mount. These output powers and slope efficiencies are comparable with results from more typical z-fold cavity configurations using bulk Yb:KYW crystals, but from devices with a much smaller footprint. With 1 % output coupling a threshold of 40 mW absorbed pump power was observed. This is the lowest threshold reported in an Yb:KYW laser. This result shows the advantages of waveguide lasers over their bulk counterparts, offering comparable output powers and slope efficiencies but with the additional advantages of compact geometries and reduced lasing thresholds.

Replacing the output coupler with an OC-SESAM, *Q*-switching was demonstrated. Pulse durations were as short as 170 ns with up to 33 mW average output powers at repetition rates exceeding 700 kHz. The maximum pulse energy was found to be 44 nJ. The advantage of partially unstable cavities in offering optimal output coupling was then demonstrated as the average output power from the same *Q*-switched laser increased to over 90 mW in such a geometry. The repetition rate and pulse duration of this laser remained similar to the stable cavity performance, but the increased average power led to a pulse energy of 140 nJ. Although unstable cavities are known to be able to improve beam quality from a laser, in this case the beam performance along the unguided direction remained poor. This was attributed to the low magnification in a plane-plane cavity which does not lead to transverse mode discrimination and therefore does not produce a good far-field beam pattern. In a monolithic cavity the best option for high beam quality is to use a channel waveguide, and this was the next topic which was investigated.

Channel waveguides were fabricated in Yb:KGdW and Yb:KYW using ULI [5]. This was the first example of ULI waveguides fabricated in Yb:KGdW. These channel waveguides were also used to build monolithic lasers, where in Yb:KGdW four waveguides were found to lase and in Yb:KYW sixteen lasing structures were identified. Interestingly, guiding regions were found to be polarisation dependent. In Yb:KGdW, ***E***||***b*** gave rise to guiding in left, central and right hand regions where optimal guiding was found in structures written with 369 nJ – 389 nJ of pulse energy and a 20 μm scan separation. Lasing powers were as high as 11.2 mW at 1036 nm and propagation losses were found to be 2.9 dBcm^{-1}. With ***E***||***a*** guiding was observed in upper and lower regions, where the optimal structure was written at 408 nJ pulse energy and a 20 μm scan separation, which had produced a cracked region between the two filaments. The best lasing performance was obtained with this structure, where 18.6 mW was achieved with a 9.3% slope efficiency using a 5 % output coupler. This waveguide lased at 1023 nm and had losses of ~2 dBcm^{-1}. The M^2 of this laser was determined to be 1.5 and 1.2 along the ***a*** and ***b*** axes respectively. The waveguide numerical aperture was used to estimate the refractive index change in the waveguides to be 0.8×10^{-3} in the ***E***||***a*** axis and 1.3×10^{-3} in the ***E***||***b*** axis.

In Yb:KYW ***E***||***a*** only gave poor guiding results, but ***E***||***b*** gave guiding in left, central and right hand regions. Central and left hand regions were consistently found to lase in structures written with a 20 μm scan separation and with pulse energies between 355 nJ and 432 nJ, where pulse energies between 392 nJ and 411 nJ gave optimal results. Output powers were low with 8.2 mW being the maximum demonstrated using a 5 % output coupler, and the losses were found to be greater than 3.7 dBcm^{-1}. The output powers and slope efficiencies were very poor when compared to those reported in the LPE planar waveguide. This was due to the large losses of the channel waveguides. However, the excellent beam quality shows the advantages channel waveguides can offer. By reducing the propagation losses of the channel waveguides excellent power, slope efficiency and beam quality should be achievable. In this work the writing polarisation, pulse energy and scan separation were varied to optimise the waveguide quality. By optimising other writing parameters it is anticipated that losses can be reduced even further.

Finally micro-spectroscopy measurements were performed on the channel waveguides in order to identify some of the structural changes that had resulted in the guiding behaviour. Micro-luminescence and micro-Raman maps of both lasing and non-lasing structures were taken. It was found that in all structures the intensity of both the luminescence and Raman peaks dropped at the written filament, suggesting increased damage and disorder in these regions, in agreement with the crystal damage which could be observed in end-facet images. This resulted in a lower material density in the filaments with reduced refractive index, forming an effective boundary for the waveguides. Higher writing pulse energies led to greater drops in intensity in the filaments, signifying increased damage, which was expected with greater writing energy. The most significant observations were changes to the energy shifts seen in several of the Raman lines in guiding regions. In Yb:KGdW the higher energy shift in the 898 cm^{-1} and 682 cm^{-1} lines were attributed to a densification of the WO_2W bridge, which increased the refractive index in these regions and explained the observed $\boldsymbol{E}||\boldsymbol{a}$ guiding regions. In the 754 cm^{-1} and 764 cm^{-1} Raman lines a lower energy shift is characteristic of densification of the WO_2W bridge in the lattice, which again resulted in an increased refractive index in these regions, which supported guiding in both Yb:KGdW and Yb:KYW along the crystallographic $\boldsymbol{b}$ axis. This technique has therefore been shown to be able to identify not only guiding regions, but also the nature of the crystal modification which has resulted in the waveguides.

This thesis has therefore presented a variety of work which has resulted in the demonstration of monolithic waveguide lasers in Yb:tungstates, and also a method for characterising the fabricated waveguides. Excellent output power and slope efficiencies were demonstrated in LPE-grown planar waveguides, and excellent beam qualities were demonstrated in channel waveguide fabricated by ULI. QD-SESAMs were also characterised to be highly suitable mode-locking elements in Yb:tungstate cavities. Future work will of course build on this to combine the excellent performance from each result into a single device.

7.2 Future Work

It is clear that this work has resulted in many novel and interesting results, but of course there is always scope for further experiments and development of the laser systems. QD saturable absorbers have been identified as suitable elements for mode locking Yb:tungstate lasers, and initial work has been done to fabricate waveguides in a QD-doped glass. Currently the non-linear absorption characteristics of the waveguides have not been measured, and so this is an obvious extension of this work. There are plans to build a pump-probe set-up at Heriot Watt University to allow the non-linear characterisation of these waveguides. This would provide information on the effect that ULI has had on the QDs, and whether the properties which make QDs so interesting have been preserved during this writing process.

LPE has been shown to be an excellent technique for fabricating low-loss planar waveguides, which can give CW performance on par with bulk lasers, but with the added advantages of low thresholds and compact cavities. By reducing the mode size even further lower thresholds could be achieved. This could be accomplished by co-doping the LPE layer with other materials such as gadolinium and lutetium to increase the refractive index contrast, allowing thinner layers to guide 1 μm light. However, to obtain really low thresholds it is not enough to have only one dimensional guiding, but a means of creating low loss channel waveguides must be found. ULI has been investigated as a method to create channel waveguides, showing in particular the advantage of channel waveguides in terms of beam quality. Due to the high losses the performance was not comparable to that of bulk and LPE planar waveguide lasers, and the thresholds were very high. Therefore further work is needed to fabricate higher quality channel waveguides.

This future work will involve further characterisation of fabricated waveguides, so that the induced changes can be better understood, allowing more control of the modification. Further characterisation would involve investigating the relationship between stress in the tungstate lattice and shifts in detected Raman and luminescence peaks. This would allow refractive index profiles to be obtained from

micro-spectroscopic measurements, and would also provide a means of feedback to help improve fabrication.

With regard to fabricating channel waveguides using ULI, the process has been optimised in terms of pulse energy, polarisation and writing direction for a given laser writing system. However, there are many additional parameters which remain to be investigated such as wavefront tilt, writing velocity, focusing optics and writing wavelength, and with a thorough investigation of these the losses could be reduced even further. Interesting work can also arise from using alternative channel fabrication methods. Ideally losses would be as low as those found in the LPE layers. Perhaps one way to begin to achieve such performance would be to start with an LPE planar waveguide and modify it to create a channel waveguide. This could be achieved by a number of methods. One possibility would be to combine LPE and ULI, such that a structure is written outside of the LPE layer, limiting the increased loss which is found to result from this technique, but creating enough refractive index contrast to induce guiding within the LPE layer. Further work is also planned in etching of the crystals to create a channel waveguide. This could either involve directly etching part of the LPE layer, or alternatively etching an overgrown undoped layer to create an effective refractive index change leading to guiding within the LPE layer. Schematics of these techniques are all illustrated in fig. 7.1.

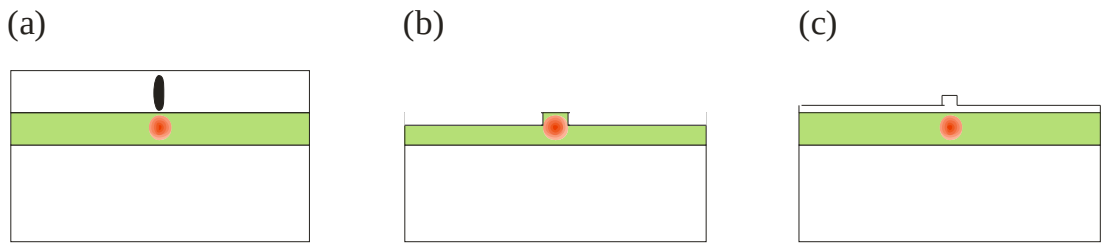

Fig. 7.1. Schematics of schemes for creating channel waveguides in Yb-doped LPE layers (illustrated in green) using (a) ULI in an overgrown layer (b) etching of the doped LPE layer (c) etching of an overgrown layer.

Finally this work shows the potential for ultrashort pulse generation from an Yb:tungstate channel waveguide laser. The limiting factor thus far has been that it has not been possible to simultaneously have excellent output performance in terms of power, as was achieved in the LPE planar waveguide laser, together with excellent

beam quality and small mode size, as was demonstrated in the ULI channel waveguide lasers. Consequently it has not been possible to obtain high enough fluences to saturate the available OC-SESAMs, providing the mechanism of ultrashort pulse generation. However, it was shown that QD-SESAMs have lower saturation fluences than their QW counterparts, and so by integration of QD-SESAMs within Yb:tungstate waveguides ultrafast pulses may be achievable. Additionally, as new fabrication techniques are investigated the propagation losses of the Yb:tungstate channel waveguides are expected to improve, increasing the fluence, enabling device saturation. Therefore the goal of ultrafast and high repetition rate Yb:tungstate waveguide lasers is now well within sight and the results in this thesis, besides being significant in and of themselves, have presented important results in this direction.

7.3 References

[1] W. F. Krupke, "Ytterbium solid-state lasers - The first decade," IEEE Journal of Selected Topics in Quantum Electronics **6,** 1287-1296 (2000).

[2] A. A. Lagatsky, F. M. Bain, C. T. A. Brown, W. Sibbett, D. A. Livshits, G. Erbert and E. U. Rafailov, "Low-loss quantum-dot-based saturable absorber for efficient femtosecond pulse generation," Applied Physics Letters **91,** 231111 (2007).

[3] A. M. Malyarevich, K. V. Yumashev, A. A. Lagatsky, F. M. Bain, C. T. A. Brown, W. Sibbett, R. R. Thomson, A. K. Kar, A. A. Onushchenko, A. A. Zhilin and A. A. Lipovskii, "Optical Waveguides in Glasses Doped with Lead Sulfide Quantum Dots," Physics, Chemistry and Application of Nanostructures**,** 140-143 (2009).

[4] F. M. Bain, A. A. Lagatsky, S. V. Kurilchick, V. E. Kisel, S. A. Guretsky, A. M. Luginets, N. A. Kalanda, I. M. Kolesova, N. V. Kuleshov, W. Sibbett and C. T. A. Brown, "Continuous-wave and Q-switched operation of a compact, diode-pumped Yb^{3+}:$KY(WO_4)_2$ planar waveguide laser," Optics Express **17,** 1666-1670 (2009).

[5] F. M. Bain, A. A. Lagatsky, R. R. Thomson, N. D. Psaila, N. V. Kuleshov, A. K. Kar, W. Sibbett and C. T. A. Brown, "Ultrafast laser inscribed Yb:$KGd(WO_4)_2$ and Yb:$KY(WO_4)_2$ channel waveguide lasers," Optics Express **17,** 22417-22422 (2009).

Appendix A – Tables of Inscribed Waveguides

Ultrafast laser inscription was used to create 168 structures in Yb:KGdW and 176 structures in Yb:KYW. Only results from a selection of the most interesting waveguides are presented in Chapter 5. Here, a full list of all the structures and their writing conditions is presented.

Yb:KGdW Writing Conditions

All structures were written with a 1064 nm Yb:fibre laser producing pulses with a 1.3 ps duration at a 500 kHz repetition rate. Samples were translated transversally along the crystallographic ***c*** axis at 6 mms^{-1}. A Mitutoyo M-PLAN-APO-NIR ×20 objective was used for focussing, which had a numerical aperture of 0.4. The structures were written 430 μm below the crystal's surface. Each structure consisted of two written tracks separated by a distance which is given in the following table. The pulse energy, polarisation and writing direction were also varied, and details of the various writing conditions used are shown below.

Pulse Energy (nJ)	Scan Separation (μm)	Polarisation	Writing Direction (positive or negative)
558	10	***E*||*c***	-
558	10	***E*||*c***	+
558	15	***E*||*c***	-
558	15	***E*||*c***	+
558	20	***E*||*c***	-
558	20	***E*||*c***	+
558	25	***E*||*c***	-
558	25	***E*||*c***	+
503	10	***E*||*c***	-
503	10	***E*||*c***	+
503	15	***E*||*c***	-
503	15	***E*||*c***	+
503	20	***E*||*c***	-
503	20	***E*||*c***	+

Appendix A – Tables of Inscribed Waveguides

Pulse Energy (nJ)	Scan Separation (μm)	Polarisation	Writing Direction (positive or negative)
503	25	$\boldsymbol{E}\|\|\boldsymbol{c}$	-
503	25	$\boldsymbol{E}\|\|\boldsymbol{c}$	+
452	10	$\boldsymbol{E}\|\|\boldsymbol{c}$	-
452	10	$\boldsymbol{E}\|\|\boldsymbol{c}$	+
452	15	$\boldsymbol{E}\|\|\boldsymbol{c}$	-
452	15	$\boldsymbol{E}\|\|\boldsymbol{c}$	+
452	20	$\boldsymbol{E}\|\|\boldsymbol{c}$	-
452	20	$\boldsymbol{E}\|\|\boldsymbol{c}$	+
452	25	$\boldsymbol{E}\|\|\boldsymbol{c}$	-
452	25	$\boldsymbol{E}\|\|\boldsymbol{c}$	+
407	10	$\boldsymbol{E}\|\|\boldsymbol{c}$	-
407	10	$\boldsymbol{E}\|\|\boldsymbol{c}$	+
407	15	$\boldsymbol{E}\|\|\boldsymbol{c}$	-
407	15	$\boldsymbol{E}\|\|\boldsymbol{c}$	+
407	20	$\boldsymbol{E}\|\|\boldsymbol{c}$	-
407	20	$\boldsymbol{E}\|\|\boldsymbol{c}$	+
407	25	$\boldsymbol{E}\|\|\boldsymbol{c}$	-
407	25	$\boldsymbol{E}\|\|\boldsymbol{c}$	+
366	10	$\boldsymbol{E}\|\|\boldsymbol{c}$	-
366	10	$\boldsymbol{E}\|\|\boldsymbol{c}$	+
366	15	$\boldsymbol{E}\|\|\boldsymbol{c}$	-
366	15	$\boldsymbol{E}\|\|\boldsymbol{c}$	+
366	20	$\boldsymbol{E}\|\|\boldsymbol{c}$	-
366	20	$\boldsymbol{E}\|\|\boldsymbol{c}$	+
366	25	$\boldsymbol{E}\|\|\boldsymbol{c}$	-
366	25	$\boldsymbol{E}\|\|\boldsymbol{c}$	+
330	10	$\boldsymbol{E}\|\|\boldsymbol{c}$	-
330	10	$\boldsymbol{E}\|\|\boldsymbol{c}$	+
330	15	$\boldsymbol{E}\|\|\boldsymbol{c}$	-
330	15	$\boldsymbol{E}\|\|\boldsymbol{c}$	+
330	20	$\boldsymbol{E}\|\|\boldsymbol{c}$	-
330	20	$\boldsymbol{E}\|\|\boldsymbol{c}$	+
330	25	$\boldsymbol{E}\|\|\boldsymbol{c}$	-
330	25	$\boldsymbol{E}\|\|\boldsymbol{c}$	+
296	10	$\boldsymbol{E}\|\|\boldsymbol{c}$	-

Pulse Energy (nJ)	Scan Separation (μm)	Polarisation	Writing Direction (positive or negative)
296	10	$\boldsymbol{E}\|\|\boldsymbol{c}$	+
296	15	$\boldsymbol{E}\|\|\boldsymbol{c}$	-
296	15	$\boldsymbol{E}\|\|\boldsymbol{c}$	+
296	20	$\boldsymbol{E}\|\|\boldsymbol{c}$	-
296	20	$\boldsymbol{E}\|\|\boldsymbol{c}$	+
296	25	$\boldsymbol{E}\|\|\boldsymbol{c}$	-
296	25	$\boldsymbol{E}\|\|\boldsymbol{c}$	+
267	10	$\boldsymbol{E}\|\|\boldsymbol{c}$	-
267	10	$\boldsymbol{E}\|\|\boldsymbol{c}$	+
267	15	$\boldsymbol{E}\|\|\boldsymbol{c}$	-
267	15	$\boldsymbol{E}\|\|\boldsymbol{c}$	+
267	20	$\boldsymbol{E}\|\|\boldsymbol{c}$	-
267	20	$\boldsymbol{E}\|\|\boldsymbol{c}$	+
267	25	$\boldsymbol{E}\|\|\boldsymbol{c}$	-
267	25	$\boldsymbol{E}\|\|\boldsymbol{c}$	+
558	10	Circular	-
558	10	Circular	+
558	15	Circular	-
558	15	Circular	+
558	20	Circular	-
558	20	Circular	+
558	25	Circular	-
558	25	Circular	+
503	10	Circular	-
503	10	Circular	+
503	15	Circular	-
503	15	Circular	+
503	20	Circular	-
503	20	Circular	+
503	25	Circular	-
503	25	Circular	+
503	20	Circular	-
503	20	Circular	+
503	25	Circular	-
503	25	Circular	+
503	30	Circular	-

Appendix A – Tables of Inscribed Waveguides

Pulse Energy (nJ)	Scan Separation (μm)	Polarisation	Writing Direction (positive or negative)
503	30	Circular	+
503	35	Circular	-
503	35	Circular	+
478	20	Circular	-
478	20	Circular	+
478	25	Circular	-
478	25	Circular	+
478	30	Circular	-
478	30	Circular	+
478	35	Circular	-
478	35	Circular	+
453	20	Circular	-
453	20	Circular	+
453	25	Circular	-
453	25	Circular	+
453	30	Circular	-
453	30	Circular	+
453	35	Circular	-
453	35	Circular	+
431	20	Circular	-
431	20	Circular	+
431	25	Circular	-
431	25	Circular	+
431	30	Circular	-
431	30	Circular	+
431	35	Circular	-
431	35	Circular	+
408	20	Circular	-
408	20	Circular	+
408	25	Circular	-
408	25	Circular	+
408	30	Circular	-
408	30	Circular	+
408	35	Circular	-
408	35	Circular	+

Pulse Energy (nJ)	Scan Separation (μm)	Polarisation	Writing Direction (positive or negative)
389	20	Circular	-
389	20	Circular	+
389	25	Circular	-
389	25	Circular	+
389	30	Circular	-
389	30	Circular	+
389	35	Circular	-
389	35	Circular	+
369	20	Circular	-
369	20	Circular	+
369	25	Circular	-
369	25	Circular	+
369	30	Circular	-
369	30	Circular	+
369	35	Circular	-
369	35	Circular	+
350	20	Circular	-
350	20	Circular	+
350	25	Circular	-
350	25	Circular	+
350	30	Circular	-
350	30	Circular	+
350	35	Circular	-
350	35	Circular	+
334	20	Circular	-
334	20	Circular	+
334	25	Circular	-
334	25	Circular	+
334	30	Circular	-
334	30	Circular	+
334	35	Circular	-
334	35	Circular	+
316	20	Circular	-
316	20	Circular	+
316	25	Circular	-
316	25	Circular	+

Pulse Energy (nJ)	Scan Separation (μm)	Polarisation	Writing Direction (positive or negative)
316	30	Circular	-
316	30	Circular	+
316	35	Circular	-
316	35	Circular	+
301	20	Circular	-
301	20	Circular	+
301	25	Circular	-
301	25	Circular	+
301	30	Circular	-
301	30	Circular	+
301	35	Circular	-
301	35	Circular	+

Table A.1. Writing conditions used to create channel waveguide in Yb:KGdW.

Yb:KYW Writing Conditions

All structures were written with a 1064 nm Yb:fibre laser producing pulses with a 1.3 ps duration at a 500 kHz repetition rate. Samples were translated transversally along the crystallographic ***c*** axis at 6 mms^{-1}. A Mitutoyo M-PLAN-APO-NIR ×20 objective was used for focussing, which had a numerical aperture of 0.4. The structures were written using circular polarisation. Each structure consisted of two written tracks separated by a distance which is given in the following table. The pulse energy, polarisation and writing direction were also varied, and details of the various writing conditions used are shown below.

Pulse Energy (nJ)	Scan Separation (μm)	Depth of Structure Below Surface (μm)	Writing Direction (positive or negative)
578	20	360	-
578	20	360	+
578	25	360	-
578	25	360	+
578	30	360	-

Pulse Energy (nJ)	Scan Separation (μm)	Depth of Structure Below Surface (μm)	Writing Direction (positive or negative)
578	30	360	+
578	35	360	-
578	35	360	+
551	20	360	-
551	20	360	+
551	25	360	-
551	25	360	+
551	30	360	-
551	30	360	+
551	35	360	-
551	35	360	+
524	20	360	-
524	20	360	+
524	25	360	-
524	25	360	+
524	30	360	-
524	30	360	+
524	35	360	-
524	35	360	+
499	20	360	-
499	20	360	+
499	25	360	-
499	25	360	+
499	30	360	-
499	30	360	+
499	35	360	-
499	35	360	+
476	20	360	-
476	20	360	+
476	25	360	-
476	25	360	+
476	30	360	-
476	30	360	+
476	35	360	-

Pulse Energy (nJ)	Scan Separation (μm)	Depth of Structure Below Surface (μm)	Writing Direction (positive or negative)
476	35	360	+
453	20	360	-
453	20	360	+
453	25	360	-
453	25	360	+
453	30	360	-
453	30	360	+
453	35	360	-
453	35	360	+
432	20	360	-
432	20	360	+
432	25	360	-
432	25	360	+
432	30	360	-
432	30	360	+
432	35	360	-
432	35	360	+
411	20	360	-
411	20	360	+
411	25	360	-
411	25	360	+
411	30	360	-
411	30	360	+
411	35	360	-
411	35	360	+
392	20	360	-
392	20	360	+
392	25	360	-
392	25	360	+
392	30	360	-
392	30	360	+
392	35	360	-
392	35	360	+
373	20	360	-

Pulse Energy (nJ)	Scan Separation (μm)	Depth of Structure Below Surface (μm)	Writing Direction (positive or negative)
373	20	360	+
373	25	360	-
373	25	360	+
373	30	360	-
373	30	360	+
373	35	360	-
373	35	360	+
355	20	360	-
355	20	360	+
355	25	360	-
355	25	360	+
355	30	360	-
355	30	360	+
355	35	360	-
355	35	360	+
339	20	370	-
339	20	370	+
339	25	370	-
339	25	370	+
339	30	370	-
339	30	370	+
339	35	370	-
339	35	370	+
392	20	370	-
392	20	370	+
392	25	370	-
392	25	370	+
392	30	370	-
392	30	370	+
392	35	370	-
392	35	370	+
373	20	370	-
373	20	370	+
373	25	370	-

Pulse Energy (nJ)	Scan Separation (μm)	Depth of Structure Below Surface (μm)	Writing Direction (positive or negative)
373	25	370	+
373	30	370	-
373	30	370	+
373	35	370	-
373	35	370	+
355	20	370	-
355	20	370	+
355	25	370	-
355	25	370	+
355	30	370	-
355	30	370	+
355	35	370	-
355	35	370	+
337	20	370	-
337	20	370	+
337	25	370	-
337	25	370	+
337	30	370	-
337	30	370	+
337	35	370	-
337	35	370	+
322	20	370	-
322	20	370	+
322	25	370	-
322	25	370	+
322	30	370	-
322	30	370	+
322	35	370	-
322	35	370	+
307	20	370	-
307	20	370	+
307	25	370	-
307	25	370	+
307	30	370	-

Pulse Energy (nJ)	Scan Separation (μm)	Depth of Structure Below Surface (μm)	Writing Direction (positive or negative)
307	30	370	+
307	35	370	-
307	35	370	+
291	20	370	-
291	20	370	+
291	25	370	-
291	25	370	+
291	30	370	-
291	30	370	+
291	35	370	-
291	35	370	+
278	20	370	-
278	20	370	+
278	25	370	-
278	25	370	+
278	30	370	-
278	30	370	+
278	35	370	-
278	35	370	+
264	20	370	-
264	20	370	+
264	25	370	-
264	25	370	+
264	30	370	-
264	30	370	+
264	35	370	-
264	35	370	+
253	20	370	-
253	20	370	+
253	25	370	-
253	25	370	+
253	30	370	-
253	30	370	+
253	35	370	-

Pulse Energy (nJ)	Scan Separation (μm)	Depth of Structure Below Surface (μm)	Writing Direction (positive or negative)
253	35	370	+

Table A.2. Writing conditions used to create channel waveguide in Yb:KYW.

These two tables provide a complete list of all structures investigated in the work which led to the results which are presented in Chapter 5.